arXiv:hep-ex/0510009v1 4 Oct 2005

EUROPEAN ORGANIZATION FOR NUCLEAR RESEARCH

Inclusive Production of Charged Pions in p+p Collisions at 158 GeV/c Beam Momentum

C. Alt[8], T. Anticic[17], B. Baatar[7], D. Barna[4], J. Bartke[5], L. Betev[9], H. Białkowska[15], C. Blume[8],
B. Boimska[15], M. Botje[1], J. Bracinik[3], P. Bunčić[9], V. Cerny[3], P. Christakoglou[2], O. Chvala[12],
P. Dinkelaker[8], J. Dolejsi[12], V. Eckardt[11], H.G. Fischer[9], D. Flierl[8], Z. Fodor[4], P. Foka[6],
V. Friese[6], M. Gaździcki[8,10], K. Grebieszkow[16], C. Höhne[6], K. Kadija[17], A. Karev[11,9],
M. Kliemant[8], S. Kniege[8], V.I. Kolesnikov[7], E. Kornas[5], R. Korus[10], M. Kowalski[5], I. Kraus[6],
M. Kreps[3], M. van Leeuwen[1], B. Lungwitz[8], M. Makariev[14], A.I. Malakhov[7], M. Mateev[14],
G.L. Melkumov[7], M. Mitrovski[8], S. Mrówczyński[10], G. Pálla[4], D. Panayotov[14], A. Petridis[2],
R. Renfordt[8], M. Rybczyński[10], A. Rybicki[5,9], A. Sandoval[6], N. Schmitz[11], T. Schuster[8],
P. Seyboth[11], F. Siklér[4], E. Skrzypczak[16], G. Stefanek[10], R. Stock[8], H. Ströbele[8], T. Susa[17],
J. Sziklai[4], P. Szymanski[9,15], V. Trubnikov[15], D. Varga[9], M. Vassiliou[2], G.I. Veres[4],
G. Vesztergombi[4], D. Vranić[6], S. Wenig[9,*)], A. Wetzler[8], Z. Włodarczyk[10], I.K. Yoo[13]

(The NA49 Collaboration)

[1]NIKHEF, Amsterdam, Netherlands.
[2]Department of Physics, University of Athens, Athens, Greece.
[3]Comenius University, Bratislava, Slovakia.
[4]KFKI Research Institute for Particle and Nuclear Physics, Budapest, Hungary.
[5]Institute of Nuclear Physics, Cracow, Poland.
[6]Gesellschaft für Schwerionenforschung (GSI), Darmstadt, Germany.
[7]Joint Institute for Nuclear Research, Dubna, Russia.
[8]Fachbereich Physik der Universität, Frankfurt, Germany.
[9]CERN, Geneva, Switzerland.
[10]Institute of Physics Świętokrzyska Academy, Kielce, Poland.
[11]Max-Planck-Institut für Physik, Munich, Germany.
[12]Institute of Particle and Nuclear Physics, Charles University, Prague, Czech Republic.
[13]Department of Physics, Pusan National University, Pusan, Republic of Korea.
[14]Atomic Physics Department, Sofia University St. Kliment Ohridski, Sofia, Bulgaria.
[15]Institute for Nuclear Studies, Warsaw, Poland.
[16]Institute for Experimental Physics, University of Warsaw, Warsaw, Poland.
[17]Rudjer Boskovic Institute, Zagreb, Croatia.

Abstract

New results on the production of charged pions in p+p interactions are presented. The data come from a sample of 4.8 million inelastic events obtained with the NA49 detector at the CERN SPS at 158 GeV/c beam momentum. Pions are identified by energy loss measurement in a large TPC tracking system which covers a major fraction of the production phase space. Inclusive invariant cross sections are given on a grid of nearly 300 bins per charge over intervals from 0 to 2 GeV/c in transverse momentum and from 0 to 0.85 in Feynman x. The results are compared to existing data in overlapping energy ranges.

---

*) Corresponding author: Siegfried.Wenig@cern.ch

1 Introduction

The NA49 collaboration has set out to explore an extended experimental programme concerning non-perturbative hadronic interactions at SPS energies. This programme covers elementary hadron–proton collisions as well as hadron–nucleus and nucleus–nucleus reactions. It is aimed at providing for each type of interaction large statistics data samples obtained with the same detector layout which combines wide acceptance coverage with complete particle identification. It is therefore well suited for the comparison of the different processes and to a detailed scrutiny of the evolution from elementary to nuclear hadronic phenomena. In the absence of reliable theoretical predictions in the non-perturbative sector of QCD, it is one of the main aims of this study to provide the basis for a model independent approach to the underlying production mechanisms. This approach has to rely on high quality data sets which cover both the full phase space and a variety of projectile and target combinations.

The present paper addresses the inclusive production of charged pions in p+p collisions. In the multiparticle final states encountered at SPS energies, single particle inclusive measurements cover only the simplest hypersurface of a complex multidimensional phase space. Only moderate hopes may be nursed to learn enough from such measurements alone to experimentally constrain the non-calculable sector of QCD, and additional studies beyond the inclusive surface constitute indeed an important part of the NA49 programme.

However, as will be shown below, the experimental situation even in the most simple case of inclusive cross sections is far from being satisfactory. Notwithstanding a sizeable number of preceding efforts especially in the SPS energy range which in part date back several decades, it has not been possible to obtain sufficiently precise and internally consistent data sets covering the whole available phase space. Precision in this context may be defined as the possibility to establish from the existing data an ensemble of cross sections which will be consistent within well defined error limits. From the physics point of view, this ensemble should permit the study of the evolution of inclusive yields from elementary to nuclear interactions. This evolution is characterized for pions by deviations of typically some tens of percent in comparison to the most straightforward superposition of elementary hadronic interactions. Its interpretation and especially any claim of connection with new physics phenomena has to rely completely on comparison with elementary data. Due to the poverty of available data sets in this sector, situations have arisen where data from nucleus–nucleus collisions are more complete and precise than the elementary reference.

It seems therefore mandatory and timely to attempt a new effort in this field with the aim of providing an improved elementary data base.

This paper is arranged as follows. In Section 2, the experimental situation in the SPS energy range is described. Sections 3 to 6 present the data samples obtained by NA49 and a detailed discussion of event cuts, particle identification, cross section normalization and applied corrections. The final data are presented and tabulated in Sections 7 and 9. A detailed comparison to existing data including a complete statistical analysis is given in Sections 8 and 9. A short discussion of the results in relation to forthcoming supplementary publications terminates the paper in Section 10.

2 The Experimental Situation

A band of beam momenta extending from 100 to about 400 GeV/c corresponding to an interval in $\sqrt{s}$ from 14 to 27 GeV may be defined as SPS/Fermilab energy range. In this interval, quite a number of experiments have published inclusive particle yields [1–12]. They may be tentatively divided into three different categories.

The first class concerns bubble chamber applications, here mostly restricted to relatively small data samples of order 10 000 events each obtained with the Fermilab 30 inch bubble chamber. It is characterized by the absence of particle identification as far as pions are concerned.

The second class covers spectrometer measurements with small solid angle devices measuring typically well delineated and restricted ranges in production angle and featuring complete particle identification.

A third class contains large solid angle spectrometers like the EHS and OMEGA facilities at CERN, with the restriction that very few, if any results concerning inclusive data have been published from these experiments.

In the framework of the present publication the data without particle identification and therefore with heavy assumptions about kaon and baryon yields for pion extraction have been discarded from comparison.

We are interested in the available measurements of the double differential cross section of identified pions

$$\frac{d^2\sigma}{dx_F dp_T^2} \tag{1}$$

as a function of the phase space variables defined in this paper as transverse momentum p_T and reduced longitudinal momentum

$$x_F = \frac{p_L}{\sqrt{s}/2} \quad , \tag{2}$$

where p_L denotes the longitudinal momentum component in the cms.

A search for such data with pion identification practically eliminates the first and third class. The phase space coverage of the remaining spectrometer experiments is characterized in Fig. 1a for the fixed target configurations. The very limited range of these experiments is immediately apparent from this plot. Data are scarce or lacking completely in the regions of p_T below 0.3 GeV/c and above 1 GeV/c as well as x_F below 0.2. In addition it will be shown in Section 8.2 below that the most copious data set of Johnson et al. [6] is afflicted with large systematic deviations which makes it unusable for quantitative reference.

It has therefore been decided to also include some of the rather extensive data from ISR

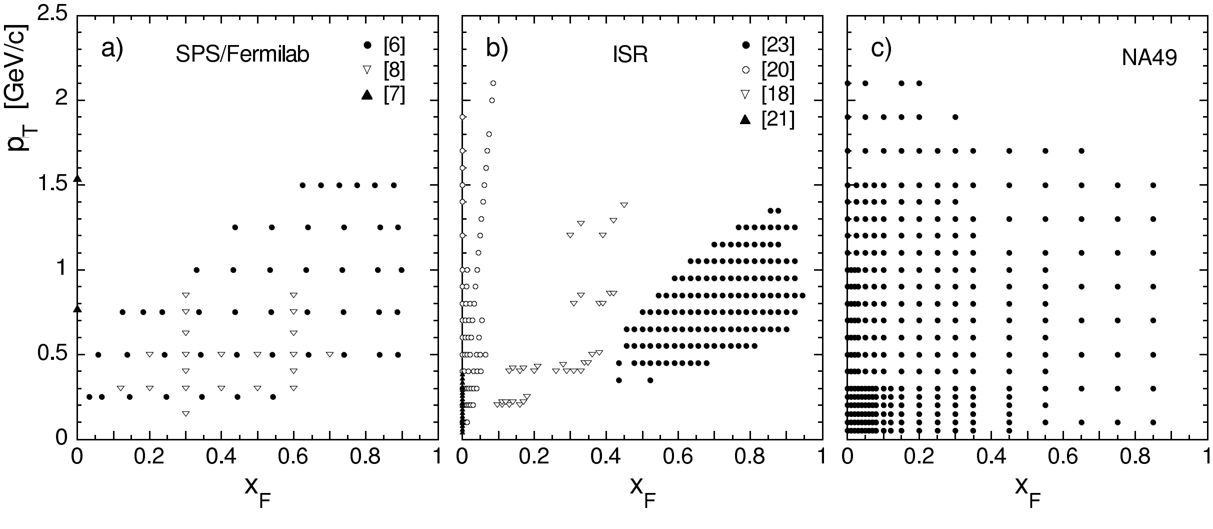

Figure 1: Phase space coverage of existing data in the a) SPS/Fermilab and b) ISR energy range compared to c) NA49. Each set of symbols represents a set of measurements.

experiments [13–23] into the comparison in the $\sqrt{s}$ range from 23 to 63 GeV as indicated in Fig. 1b. As a detailed study of s-dependence over the complete kinematic plane is outside the scope of the present paper, only data at $x_F > 0.3$ have been used for the comparison. In this region Feynman scaling is expected to hold on a few percent level whereas a more involved s-dependence is present at low x_F.

The phase space coverage of the NA49 apparatus is shown for comparison in Fig. 1c. This acceptance allows for the first time a detailed study of the low p_T region and is only limited by statistics at p_T above 2 GeV/c. In addition, there is a restricted loss of acceptance at $x_F > 0.7$ in the lower p_T range for π^+ due to the interaction trigger used (see Section 3.3).

The main aim of the present paper is to contribute new data covering the accessible phase space as densely and continuously as possible in a single experiment. This aim needs first of all a very high statistics event sample. In addition, high quality particle identification has to be performed over the accessible range of kinematic variables. As a third basic requirement the absolute normalization and the systematic error sources should be controlled on an adequate level with respect to the statistical uncertainties.

3 The NA49 Experiment

NA49 is a fixed target experiment situated in the H2 beam line at the CERN SPS accelerator complex. It uses a set of large Time Projection Chambers (TPC) together with two large aperture Vertex Magnets (VTX1,2) for tracking and particle identification. A schematic view of the detector is shown in Fig. 2 with an overlay of tracks from a typical mean multiplicity p+p event. The details of the detector layout, construction and performance are described in [24].

In order to introduce and explain the data taking and analysis policies adopted in the present work on elementary hadronic cross sections, some general features of the detector system have to be stressed:

- The data flow from the $1.8 \cdot 10^5$ TPC electronics channels whose analog outputs are digitized in 512 time buckets per channel produces event sizes of about 1.5 Mbyte after zero suppression. This in turn limits the total number of events that can be recorded, stored and processed. The data sample analyzed in this paper corresponds to a raw data volume of 10 Tbytes.
- The readout system which has been optimized for operation with heavy ion collisions only allows a recording rate of 32 events per accelerator cycle.
- This readout rate can be saturated with rather modest beam intensities of about 10^4/s which keeps the rate of multiple events during the 50 μs open time of the TPC tracker small enough to be readily eliminated off-line.
- Due to the limitations discussed above, the unbiased running on a beam trigger alone with alternating full and empty target is not feasible. The experiment has therefore to be operated with an interaction trigger which unavoidably introduces a certain trigger bias. The corrections for this bias are discussed in detail in Section 5.2 below.

3.1 The Beam

The secondary hadron beam was produced by 400 GeV/c primary protons impinging on a 10 cm long Be target. Secondary hadrons were selected in a beam line set at 158 GeV/c momentum with a resolution of 0.13%. The particle composition of the beam was roughly 65% protons, 30% pions and 5% kaons. Protons were identified using a CEDAR [25] Ring Cerenkov counter (see insert Fig. 2) with a misidentification probability of less than 10^{-3}. Typical beam

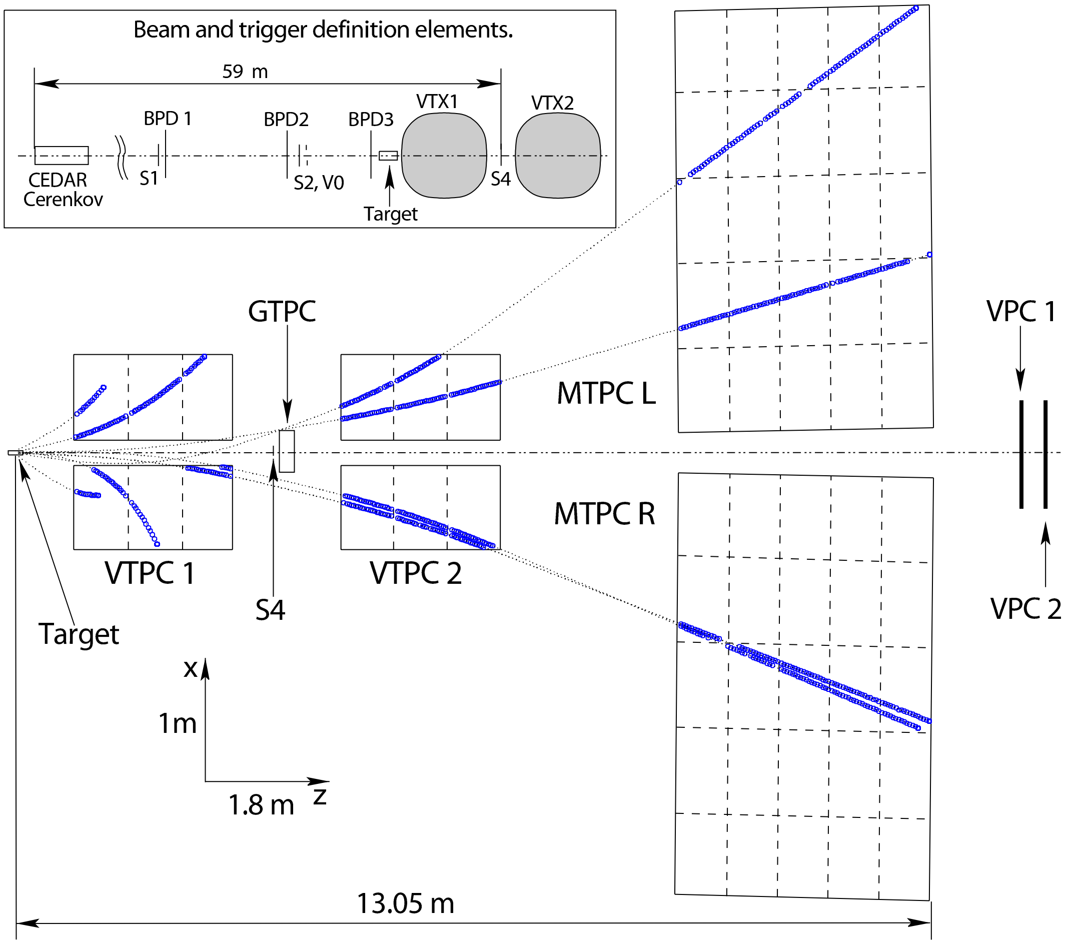

Figure 2: NA49 detector layout and tracks of a typical mean multiplicity p+p event. The open circles are the points registered in the TPC's, the dotted lines are the interpolation trajectories between the track segments and the extrapolations to the event vertex in the LH_2 target. The beam and trigger definition counters are presented in the inset. Detector name abbreviations are explained in the text.

intensities on target were $3 \cdot 10^4$ particles per extraction of 2.37 s. Two scintillators (S1 and S2 in Fig. 2) provided beam definition and timing, together with a ring-shaped veto counter (V0) reducing the background from upstream interactions. Three two-plane proportional chambers (BPD1–3 in Fig. 2) with cathode strip readout measured the projectile trajectory yielding 150 μm position and 4.5 μrad angle resolution at the target position where the beam profile had a full width at base of 6 mm horizontally and 4 mm vertically.

3.2 The Target

A liquid hydrogen target of 20.29 cm length (2.8% interaction length) and 3 cm diameter placed 88.4 cm upstream of the first TPC (VTPC-1) was used. The exact target length is determined from the distribution of the reconstructed vertex positions in high multiplicity empty target events as shown in Fig. 3.

Runs with full and empty target were alternated. As the empty/full event ratio can be reduced from initially 18% to 9% after suitable offline cuts, and as the empty target rate has been shown to be treatable as a small correction to the full target data, see Section 5.1, the empty target running could be kept to a fraction of a few percent of the total data taking.

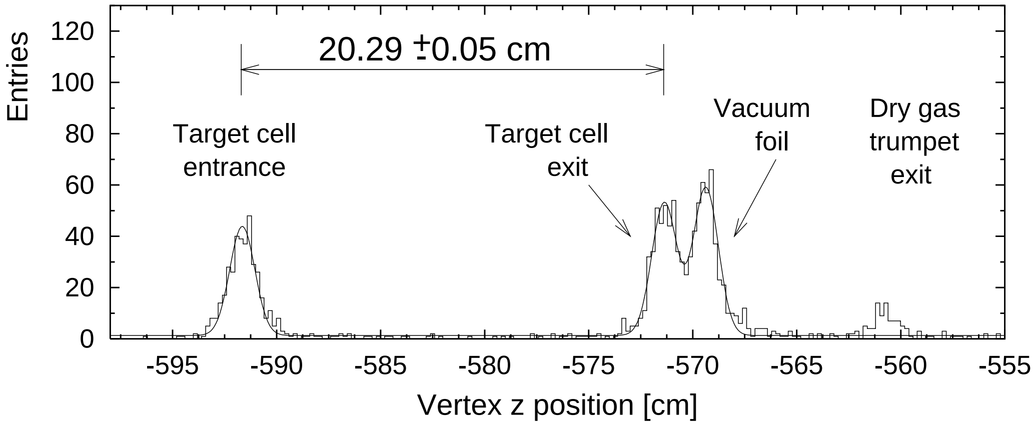

Figure 3: Distribution of reconstructed vertex position in high multiplicity empty target events delivering the exact target length.

The target was filled with para-Hydrogen obtained in a closed-loop liquefaction system which was operated at 75 mbar overpressure with respect to atmosphere. This results, at the mean atmospheric pressure of 965 mbar measured over the running periods of the experiment, in a density of $\rho_H = 0.0707$ g/cm^3. In addition, the cross section determination has to take into account the density of gaseous hydrogen ρ_{ET} present in the empty target runs. This density is obtained from the empty over full target ratio of high multiplicity events observed in a small fiducial volume around the target center. The density ratio ρ_{ET}/ρ_H turns out to be 0.5% which indicates an increase of the average temperature in the empty target by about $40°$K above liquid temperature. The boiling rate in full-target condition has been verified to present a negligible modification of the liquid density.

3.3 The Trigger

Beam protons were selected by the coincidence C·S1·S2·$\overline{\text{V0}}$ yielding the beam rate R_{beam}. The interaction trigger was defined by a small scintillation counter (S4 in Fig. 2) in anti-coincidence with the beam. This counter of 2 cm diameter was placed on the beam trajectory 380 cm downstream of the target, between the two Vertex Magnets. The trigger condition C·S1·S2·$\overline{\text{V0}}$ · $\overline{\text{S4}}$ delivered the interaction rates R_{FT} and R_{ET} for full and empty target operation, respectively. The corresponding trigger cross section σ_{trig} is calculated according to the formula

$$\sigma_{trig} = \frac{P^H}{\rho_H \cdot l \cdot N_A/A} \quad , \tag{3}$$

where l, N_A, A and ρ_H denote, respectively, the target length, the Avogadro constant, the atomic number and the liquid hydrogen target density. The interaction probability in hydrogen P^H has to be extracted from the measured rates R_{FT}, R_{ET} and R_{beam}. Taking into account the exponential beam attenuation in the target, the reduction of beam intensity due to interactions upstream of the target, the reduction of the downstream interaction probability in full target operation, and the gaseous hydrogen content of the empty target cell as discussed above, it is determined by the relation

$$P^H = \frac{R_{FT} - R_{ET}}{R_{beam}} \cdot \left(1 + \frac{R_{FT} - R_{ET}}{2 \cdot R_{beam}} + \frac{R_{ET}}{R_{beam}} + \frac{\rho_{ET}}{\rho_H}\right) \quad . \tag{4}$$

In this expression higher order terms are neglected. The resulting trigger cross section, averaged over three running periods in the years 1999, 2000 and 2002, amounts to 28.23 mb. From this value the total inelastic cross section as measured by NA49 is derived using a detailed Monte Carlo calculation which takes into account the measured inclusive distributions of protons, kaons and pions as well as the contribution from elastic scattering in order to determine the loss of events due to produced particles hitting S4. The different components resulting from this calculation are presented in Table 1.

σ_{trig}	28.23 mb
loss from p	3.98 mb
loss from π, K	0.33 mb
contribution from σ_{el}	-1.08 mb
predicted σ_{inel}	31.46 mb
literature value	31.78 mb

Table 1: Contributions derived by a detailed Monte Carlo calculation to the determination of the inelastic cross section σ_{inel}.

It appears that the extracted inelastic cross section compares with the literature value of 31.78 mb [26] to within one percent. The total trigger loss concerning inelastic events amounts to 14.4%. The rejected events come mostly from target diffraction (about 2.5 mb) and from non- diffractive events containing forward charged particles at high x_F which hit S4. In order to account for this event rejection, a topology-dependent correction to the inclusive cross sections is applied, as described in Section 5.2.

3.4 Tracking and Event Reconstruction

The tracking system of the NA49 detector comprises a set of large volume Time Projection Chambers covering a total volume of about 50 m^3. Two of them (VTPC-1 and VTPC-2 in Fig. 2) are placed inside superconducting Vertex Magnets with a combined bending power of 9 Tm. The magnets define by their aperture the phase space available for tracking. Two larger TPC's (MTPC-R and MTPC-L in Fig. 2) are positioned downstream of the magnets in order to extend the acceptance to larger momenta and to provide sufficient track length for precise particle identification via ionization energy loss dE/dx measurement. The use of the same detector for the complete range of interactions implies a separation of the sensitive TPC volumes with respect to the beam trajectory. Otherwise, in the case of heavy ion collisions non-interacting beam particles would create excessive chamber loads and the density of secondary tracks would be prohibitively high. The corresponding acceptance loss for low p_T particles in the x_F range above 0.5 has been remedied by the introduction of a small TPC on the beam line in between the two magnets (GTPC in Fig. 2) which, in combination with two strip-readout proportional chambers (VPC-1 and VPC-2 in Fig. 2) ensures tracking acceptance up to the kinematic limit. As the target is placed upstream of the magnets there is a gradual reduction of acceptance at low p_T in the backward hemisphere which for pions starts to be effective for $x_F < -0.05$. The overall acceptance region for tracking of pions in the forward x_F/p_T plane has been shown in Fig. 1c.

The event reconstruction proceeds through several steps. Firstly, all charged track candidates leaving at least 8 space points (clusters) in the TPC system are pattern recognized and momentum fitted. This step includes the formation of global tracks from track segments visible in different TPC's (see Fig. 2). Secondly, a primary event vertex is fitted using all global tracks found in the event together with the measured beam track. After a successful vertex reconstruction, a second path of momentum fitting is performed also including tracks which are only recorded in the downstream TPC's outside the magnetic field. In this final momentum fit, the determined vertex point is used as an additional measured point on the track. All tracks with an acceptable χ^2 of the fit are retained for further analysis.

3.5 Event Selection

Two steps of event selection are introduced in order to clean up the event sample and to reduce the empty target background.

Firstly, cuts on the beam position close to the target are performed. The position of the incoming beam particle is registered in three Beam Position Detectors (BPD1-3 in Fig. 2). The three corresponding measurements are required to be well defined and collinear in both measured transverse coordinates by imposing that the extrapolation from BPD-1 and BPD-2 to BPD-3 coincides with the beam position measured in BPD-3, as demonstrated in Fig. 4. A further, less restrictive cut is imposed on the beam profile. These cuts are bias-free as the measurement takes place before the interaction.

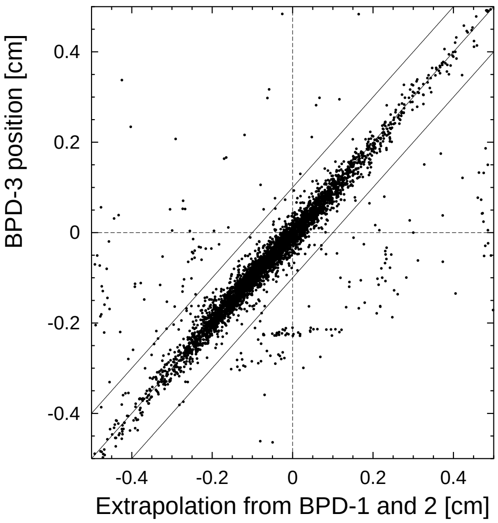

Figure 4: Beam position at BPD-3 versus extrapolation of beams from BPD-1 and BPD-2 to BPD-3. Only events falling between the two lines are accepted.

Secondly, the interaction vertex is constrained to a fiducial region around the target position by applying a cut on the longitudinal coordinate of the reconstructed vertex position. Though this cut is very efficient in reducing the empty target contribution, it must be carefully designed as the precision of the reconstructed vertex position depends strongly on the event configuration. The longitudinal vertex cut is therefore performed depending on the track multiplicity and on the track topology. Short or very small laboratory angle tracks are not entering the track sample determining the vertex and the cut boundaries are placed so that no event from the target is rejected. This is exemplified in the normalized vertex distributions from full and empty target shown in Fig. 5a and b. For the 5% of the target events with at least one reconstructed track, for which the reconstruction software does not give a reliable longitudinal vertex position, the target center is used.

The combined event selection described above reduces the relative empty target yield from 18% to 9% retaining 85% of the liquid hydrogen target events. This final sample corre-

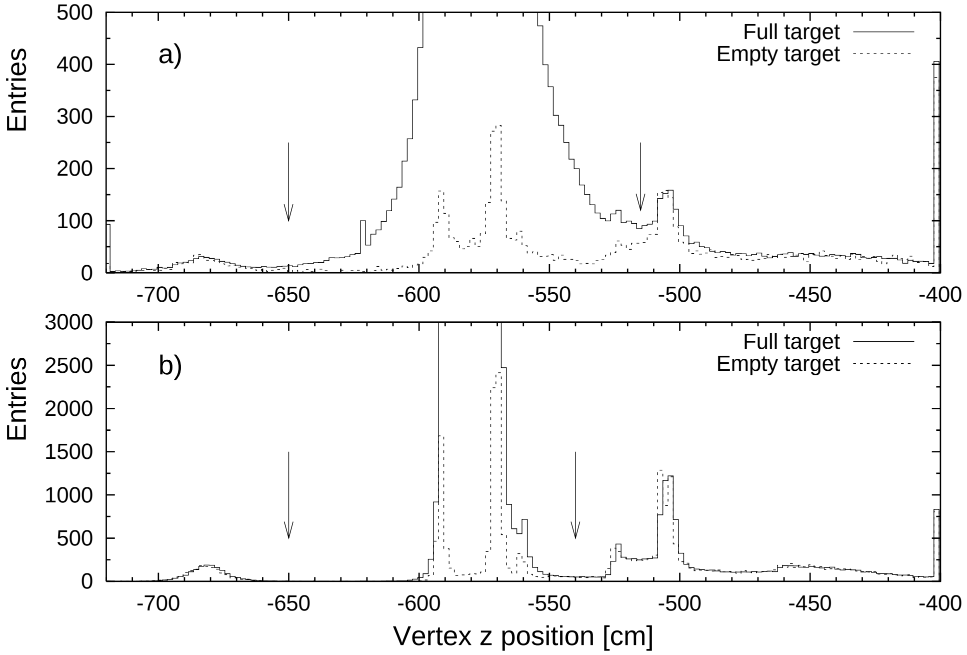

Figure 5: Normalized vertex distributions from full and empty target events with selected track multiplicity a) one and b) five and more. The imposed vertex cuts are indicated by arrows.

sponds to $4.8 \cdot 10^6$ events which were obtained in three running periods between the years 1999 and 2002, as shown in Table 2.

3.6 Track Selection

A track in the NA49 detector is defined by the ensemble of clusters (points) in three dimensions that a charged particle leaves in the effective volume of the TPC system. These clusters have a typical spacing in track direction of about 3 cm in the VTPC's and 4 cm in the MTPC regions. The tracking in a TPC environment has several decisive advantages which make the track selection a relatively straight-forward and safe task:

- The local efficiency for cluster formation is practically 100% with a loss rate below the permille level. This is guaranteed by the choice of operation point of the readout proportional chambers and by the high reliability of the readout electronics which has a fraction of less than 10^{-3} of missing or malfunctioning channels.
- The total number of points expected on each track can be reliably predicted by detector simulation with the exception of some edge regions for the VTPC's due to magnetic field $E \times B$ effects.

	Events taken		Events after cuts	
Year	Full target	Empty target	Full target	Empty target
1999	1 211 k	41.2 k	906 k	13.7 k
2000	2 648 k	47.8 k	2 049 k	16.9 k
2002	2 508 k	69.0 k	1 814 k	21.8 k
Total	6 367 k	158.0 k	4 769 k	52.4 k

Table 2: Data samples analyzed.

- Regions of 100% acceptance can be readily defined in each kinematic bin Δx_F, Δp_T, and the azimuthal angle wedge $\Delta\Phi$ by inspecting the distribution of points per track in comparison to the expected value. In practice this is achieved by adjusting $\Delta\Phi$ such that this distribution does not show tails beyond a well-defined average. This gives at the same time an experimental handle to stay away from edge regions which show a drop of the number of points.
- The only possibility of track losses or a reduction of track length is due to weak decays or hadronic interaction in the detector gas. The policy adopted in the present analysis is to allow a track to be shorter than expected if it has a minimum length and if the lost points are concentrated at the end of the track. It has been verified by eye-scans on such shortened tracks that either a decay (presence of one additional downstream track at an angle to the primary track) or a hadronic interaction (several additional tracks emerging from a defined interaction vertex) is present.

In practice each track entering the analysis sample has to have at least 30 points in order to ensure a minimum quality of particle identification (see Section 4). This corresponds to detected track lengths in excess of 90 cm. The only exception to this criterion is in the extreme forward direction where the GTPC/VPC combination has only 9 space points and where no particle identification via dE/dx is feasible. An example of a point number distribution in a typical analysis bin is given in Fig. 6.

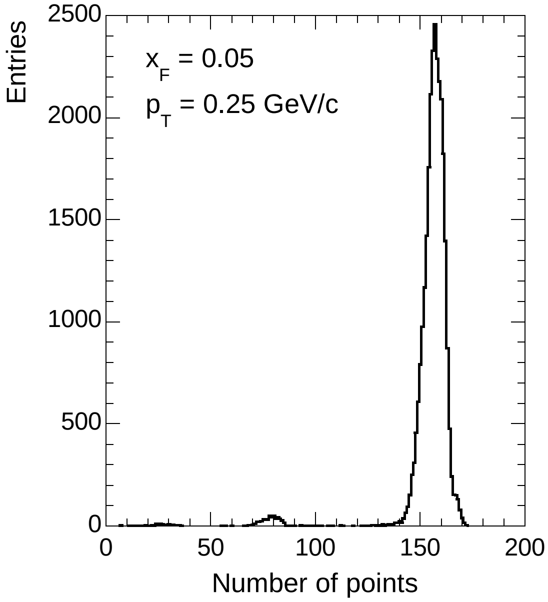

Figure 6: Distribution of the number of measured points in a typical analysis bin at $x_F = 0.05$ and $p_T = 0.25$ GeV/c.

The corresponding tracks span 3 TPC's (VTPC-1,VTPC-2,MTPC) with an expected number of about 160 clusters. 2.15% of all tracks are found in two distinct accumulations around 80 and 30 points, corresponding to tracks detected up to the end of VTPC-2 (1.7%) and VTPC-1 (0.45%), respectively. This has to be compared to the expected fraction from nuclear interactions, 1.2% and 0.3%, confirming that the reconstruction software does not introduce short tracks, and therefore potential background, of unexplained sources. The small fraction of tracks falling below the 30 point cut is corrected for by the absorption correction described in Section 5.4.

The track selection criteria defined above have been controlled by extensive eye-scans. This method is made very efficient in the low multiplicity environment of p+p collisions by the photograph-like picture built up by the measured space points and by the excellent pattern recognition capability of the human eye. Based on extensive studies with special care for potentially problematic areas (high p_T, edge regions of acceptance, short tracks) the tracking efficiency is found to be 100% with an upper error limit of 0.5% below $x_F = 0.3$ rising to less than 2% close to the kinematic boundary approached by the GTPC/VPC combinations.

3.7 Acceptance Coverage, Binning and Statistical Errors

The event sample defined above contains a total of about 28 million pions. In order to cover the available acceptance in an optimum fashion, a binning scheme presented in Fig. 7 has been chosen in the variables x_F and p_T. There are several aspects determining this choice:

- Optimum exploitation of the available statistics
- Definition of bin centers at user-friendly and consistent values of x_F and p_T
- Compliance with the structure of the inclusive cross sections
- Sufficiently small bins in p_{tot} for optimum extraction of ionization energy loss for particle identification
- Avoidance of overlaps and minimization of lost regions
- Optimization of bin sizes for minimum binning effects and corresponding corrections

The resulting statistical precision per bin is also indicated in Fig. 7. This precision is superior or equal to all other existing measurements in the SPS/Fermilab and ISR energy regions with the exception of a few points at large p_T and/or large x_F.

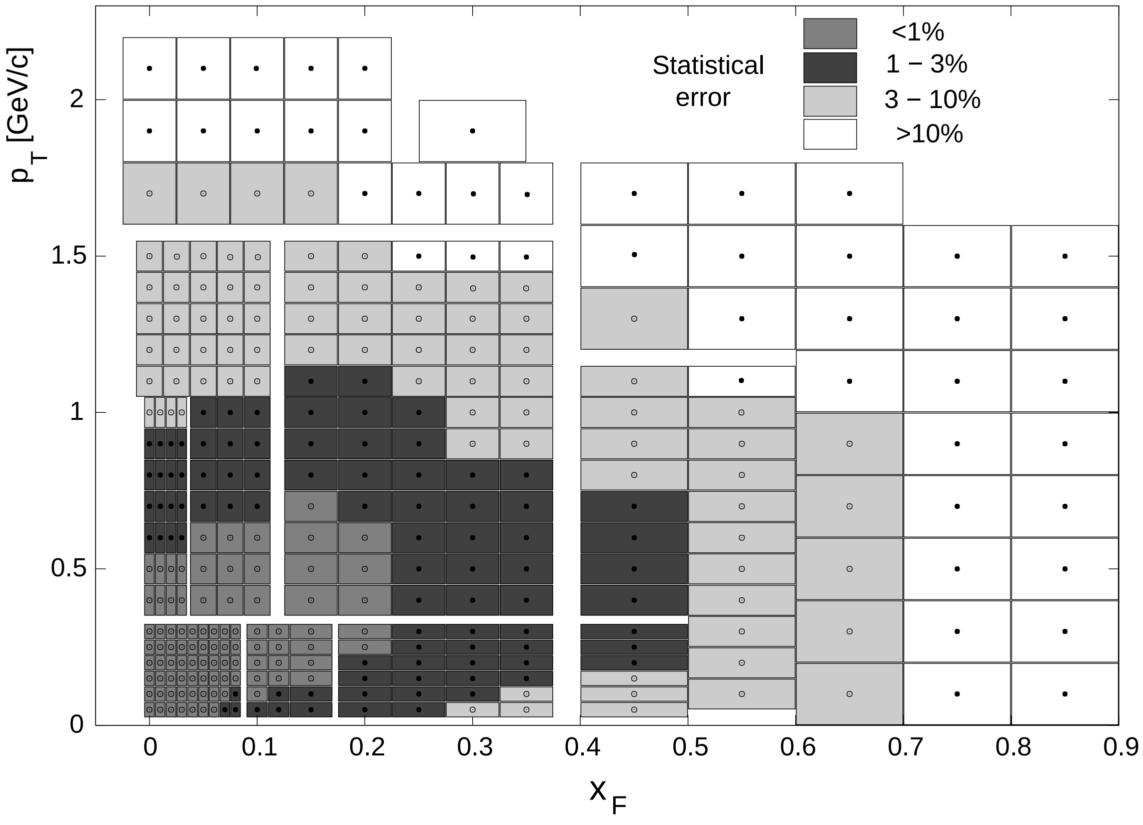

Figure 7: Binning scheme in x_F and p_T together with information about the statistical error.

4 Particle Identification

4.1 Identification Method, Parametrizations and Performance

The NA49 detector offers a powerful combination of tracking and particle identification via ionization energy loss (dE/dx) measurement in the TPC system. This system combines four large TPC volumes and features track lengths of between 1 m and 6 m in the kinematic region for pions covered in this publication. Each track is sampled by readout pads of 2.8 and 4 cm length in the Vertex and Main TPC's, respectively. This results in the pattern of sample numbers N_s per track as a function of x_F and p_T shown in Fig. 8 .

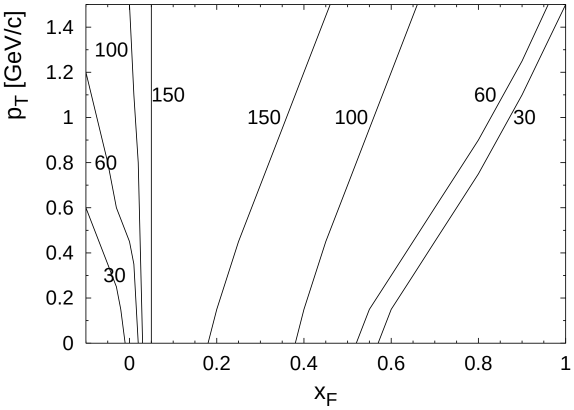

Figure 8: Lines for constant number of dE/dx samples per track in the x_F/p_T plane (restricted $\Delta\Phi$ range of selected tracks).

The dE/dx measurement is achieved by forming a truncated mean of the 50% smallest charge deposits sampled along each track. The truncation transforms the Landau distribution of the samples into a Gaussian distribution of the mean per track if the number of samples stays above about 30. Under this condition the relative resolution of the energy loss measurement can be parametrized as

$$\frac{\sigma(N_s, dE/dx)}{dE/dx} = \sigma_0 \frac{1}{N_s^{\beta}} (dE/dx)^{\alpha} \tag{5}$$

where the dependence of the truncated mean on the number of samples $dE/dx(N_s)$ and the parameters σ_0, α and β are determined experimentally. To this end, for each of the 62 readout sectors of the TPC system, tracks are binned in laboratory momentum p_{lab} and a preliminary truncated mean distribution is formed with the samples found outside the sector under study. Sharp cuts are performed on this preliminary dE/dx measurement in order to separate electrons, pions, kaons and protons in each momentum bin. Samples from different, identified tracks in the given sector are then combined into truncated means with an arbitrary number of samples in order to determine the dependences defined above.

The dependence of the dE/dx measurement on the number of samples, $dE/dx(N_s)$ is shown in Fig. 9a. The dependences of the resolution on dE/dx and N_s are presented in Fig. 9b and 9c. The parameters α and β are fitted to

$$\alpha = -0.39 \pm 0.03 \qquad \text{and} \qquad \beta = 0.50 \pm 0.01 \quad .$$

The NA49 TPC system employs different gases based on Ne in the VTPC and Ar in the MTPC. The function $dE/dx(N_s)$ and the parameters α and β are found to be independent of the type of gas. Also the parameter σ_0 referred to the same pad length is the same for Ne

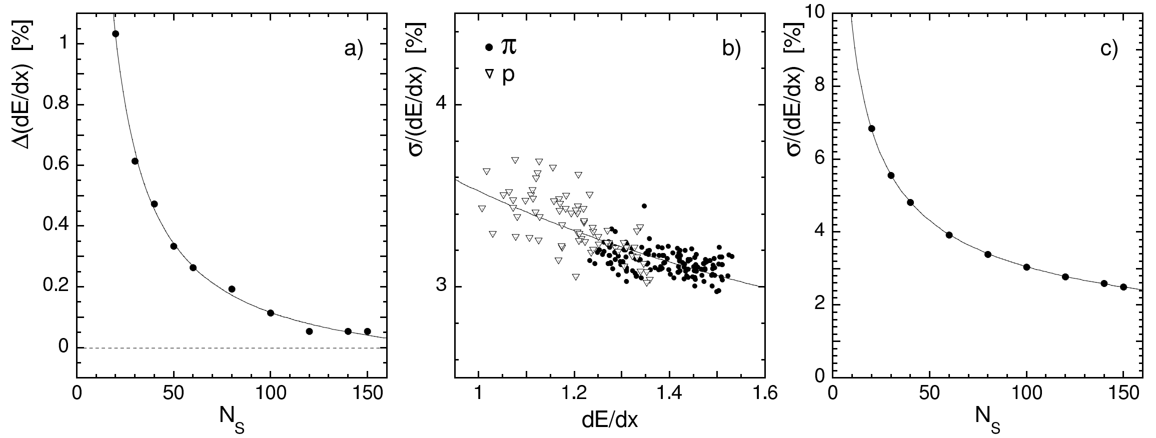

Figure 9: a) Percentage deviation of the mean $dE/dx(N_s)$ from $dE/dx(\infty)$ as a function of N_s; resolution as a function of b) dE/dx and c) N_s. All 3 panels are for MTPC.

and Ar. This has been shown by Lehraus et al. in 1982 [27] and can be understood by the different behaviour of secondary ionization for different noble gases [28]. The only difference of resolution observed in the Vertex chambers is due to the shorter pad length with a dependence which is again given by the parameter α. The resulting values are

$$\sigma_0^{\text{Vertex}} = 0.41 \qquad \text{and} \qquad \sigma_0^{\text{Main}} = 0.352 \quad .$$

The measured truncated means have a nonlinear relationship to the Bethe Bloch function which describes the primary ionization loss and has a different dependence on particle velocity ($\beta\gamma$) in the two gases. This difference which is of the order of 0-5% for different regions of $\beta\gamma$ has to be taken into account. Using the above methodology the energy loss functions are independently determined for the two gases. In order to combine samples from the VTPC and MTPC on the same track two independent truncated means are formed. The value from the MTPC is transformed to the corresponding value of the VTPC using a linear transformation. The weighted average of these numbers, taking the respective resolutions into account, results in the final dE/dx measurement.

It has to be mentioned that before the formation of truncated means a number of corrections have to be applied to each ionization sample. This concerns detailed time dependence extending over the complete data taking period of several years including pressure dependence up to second order terms, and corrections for track angles, effects of magnetic field and drift length dependences principally induced by the electronics threshold cut combined with electron diffusion in the gas.

The resulting relative resolution is typically on the 3-4% level over most of the phase space covered by this experiment with tails up to 8% at low x_F and p_T and at large x_F due to the decrease of sample numbers. The scatter plot of dE/dx values (referred to minimum ionization) versus track momentum shown in Fig. 10 gives an impression of the performance with respect to the necessity to separate particles in the region of the relativistic rise. The lines shown in Fig. 10 represent the mean response of the detector to the different types of particle derived from the measured energy loss.

4.2 Fit Procedure and Yield Determination

The particle identification, i.e. the determination of the yields of individual particle species is achieved by a fit to the dE/dx distribution for a small region of momentum defined

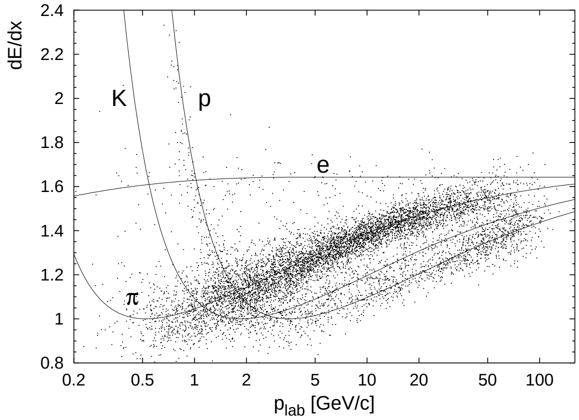

Figure 10: Energy loss dE/dx with respect to minimum ionization as a function of track momentum p_{lab}.

by the analysis bin. This distribution is a superposition of Gaussians with variances following for each particle type the parametrization specified in Formula 5 above, and thus taking proper account of the variation of N_s over the bin. Two typical examples are shown in Fig. 11.

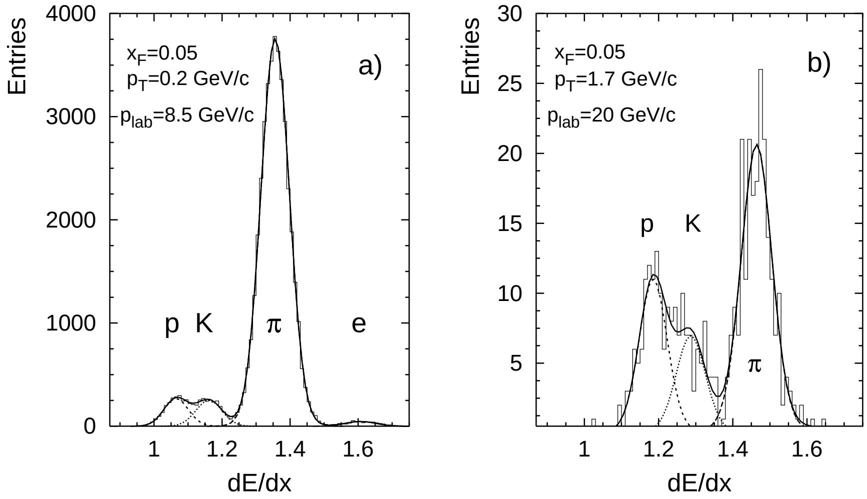

Figure 11: dE/dx distribution for two different x_F/p_T bins. The line represents the fit.

The fit has in principle nine parameters: four particle yields, four mean dE/dx values and the σ_0 parameter describing the width of the individual distributions. The last five parameters would be determined exactly by the energy loss function and the resolution function (Formula 5) if these quantities could be absolutely predicted. Due to the complexity of the primary and secondary ionization processes this prediction is, however, not possible on the level of precision needed here. The mean energy loss which is a unique function of $p_{lab}/m = \beta\gamma$ (see Fig. 10) has therefore to be described by a multi-parameter approximation which must be expected to show deviations from the measured response. Detector related imperfections in the elaboration of local calibration, magnetic field effects and pulse formation introduce additional deviations which in general violate the $\beta\gamma$ scaling of the elementary process. The resulting pattern of displacements has a smooth dependence on the kinematic variables as exemplified in Fig. 12, where the deviations are shown as a function of p_T at a fixed x_F for pions.

Indeed, in order to keep the systematic error of the yield extraction well below the sta-

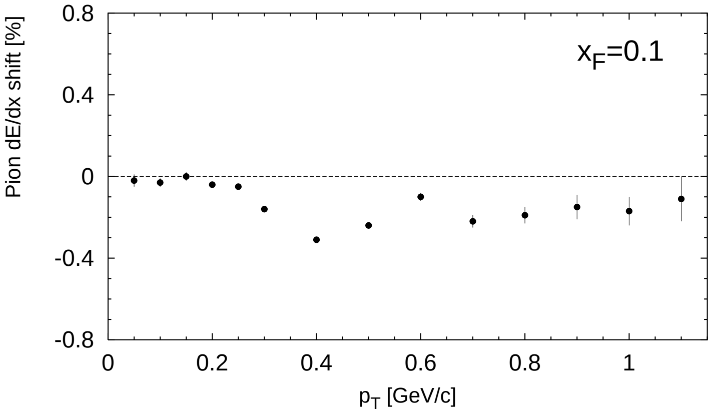

Figure 12: Deviation of the measured mean dE/dx from the predicted one as a function of p_T for pions.

tistical error in a bin, these shifts have to be and can be determined on a sub-percent level by performing complete nine parameter fits. The fit procedure minimizes the χ^2 over the complete dE/dx distribution in each bin. For the χ^2 definition different prescriptions representing the degree to which the fit is considered reliable have been tested. Comparison of the results from these different prescriptions reveals consistency within the expected statistical errors, confirming that there are no visible tails or shape distortions affecting the yield extraction. The statistical error of the fit is calculated from the covariance matrix of the nine parameters using the standard χ^2 definition. For the determination of the pion yield which is dominating over most of the measured phase space, the error turns out to be equal to the square-root of the number of pions in each bin with the exception of the far forward region ($x_F > 0.3$) discussed in Section 4.5 below. This means that the fitting method itself does not introduce any further systematic uncertainty to be added to the purely statistical fluctuations of the number of pions in each bin.

As each of the 589 x_F/p_T bins is fitted individually without imposing external constraints, extensive checks of the fit outputs are performed. In fact, the results have been extracted by three people with two different programs and the consistency has been confirmed in about 300 mutual cross-check bins.

4.3 The Region of dE/dx Crossing

Below p_{lab} of about 3 GeV/c the energy loss functions of pions, kaons and protons approach each other in the so-called cross-over region, see Fig. 10. This, together with a significant reduction of track length in the same region, see Fig. 8, prohibits independent pion identification. On the other hand, as pions at $x_F = p_T = 0$ have a p_{lab} of 1.3 GeV/c, this region contains most of the inclusive pion yield and is therefore essential to complete the data set.

In order to make the measurement possible, a reflection technique already used in bubble chamber experiments [29] without any means of particle identification in this region is employed. At the laboratory momentum which corresponds to $x_F = p_T = 0$ for pions, protons are at $x_F^{\mathrm{p}} \simeq -0.3$. The proton yield can therefore be extracted from forward/backward symmetry by fitting protons in the symmetric bin at $x_F^{\mathrm{p}} \simeq +0.3$. The corresponding reflection can be applied for kaons.

In practice, the complete pion analysis bin is reflected with proton (or kaon) assumption. The dE/dx distributions for the original pion bin and the corresponding proton-reflected bin is shown in Fig. 13.

The reflection technique is used for $p_T < 0.3$ GeV/c at $x_F = 0$ and up to $x_F = 0.02$

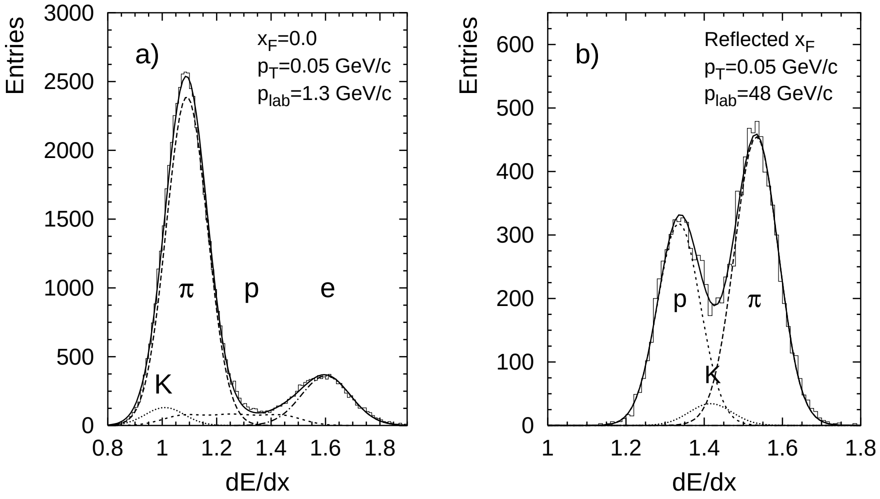

Figure 13: dE/dx distribution in a) the pion bin ($p = 1.3$ GeV/c) and b) the corresponding proton reflected bin ($p = 48$ GeV/c).

at $p_T = 0.05$ GeV/c. The estimated systematic error from this method is below 1% since the proton and kaon contributions are on the 5-10% level in this kinematic area. The consistency of the method has been tested in bins where both the normal extraction and the reflection method are usable, and its reliability was confirmed.

4.4 Electrons at High Momenta

Above p_{lab} of about 40 GeV/c the energy loss of pions approaches the relativistic plateau occupied by the electrons, rendering independent extraction difficult. This difficulty is enhanced by the fact that the e/π ratio becomes very small, typically of the order of a few permille. In order to be able to control this small contribution, a Monte Carlo simulation has been constructed using π^0 as the main source of electrons by gamma conversion and Dalitz decay. The π^0 cross section is obtained as the average of the measured charged pions and the combined conversion probability is adjusted from the measurement of the e/π ratio at $x_F = 0.05$ as shown in Fig. 14. In the high x_F region, the ratio is then constrained to the value predicted by the simulation and the small excess over the prediction obtained from the fit added to the pion yield.

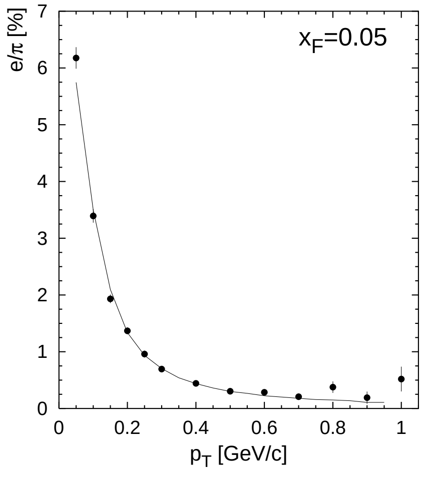

Figure 14: e/π ratio as a function of p_T at $x_F = 0.05$. The line represents the Monte Carlo result.

4.5 Constraints from K/π and p/π Ratios at High x_F

The region of x_F above about 0.3 presents specific problems for the independent extraction of kaons necessary to obtain bias-free pion cross sections. This is due to the fact that the mean ionizations of the different particle types approach each other towards saturation, and that the average track length steadily decreases. Furthermore, the cross sections fall steeply with x_F, which progressively reduces the available statistics per bin.

The combined (K$^-$+p̄)/π^- ratio is rapidly falling with x_F for all p_T values. This p_T averaged ratio as obtained from the NA49 data is shown in Fig. 15a as a function of x_F. As the dE/dx fits become rather unreliable for values of this ratio below a few percent and at low statistics, the measurement is complemented by values from other experiments [6, 8] also shown in Fig. 15a and extrapolated smoothly to zero at $x_F \simeq 0.85$.

For K$^+$ extraction, the situation becomes difficult already above $x_F \simeq 0.3$ due to the preponderant p component. This leads to problems with the independent determination of the kaon shift with respect to the energy loss function as described in Section 4.2 above. In fact the fit tends to find unphysical local minima of χ^2 corresponding to large displacements of the K$^+$. In this area the K$^+$ shifts have to be constrained by using the values obtained for pions and protons. The resulting K$^+$/π^+ ratios are again compared to data from other experiments [6, 8] which agree well with the results from NA49 at $x_F = 0.3$ presented in Fig. 15b. This confirmation of consistency is necessary, as for higher x_F values the K$^+/\pi^+$ ratio was constrained to that from other measurements. The rapid decrease of the π^+/p ratio to values below 5% at $x_F > 0.55$ imposes, together with the slightly increasing K$^+$/π^+ ratio in this region, a limit on reliable π^+ extraction at $x_F = 0.55$.

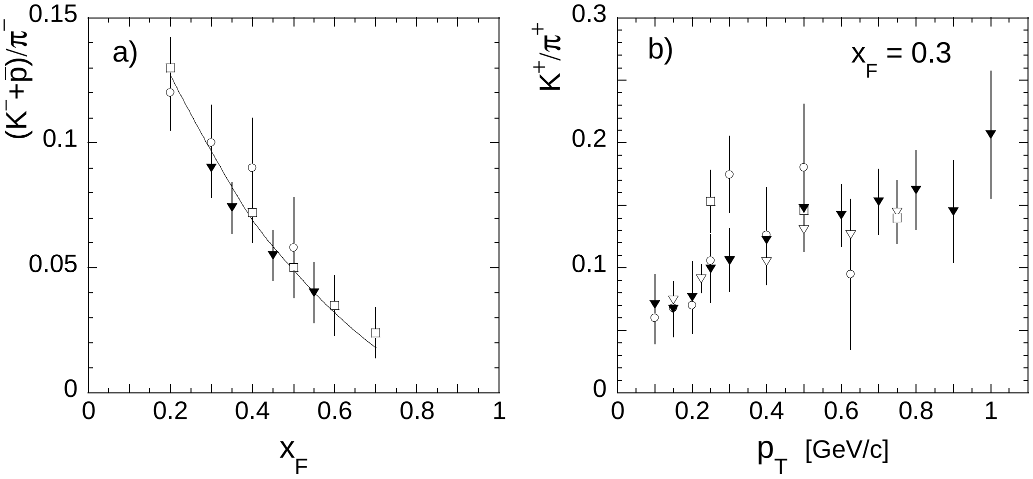

Figure 15: a) (K$^-$+p̄)/π^- ratio as a function of x_F measured by [8] (open circles) and [6] (open squares) compared to NA49 (full triangles), b) K$^+$/π^+ ratio as a function of p_T measured by [8] (open circles and triangles) and [6] (open squares) compared to NA49 (full triangles).

5 Evaluation of Invariant Cross Sections and Corrections

The invariant inclusive cross section is defined as

$$f(x_F, p_T) = E(x_F, p_T) \cdot \frac{d^3\sigma}{dp^3}(x_F, p_T) \tag{6}$$

where dp^3 is the infinitesimal volume element in three dimensional momentum space.

This cross section is approximated by the measured quantity

$$f_{meas}(x_F, p_T, \Delta p^3) = E(x_F, p_T, \Delta p^3) \cdot \frac{\sigma_{trig}}{N_{ev}} \cdot \frac{\Delta n(x_F, p_T, \Delta p^3)}{\Delta p^3} \quad , \tag{7}$$

where Δp^3 is the finite volume element defined by the experimental bin width, σ_{trig} the trigger cross section discussed in Section 3.3, N_{ev} the number of events originating from the liquid hydrogen target, and Δn the number of identified pions from the target measured in the bin Δp^3. In general and for arbitrary functional shapes of $f(x_F, p_T)$, the measured quantity f_{meas} depends on the bin width Δp^3 via E and Δn.

Several steps of normalization and correction are necessary in order to make f_{meas} approach $f(x_F, p_T)$:

- The numbers N_{ev} and Δn have to be determined from the measured full and empty target yields.
- The fact that σ_{trig} is not equal to σ_{inel} necessitates a trigger bias correction.
- Δn has to be corrected for re-interaction of produced particles in the target volume, for weak decay and absorption of pions on their way through the detector, and for feed-down from weak decay of strange particles.
- The finite volume element Δp^3 has to be replaced by the infinitesimal dp^3 which requires a binning correction.

This list defines seven corrections which will be discussed in turn below.

5.1 Empty Target Correction

The particle yield $\Delta n/N_{ev}$ can in principle be determined from separate yield determinations in full and empty target conditions for each bin with the formula

$$\left(\frac{\Delta n}{N_{ev}}\right)^{FT-ET} = \frac{1}{1-\epsilon}\left(\left(\frac{\Delta n}{N_{ev}}\right)^{FT} - \epsilon\left(\frac{\Delta n}{N_{ev}}\right)^{ET}\right) \quad ,$$

where $\epsilon = R_{ET}/R_{FT}$.

In practice the bin-by-bin subtraction would necessitate a large enough event sample from empty target to comply with the statistical precision of the full target data and in addition would give identification problems in the regions of low cross sections where fits to the energy loss distributions anyhow become critical. Given the constraints in data taking of the NA49 experiment and the sizeable reduction of the empty target rate, both evoked and described in Section 3, a more efficient approach is used. For the achieved empty/full target event ratio of 9%, the empty target contribution in terms of track numbers in a given bin is in fact only about 4-5% due to the much larger yield of empty (”zero prong”) events in this sample. In addition the empty target events are mostly of the type p+C and p+air and produce pion yields in the forward (projectile) hemisphere which are very similar to p+p collisions. These points make it possible to extract the cross sections from full target runs alone and to treat the empty target contribution as a small correction. Detailed studies have shown that this correction, which is about 3–4%, is the same for π^+ and π^-, has no measurable p_T dependence, and only a slight variation with x_F. The resulting correction, defined as the ratio of the cross section measured with the proper full-empty subtraction to the one extracted from full target data only, is shown in Fig. 16.

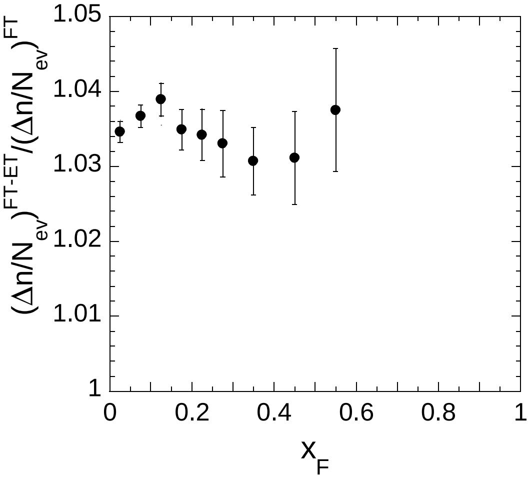

Figure 16: Correction factor applied to account for the empty target contribution as a function of x_F for the average of π^+ and π^-.

5.2 Trigger Bias Correction

As explained in Section 3.3 the interaction trigger defined by the scintillator S4 accepts only 85.6% of the total inelastic cross section. This bias will reflect into the measured cross sections via the expression

$$f_{meas} \sim \sigma_{trig} \cdot \frac{\Delta n}{N_{ev}} \tag{8}$$

in a non-trivial way. It will be zero for all event topologies with no hit of S4, i.e. for the far forward region where – once a particle is detected there – no further particle can reach S4 by energy-momentum conservation. On the other hand, as it has been shown that particle yields completely decouple between the forward and the backward hemispheres [30], the loss of 14.4% should be entirely felt in the backward region. Therefore a dependence on x_F as illustrated in Fig. 17 may be expected, whereas short range correlations should modify this prediction in the forward hemisphere.

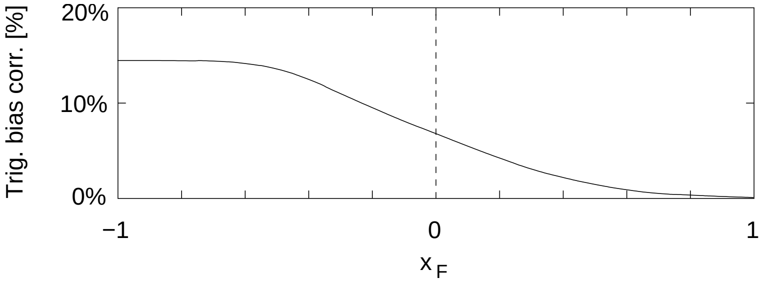

Figure 17: Qualitative expectation of trigger bias correction as a function of x_F.

Detailed correction tables are obtained experimentally by increasing the diameter of the S4 counter off-line and extrapolating the observed change in cross section to surface zero. The method resembles the technique used in transmission experiments and relies entirely on measured quantities. This is important to note as no event generator codes can be expected to be reliable at the level of precision required here. The systematic error from this method is dominated by the statistical error of the evaluation, typically a factor of three smaller than the statistical error of the extracted data.

The resulting trigger bias correction over the kinematic range of the experiment as presented in Fig. 18a and b follows indeed the expectation for p_T values above about 0.6 GeV/c. For smaller p_T a significant micro-structure in the x_F dependence appears which is a reflection of hadronic two-body correlations driven by resonance decay (see also the discussion in Section 10).

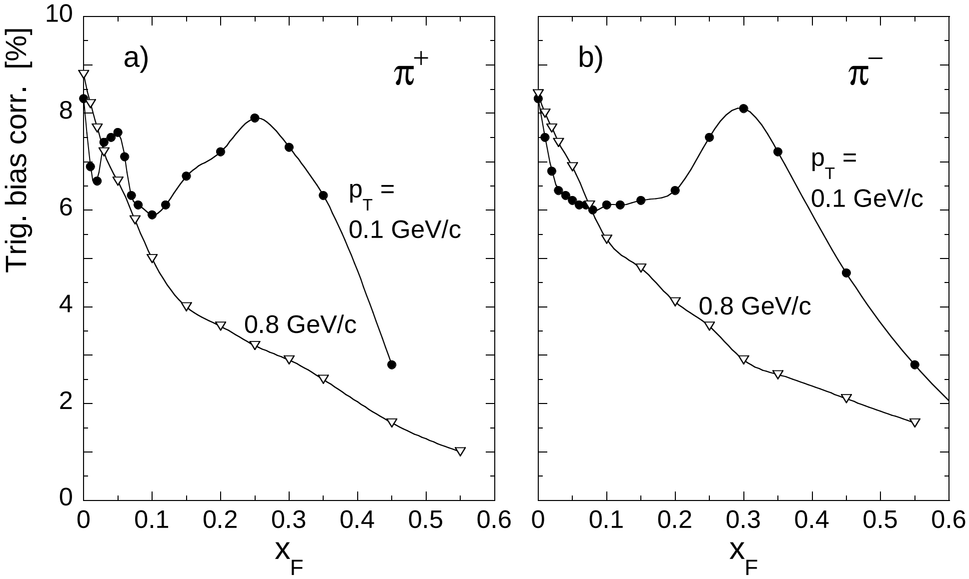

Figure 18: Trigger bias correction as a function of x_F at various p_T for a) π^+ and b) π^-.

5.3 Re-interaction in the Liquid Hydrogen Target

The produced particles will travel through the target material downstream of the primary interaction. Given the 2.8% interaction length of the target for protons, a secondary interaction will occur in about 1.4% of the cases for produced hadrons. The correction for this effect is evaluated using the PYTHIA event generator [31], assuming that all daughter particles from these secondary interactions are reconstructed at the primary vertex. As hadronic interactions will also produce pions, not only make them vanish, the correction factor is > 1.0 in the high x_F region and < 1.0 in the low x_F region where pion production dominates. The x_F dependence of the correction is shown in Fig. 19.

5.4 Absorption in Detector Material

The correction for pions interacting in the downstream material of the detector is determined using the GEANT simulation of the NA49 detector. Based on eye-scans it is assumed that all primary pions undergoing hadronic interactions before detection are lost. This assumption largely simplifies the analysis, and given the small value of the correction even in the critical regions of phase space, it introduces only a small systematic error. The absorption correction as a function of x_F at two p_T values is shown in Fig. 20. At low p_T the x_F dependence exhibits multiple maxima which correspond to the position of the ceramic support tubes of the TPC field cages [24].

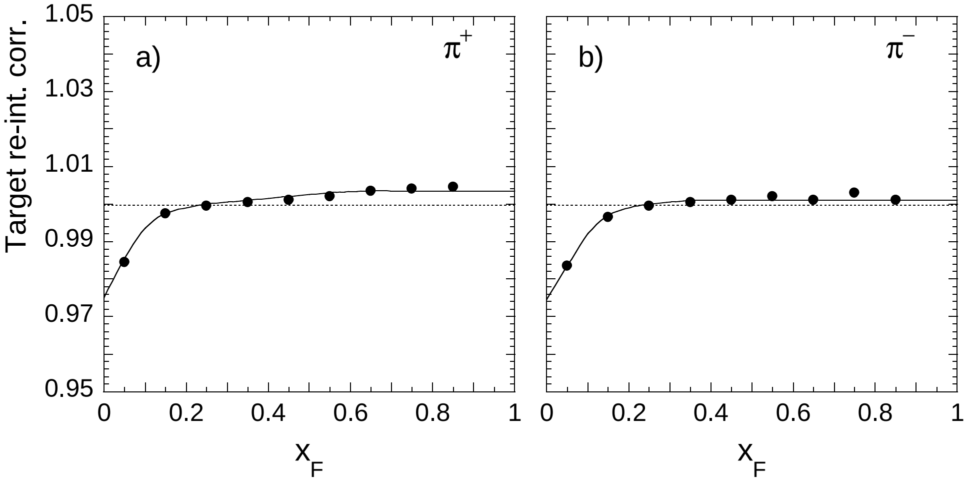

Figure 19: Correction factor applied accounting for the target re-interaction of produced particles.

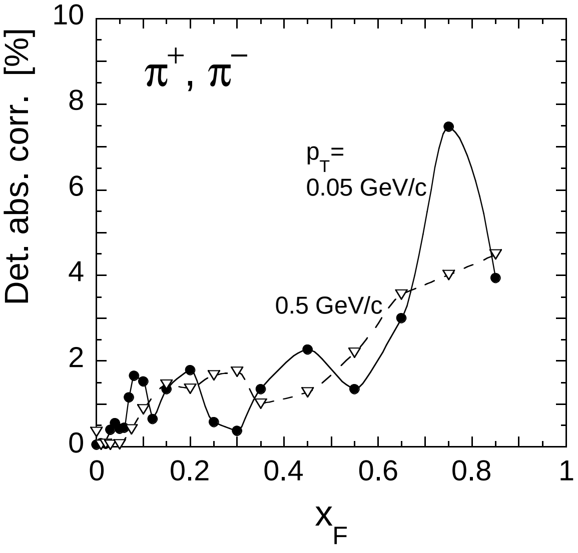

Figure 20: Correction due to absorption of produced pions in the downstream detector material.

5.5 Pion Weak Decay

Due to the sizeable decay length of pions in the weak channel $\pi \rightarrow \mu + \nu_\mu$ only a small fraction of pions will decay on their way through the detector, ranging from a maximum of 3.6% at the smallest detected p_{lab} at x_F and $p_T = 0.0$ to less than 0.5% for $p_{lab} > 10$ GeV/c. The bulk of these decays will cause neither a loss of the particle track nor a misidentification problem. The dip angle of the muon track which is most critical for its reconstruction at the primary vertex deviates less than 1° from the pion direction at the lowest energy, and the muon takes on average about 80% of the pion momentum. Muons from decays in front of the detector in the field-free or stray field regions are therefore reconstructed at vertex. The same applies for decays downstream of VTPC-2. The only sample contributing to track losses corresponds to decays inside the magnetic field before the primary track has left the necessary 30 points for analysis and where the secondary track escapes reconstruction. The tracking inefficiency for this sample, which amounts to 1.5% of pions at the lowest detected momentum, is determined to about 20% ± 10%, by making use of the total fraction of tracks with less than about 30 points in the low momentum range. This low inefficiency was confirmed by detailed eye-scans, showing that secondary interactions or kaon decays are the primary source of these short tracks, and not pion weak decays. The resulting correction decreases rapidly with increasing laboratory momentum from a maximum value of 0.36% at x_F and $p_T = 0$ as shown in Fig. 21.

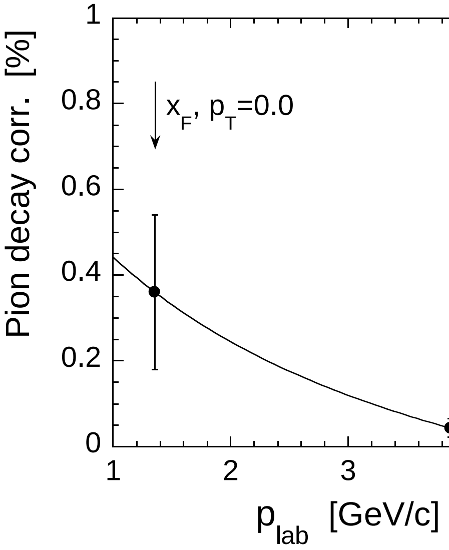

Figure 21: Correction (close to $1/p$) due to the weak decay of pions.

As far as particle identification is concerned, muons appear shifted upwards by about one standard deviation from the pion position in the energy loss distribution. This small deviation is absorbed in the independent fit of position and width of the pion peak in each bin.

5.6 Feed-down to Pions from Weak Decays of Strange Particles

It may in principle be a matter of discussion whether decay pions from weak decays of strange particles should be subtracted or counted into the total sample. In bubble chamber experiments with usually a small detector size, most decays escape detection via too long decay lengths. For decays inside the fiducial volume, secondary vertices are readily detected and the corresponding decay particles eliminated from the sample. For counter experiments the situation is less clear. In fixed target geometry the detectors are long enough to see a sizeable fraction of the decay daughters and vertex fitting is usually not precise enough to eliminate all secondary vertices. In the early collider experiments at the ISR one can start with the assumption that almost all decay products are counted into the track sample. In fact none of the experiments compared to the present data, see Section 8, has attempted a feed-down correction. As feed-down pions are mostly concentrated at low p_T and low x_F the case is saved by the fact that these experiments usually have no acceptance in these regions.

In view of this situation and as the present experiment has full acceptance in the critical areas of phase space, a complete feed-down subtraction is performed by considering all relevant sources, i.e. $\mathrm{K}^0_s, \Lambda, \Sigma^+, \Sigma^-, \bar{\Lambda}$. The main source of systematic uncertainty is the very limited knowledge of the corresponding production cross sections.

The correction is determined in three steps. First, the double-differential parent distributions are adjusted to existing data. With this input, in the second step, a decay Monte Carlo is used to predict yields of daughter particles in the x_F/p_T bins of the experiment. These yields are, in the third step, folded with the reconstruction efficiency which is obtained from a detailed NA49 detector simulation using complete generated events containing the appropriate strange hadrons.

The p_T integrated density distributions of parent particles are shown in Fig. 22 as a function of x_F. The corresponding p_T distributions are extracted for K^0_s from averaged charged kaon data and for Λ from a combined set of bubble chamber, NA49 and ISR data [32].

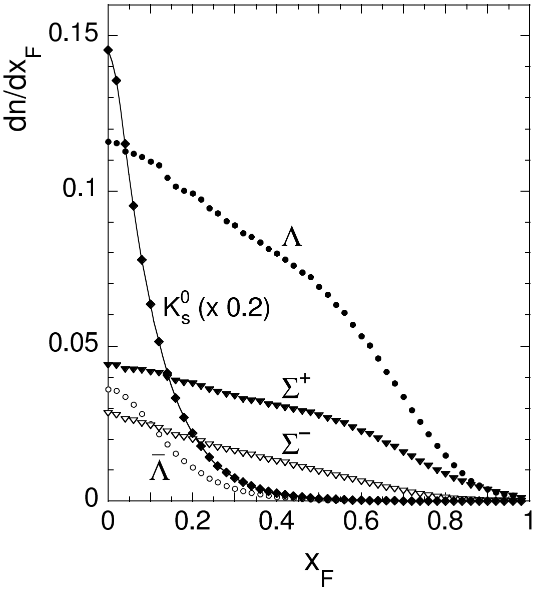

Figure 22: p_T integrated density distribution dn/dx_F of parent particles contributing to the feed-down correction.

The reconstruction efficiency for the daughter pions, determined from a full GEANT simulation of the NA49 detector using VENUS for the input distributions, is defined as the ratio of reconstructed vertex tracks in a given analysis bin to the daughter tracks emitted to the same bin. As such, this ratio can reach values above 1.0. It has been verified that the efficiency is only depending weakly on the input parent-particle distribution, and can therefore be used as a multiplicative factor.

The average reconstruction efficiency reaches levels of up to 50% in the low x_F region. It is rather independent of p_T but shows a strong variation with the azimuthal angle which is due to biases in the fitting of decay products to the primary vertex. This is exemplified in Fig. 23 which shows the azimuthal dependence for Lambda decay to pions with $p_{lab} = 3.2$ GeV/c in different bins of p_T. This observation leads to the restriction of the Φ window in bins which have otherwise full acceptance for vertex tracks (see Section 3.6).

The resulting total feed-down correction for π^+ and π^- is presented in Fig. 24 as a function of x_F for various p_T bins. Apparently this correction is very sizeable especially at low p_T and extends rather far up in x_F with a complex overall structure. Therefore it is no question that great care has to be taken in comparing experiments with undefined feed-down treatment in these areas.

5.7 Binning Correction

The extraction of invariant cross sections has by necessity to be performed in finite bins of phase space. The measured yield is therefore the integral of the particle density over the phase

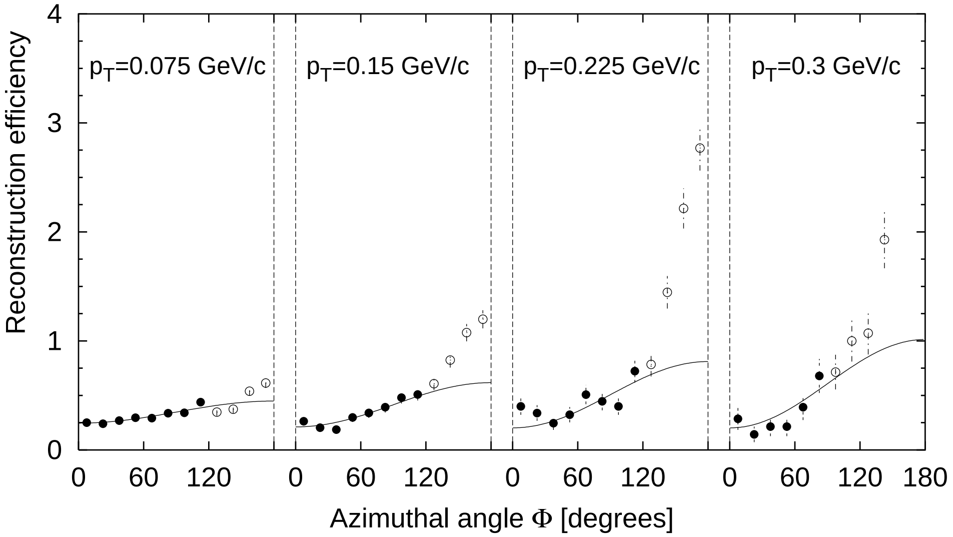

Figure 23: Reconstruction efficiency for pions with $p_{lab} = 3.2$ GeV/c from Λ decay as a function of Φ for various p_T values. The Φ region chosen for pion extraction is indicated by full symbols, where $\Phi = 0$ is in the horizontal plane.

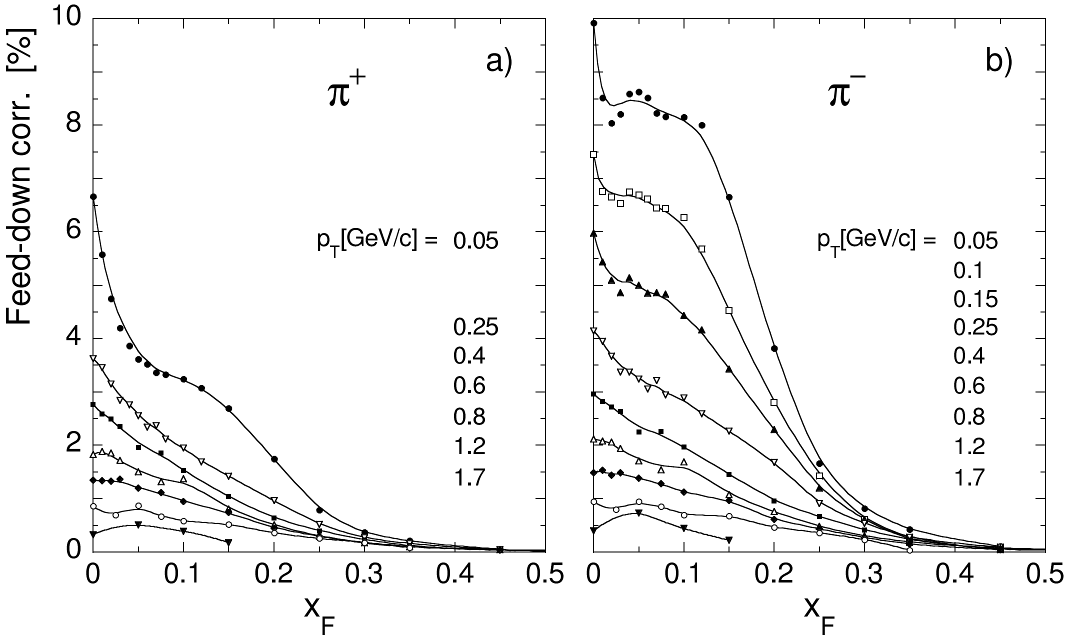

Figure 24: Correction of feed-down to pions from weak decays for a) π^+ and b) π^-.

space volume element. As the density distribution as a function of the azimuthal angle is flat by symmetry, the problem reduces to a determination of binning corrections in x_F and p_T.

Approximating the variation of particle density ρ in the coordinate t by an expansion in local derivatives,

$$\rho(t) \approx \rho(t_0) + \rho'(t_0)(t - t_0) + \rho''(t_0)\frac{(t - t_0)^2}{2}$$

the measured value corresponding to the bin center t_0 is

$$\rho_{meas}(t_0) = \frac{1}{\Delta}\int_{t_0-\Delta/2}^{t_0+\Delta/2} \rho(t)\mathrm{d}t \approx \rho(t_0) + \frac{1}{24}\rho''(t_0)\Delta^2$$

up to second order terms, where Δ is the bin width. Hence the difference between the real particle density at t_0 and its measured value is proportional to the second derivative of the density function and to the square of the bin width. This approximation holds if the difference does not exceed the level of a few percent.

For the functional forms discussed here the second derivative may be approximated from neighbouring data points by

$$\rho''(t_0) \approx \left(\left(\frac{\Delta_1 \rho(t_2) + \Delta_2 \rho(t_1)}{\Delta_1 + \Delta_2} \right) - \rho(t_0) \right) \frac{2}{\Delta_1 \Delta_2} \ ,$$

where $\Delta_1 = t_1 - t_0$ and $\Delta_2 = t_0 - t_2$.

The generalization of the method to the case of double differential cross sections is straightforward and it can be shown that the correction can be determined independently in the two coordinates.

The above consideration defines the binning correction, which can be evaluated for all data points if statistics permits an estimation of the second derivative. The statistical uncertainty induced by the correction, determined by the error of neighbouring points, is about a factor of 10 lower than the error of the data points itself. The direct application of the correction makes it model or parametrization independent.

The correction is on the 1–4% level as shown in Fig. 25 for some typical p_T and x_F dependences. In fact, one of the important aspects in the elaboration of the binning scheme, see Section 3.7, is to keep this correction low in the high statistics regions in order to capture the structures of the density function in an optimum fashion. The remaining systematic error from neglecting higher terms is below 0.5% as verified by Monte Carlo studies.

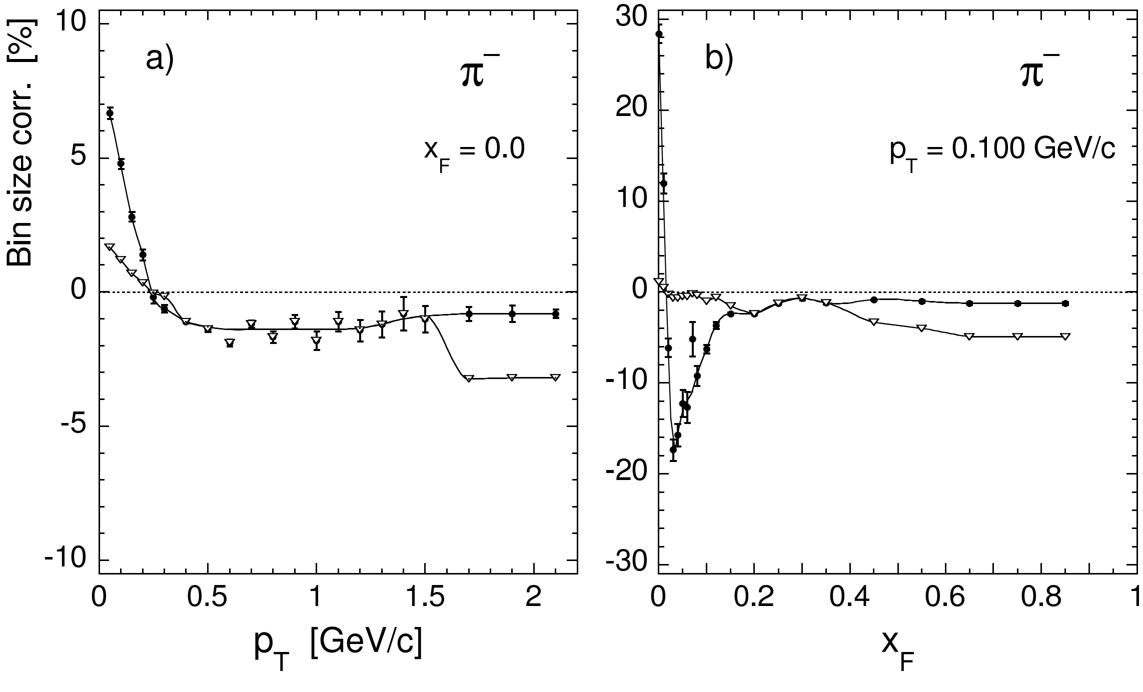

Figure 25: Correction due to the binning in a) p_T and b) x_F. Full circles represent the correction for a fixed bin of $\Delta p_T = 0.1$ GeV/c and $\Delta x_F = 0.05$, respectively; open triangles describe the correction for the bin sizes actually used.

6 Systematic Errors

In addition to the overall normalization uncertainty, the corrections discussed in Section 5 introduce systematic errors which are estimated by allowing appropriate error bands for the underlying physics inputs. The corresponding values are given in Table 3. By summing up all contributions, an upper limit of 4.8% for the total systematic uncertainty can be claimed.

Normalization	1.5 %
Tracking efficiency	0.5 %
Trigger bias	0.5 %
Feed-down	0.5–1.5 %
Detector absorption Pion decay $\pi \to \mu + \nu_\mu$ Re-interaction in target	0.5 %
Binning	0.3 %
Total (upper limit)	4.8 %
Total (quadratic sum)	2.0 %

Table 3: Summary of systematic errors.

It should be noted that in the high x_F region where certain assumptions have to be made on K^+/π^+ and K^-/π^- ratios for the purpose of particle identification, additional systematic uncertainties of between 1 and 3% have to be added.

Further information on the error sources is contained in Fig. 26 which gives the distributions of each single correction and of the resulting total correction for the 589 data points of this

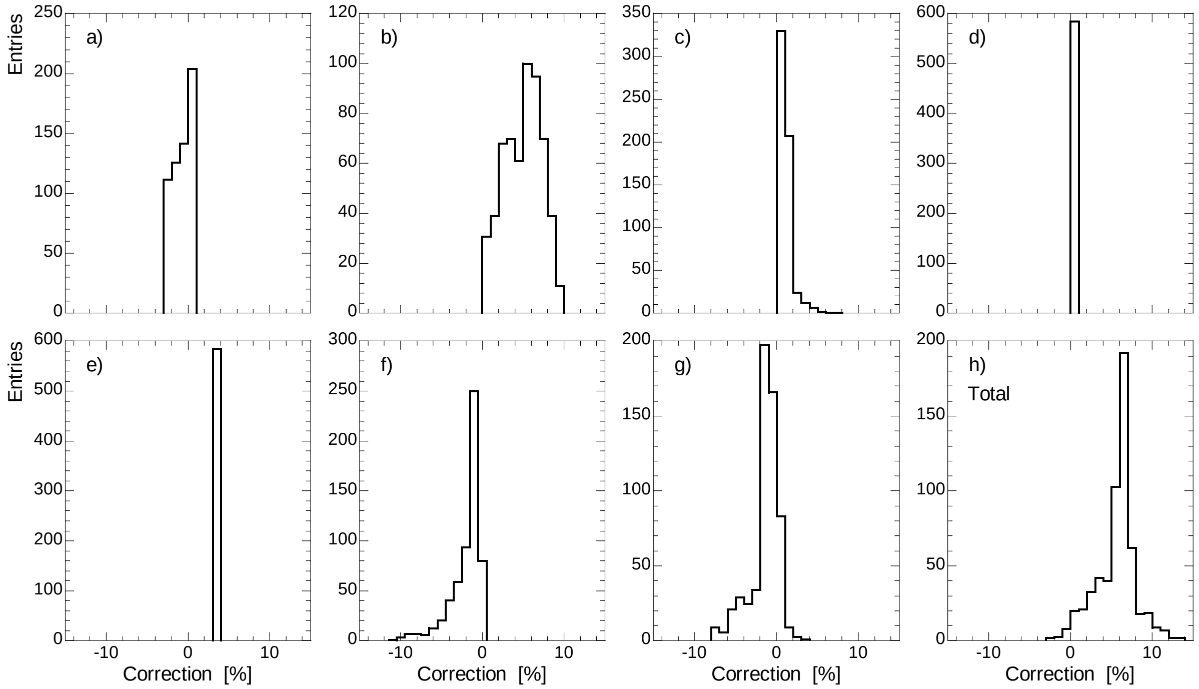

Figure 26: Distribution of correction for a) target re-interaction, b) trigger bias, c) absorption in detector material, d) pion decay, e) empty target contribution, f) feed-down, g) binning, and h) resulting total correction.

experiment. It appears that the individual corrections compensate to a large extent in the overall result so that only few points had to be corrected by more than 10%. This might give some support to the estimation of the total systematic error as the sum of the squares to only 2%. This low value has to be regarded with some caution since the authors are the first to recognize that this way of minimizing possible systematic uncertainties has been in the past, one of the major difficulties in the quantitative comparison of hadronic cross sections. Finally, only comparison between different independent measurements can help to understand the problem of systematic error propagation. This comparison will be attempted in Sections 8 and 9 below.

7 Results

The following chapter presents the double differential invariant cross sections for charged pions resulting from the event sample and from the extraction and correction procedures discussed above. The basic numerical information is summarized in data tables. The completeness and the small statistical and systematic errors of these data allow the identification of a complex structure in their dependence on the kinematic variables which cannot be parametrized by straight-forward arithmetic expressions. A numerical interpolation scheme has therefore been developed. The resulting curves are presented together with the data points in p_T distributions at fixed x_F, in x_F distributions at fixed p_T, and in corresponding π^+/π^- distributions. Finally, the cross sections are also shown in their dependence on rapidity y and transverse mass m_T.

7.1 Data Tables

The following Tables summarize the double differential invariant cross sections as a function of x_F and p_T for the binning scheme discussed in Section 3.7 above. This scheme results in 281 measured values for π^+ (Table 4) and 308 values for π^- (Table 5) production, the difference for the two charges being due to the limitation of π^+ identification in the region above $x_F = 0.55$ (see Section 4.5).

The detailed structure of the data tables results from the attempt to cover as completely as possible the available phase space with bins which comply with the statistical errors of the data spanning five orders of magnitude in cross section.

7.2 Interpolation Scheme

Although the data binning has been chosen to correspond to well defined bin centers in x_F and p_T, it is desirable to also offer an interpolation scheme which produces smooth overall x_F and p_T dependences for the internal extension of the data to non-measured intermediate values and for comparison with other data measured at different x_F and p_T values. Any attempt at such numerical interpolation meets with the problem that the dense phase space coverage combined with the small statistical errors of the data reveals a microstructure both in the p_T and x_F dependences which makes a description with arithmetic parametrizations if not impossible, then at least incompatible with the data quality. A multistep manual interpolation method is therefore selected which relies on local continuity of the cross sections both in the p_T and x_F variables and which complies with the statistical accuracy of the data points. The final result can be controlled by evaluating the distribution of the differences between data and interpolated values, divided by the statistical error of each data point. This distribution should be a Gaussian centered at zero and with variance unity if the interpolation scheme does not introduce a bias. As shown in Fig. 27 this is indeed the case for the 589 data points of this experiment.

$f(x_F,p_T)$ Δf										
$p_T\backslash x_F$	0.0	0.01	0.02	0.025	0.03	0.04	0.05	0.06	0.07	0.075
0.050	62.87 0.61	62.79 0.66	59.44 0.65		51.53 0.63	43.29 0.63	37.64 0.75	32.64 0.86	29.78 0.98	
0.100	59.66 0.58	58.91 0.62	54.55 0.48		51.49 0.54	45.19 0.54	41.09 0.63	36.46 0.73	32.92 0.81	
0.150	51.20 0.55	50.87 0.58	47.98 0.55		45.66 0.58	42.21 0.48	39.68 0.54	36.39 0.59	34.55 0.67	
0.200	41.42 0.65	40.78 0.49	39.58 0.51		37.37 0.56	35.33 0.54	33.69 0.50	31.49 0.58	29.16 0.63	
0.250	32.00 0.57	31.93 0.53	30.47 0.55		29.47 0.61	27.77 0.53	26.54 0.60	25.04 0.68	23.80 0.63	
0.300	24.11 0.49	23.89 0.62	23.03 0.60		22.00 0.67	21.35 0.69	20.37 0.62	19.44 0.71	18.71 0.68	
0.400	13.20 0.57	13.21 0.57	12.76 0.58		12.11 0.61		11.56 0.43			10.89 0.35
0.500	7.212 0.77	7.297 0.78	7.046 0.80		6.690 0.85		6.423 0.59			6.033 0.62
0.600	4.102 1.02	3.920 1.07	3.923 1.06		3.723 1.11		3.585 0.77			3.356 0.79
0.700	2.219 1.41	2.233 1.40	2.170 1.43		2.027 1.52		2.007 1.01			1.924 1.11
0.800	1.213 1.86	1.259 1.87	1.183 1.89		1.148 1.94		1.156 1.30			1.082 1.38
0.900	0.689 2.49	0.681 2.51	0.702 2.43		0.692 2.47		0.652 1.96			0.607 1.93
1.000	0.386 3.31	0.397 3.22	0.383 3.33		0.383 3.32		0.379 2.54			0.368 2.62
1.100	0.248 2.60			0.236 3.48			0.223 3.35			0.219 3.42
1.200	0.136 3.54			0.135 4.57			0.120 4.32			0.128 4.17
1.300	0.0797 4.56			0.0750 6.07			0.0729 5.55			0.0734 5.67
1.400	0.0482 5.99			0.0448 8.04			0.0443 6.97			0.0473 6.58
1.500	0.0296 7.61			0.0277 9.96			0.0302 8.45			0.0266 9.20
1.700	0.0122 6.14						0.0115 6.76			
1.900	0.00406 10.2						0.00373 11.9			
2.100	0.00172 15.4						0.00149 18.8			
$p_T\backslash x_F$	0.08	0.1	0.12	0.15	0.2	0.25	0.3	0.35	0.45	0.55
0.050	27.71 1.07	24.05 0.92	22.01 1.04	19.13 0.92	17.35 1.08	15.80 1.57	11.80 2.06	7.690 2.75	3.720 3.18	
0.100	29.30 0.91	25.11 0.77	22.98 0.89	20.40 0.78	16.72 0.93	14.59 1.35	11.23 1.81	6.811 2.11	3.734 2.23	
0.150	30.72 0.75	26.17 0.63	23.42 0.75	20.15 0.65	16.16 0.78	12.87 1.16	9.319 1.68	5.970 1.82	3.266 1.94	
0.200	27.80 0.67	24.38 0.59	21.57 0.67	18.40 0.59	13.64 0.73	10.84 1.10	7.535 1.57	5.169 1.67	2.812 1.82	1.683 2.32
0.250	22.94 0.66	20.16 0.59	18.06 0.67	15.33 0.57	11.59 0.71	8.601 1.17	6.478 1.55	4.354 1.62	2.435 1.75	
0.300	18.18 0.71	16.19 0.60	14.57 0.67	12.59 0.58	9.413 0.72	7.164 1.14	5.146 1.57	3.659 1.61	1.970 1.79	1.198 2.18
0.400		10.00 0.42		8.047 0.40	6.189 0.61	4.754 0.85	3.514 1.16	2.590 1.18	1.388 1.29	0.853 3.58
0.500		5.749 0.50		5.026 0.46	4.040 0.68	3.204 0.93	2.367 1.25	1.812 1.28	0.949 1.37	0.538 3.94
0.600		3.186 0.64		2.874 0.65	2.561 0.77	2.071 1.06	1.681 1.38	1.313 1.38	0.660 1.49	0.349 4.59
0.700		1.770 1.02		1.623 0.83	1.452 1.02	1.272 1.25	1.006 1.63	0.863 1.58	0.482 1.67	0.227 5.29
0.800		1.027 1.45		0.905 1.04	0.806 1.29	0.697 1.58	0.608 1.98	0.490 1.96	0.305 1.98	0.148 6.20
0.900		0.576 2.03		0.516 1.35	0.471 1.63	0.398 2.01	0.304 2.64	0.281 2.47	0.188 2.39	0.0956 7.24
1.000		0.356 2.40		0.298 1.71	0.252 2.14	0.219 2.56	0.181 3.27	0.158 3.14	0.101 3.10	0.0592 8.74
1.100		0.203 3.67		0.176 2.41	0.155 2.72	0.130 3.18	0.113 3.98	0.0802 4.16	0.0514 4.07	0.0326 7.89
1.200		0.125 4.27		0.106 3.36	0.0876 3.49	0.0739 4.11	0.0555 5.46	0.0497 5.09	0.0290 5.27	
1.300		0.0701 6.07		0.0653 4.54	0.0530 4.47	0.0482 5.16	0.0405 6.20	0.0274 6.74	0.0189 6.38	0.00724 15.1
1.400		0.0416 7.65		0.0405 5.59	0.0295 7.45	0.0246 6.72	0.0234 7.92	0.0169 8.28	0.0116 7.74	
1.500		0.0290 9.23		0.0258 7.49	0.0204 7.79	0.0179 9.45	0.0138 4.93	0.0110 7.01	0.00612 8.78	0.00214 26.7
1.700		0.00981 7.56		0.0114 7.78	0.00720 9.78	0.00615 10.5	0.00527 7.69	0.00448 10.5	0.00315 11.8	
1.900		0.00339 12.7		0.00374 13.9	0.00323 13.7		0.00273 10.3	0.00209 17.7		
2.100				0.00215 17.3	0.00151 22.6			0.00110 24.5		

Table 4: Double differential invariant cross section $f(x_F, p_T)$ [mb/(GeV^2/c^3)] for π^+ produced in p+p interactions at 158 GeV/c. The statistical uncertainty Δf is given in %.

	$f(x_F, p_T)$ Δf									
$p_T \backslash x_F$	0.0	0.01	0.02	0.025	0.03	0.04	0.05	0.06	0.07	0.075
0.050	59.19 0.52	55.36 0.57	49.58 0.69		41.35 0.70	35.72 0.67	30.52 0.81	26.76 0.93	23.79 1.05	
0.100	54.40 0.48	52.21 0.52	47.69 0.49		41.32 0.57	35.95 0.59	31.55 0.71	27.53 0.81	24.76 0.91	
0.150	46.74 0.47	45.73 0.48	41.85 0.57		37.78 0.63	34.21 0.51	30.42 0.61	27.50 0.68	24.47 0.77	
0.200	37.85 0.53	36.91 0.51	34.65 0.55		31.96 0.62	29.26 0.57	26.45 0.55	24.03 0.65	22.16 0.71	
0.250	29.00 0.59	28.74 0.55	26.68 0.59		25.41 0.66	23.56 0.58	21.70 0.68	19.90 0.74	18.51 0.69	
0.300	22.02 0.68	22.25 0.67	20.62 0.67		19.51 0.70	18.26 0.75	16.87 0.69	15.98 0.79	14.91 0.71	
0.400	12.28 0.61	12.05 0.62	11.63 0.55		10.75 0.59		10.05 0.45			8.853 0.39
0.500	6.673 0.80	6.371 0.83	6.296 0.84		5.946 0.91		5.697 0.63			5.069 0.67
0.600	3.498 1.10	3.542 1.11	3.507 1.12		3.261 1.20		3.147 0.81			2.849 0.86
0.700	2.016 1.44	1.959 1.47	1.893 1.51		1.852 1.55		1.705 1.06			1.616 1.19
0.800	1.098 1.95	1.089 1.96	1.101 1.94		1.049 2.03		0.982 1.41			0.940 1.48
0.900	0.641 2.51	0.616 2.59	0.622 2.57		0.570 2.80		0.567 2.08			0.529 2.02
1.000	0.346 3.37	0.372 3.43	0.341 3.43		0.336 3.48		0.318 2.68			0.307 2.79
1.100	0.209 3.09			0.215 3.64			0.190 3.35			0.181 3.53
1.200	0.122 3.67			0.117 4.91			0.111 4.52			0.0982 5.38
1.300	0.0784 4.64			0.0686 6.49			0.0597 6.04			0.0582 6.39
1.400	0.0469 5.91			0.0411 8.23			0.0372 7.76			0.0329 8.41
1.500	0.0242 8.33			0.0262 10.5			0.0232 9.59			0.0212 10.5
1.700	0.0102 6.25						0.00785 8.09			
1.900	0.00399 10.3						0.00344 12.2			
2.100	0.00124 27.4						0.00162 17.7			
$p_T \backslash x_F$	0.08	0.1	0.12	0.15	0.2	0.25	0.3	0.35	0.45	0.55
0.050	21.27 1.19	17.41 1.04	14.35 1.26	11.31 1.16	7.564 1.55	6.064 2.36	4.669 3.32	3.007 4.44	1.418 5.09	
0.100	21.39 1.06	17.17 0.90	14.49 1.08	11.40 1.02	7.652 1.33	5.802 1.97	4.429 2.94	2.964 3.17	1.494 3.52	0.528 5.91
0.150	21.66 0.87	17.62 0.78	14.45 0.96	11.23 0.84	7.367 1.11	5.539 1.63	3.971 2.51	2.712 2.66	1.300 3.07	
0.200	20.30 0.79	16.41 0.71	13.62 0.87	10.63 0.76	6.743 1.00	4.839 1.51	3.453 2.30	2.191 2.57	1.191 2.79	0.550 4.20
0.250	17.28 0.80	14.32 0.67	12.03 0.81	9.195 0.73	5.986 0.95	4.334 1.52	2.872 2.31	2.152 2.30	0.978 2.71	
0.300	13.89 0.77	12.27 0.70	10.08 0.75	8.226 0.71	5.279 0.92	3.795 1.47	2.538 2.21	1.689 2.37	0.875 2.28	0.432 3.90
0.400		7.674 0.48		5.567 0.48	3.892 0.76	2.741 1.06	1.914 1.57	1.286 1.66	0.637 2.30	0.267 4.23
0.500		4.524 0.57		3.485 0.54	2.646 0.83	1.908 1.14	1.366 1.66	0.927 1.75	0.429 2.49	0.194 4.46
0.600		2.564 0.71		2.133 0.75	1.670 0.96	1.258 1.28	0.958 1.82	0.676 1.89	0.305 2.68	0.133 4.88
0.700		1.492 1.15		1.225 0.92	1.010 1.20	0.788 1.50	0.600 2.13	0.441 2.18	0.211 2.99	0.0821 5.73
0.800		0.867 1.60		0.686 1.18	0.590 1.49	0.474 1.84	0.364 2.55	0.265 2.63	0.135 3.55	0.0627 6.15
0.900		0.472 2.25		0.401 1.48	0.328 1.90	0.270 2.29	0.226 3.07	0.165 3.15	0.0840 4.22	0.0345 7.78
1.000		0.264 2.81		0.234 1.88	0.181 2.45	0.159 2.86	0.133 3.80	0.0971 3.89	0.0524 5.34	0.0185 10.1
1.100		0.174 3.68		0.139 2.69	0.115 2.99	0.0880 3.71	0.0779 4.77	0.0553 4.90	0.0315 5.41	0.0126 8.19
1.200		0.105 5.10		0.0803 3.65	0.0680 3.78	0.0514 4.67	0.0421 6.38	0.0332 6.14		
1.300		0.0606 6.51		0.0499 4.99	0.0401 4.80	0.0332 5.63	0.0247 7.93	0.0187 7.93	0.0103 6.39	0.00463 12.6
1.400		0.0420 7.67		0.0320 6.09	0.0225 7.27	0.0186 7.35	0.0136 10.7			
1.500		0.0201 11.1		0.0196 8.76	0.0131 9.13	0.0137 10.5	0.00879 6.22	0.00676 6.13	0.00439 8.92	0.00104 24.9
1.700		0.00868 8.05		0.00885 8.78	0.00488 11.1	0.00466 11.2	0.00338 9.64	0.00276 9.43	0.00127 17.6	0.00052 33.2
1.900		0.00254 14.6		0.00255 16.5	0.00197 17.0		0.00114 16.5			
2.100				0.00071 30.9	0.00101 23.3					
$p_T \backslash x_F$	0.65	0.75	0.85							
0.100	0.221 7.4	0.0588 15.8	0.0259 25.0							
0.300	0.149 5.1	0.0409 10.6	0.0111 21.8							
0.500	0.0582 6.3	0.0199 11.5	0.00421 26.7							
0.700	0.0282 7.9	0.00742 16.0	0.00236 30.0							
0.900	0.0142 9.5	0.00250 24.3	0.00116 37.6							
1.100	0.00517 14.3	0.00185 25.8	0.00014 100							
1.300	0.00161 23.5	0.00074 37.3	0.00012 100							
1.500	0.00048 41.7	0.00019 68.4								
1.700	0.00014 71.4									

Table 5: Double differential invariant cross section $f(x_F, p_T)$ [mb/(GeV^2/c^3)] for π^- produced in p+p interactions at 158 GeV/c. The statistical uncertainty Δf is given in %.

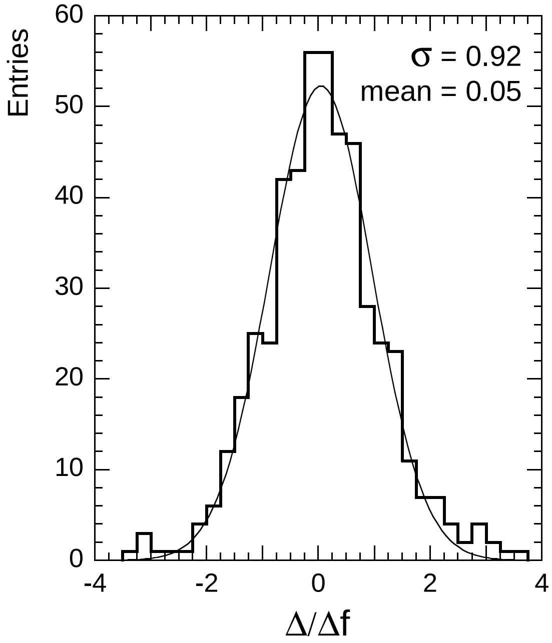

Figure 27: Histogramme of the differences Δ between the measured invariant cross sections and the corresponding interpolated values (π^+ and π^- combined) divided by the experimental uncertainty Δf of the data points.

In the Figures shown in the subsequent Sections, the interpolation for π^+ is extended beyond the region of identification, $x_F > 0.55$, by using data from experiments at ISR energies. This is discussed and justified in Section 8.2.

7.3 Dependence of Cross Section on p_T and x_F

The general behaviour of the invariant cross section as a function of p_T at fixed x_F is presented in Fig. 28. In order to clearly bring out the shape evolution and to avoid overlapping of the interpolated curves and error bars, the values at subsequent x_F values are multiplied by factors of typically 0.5 as given in the figure caption.

The observed p_T dependence is definitely not describable by a simple overall exponential parametrization at any value of x_F, unless one wants to introduce local exponential slope parameters for small regions of p_T. In addition, distinct structures are found at low p_T and $x_F < 0.3$ and in the p_T range from 0.5 to 1 GeV/c for $x_F > 0.25$. The structure at low p_T is shown in more detail in the linear plots of Fig. 29 where a local maximum at $p_T \simeq 0.15$ GeV/c is seen to develop in the region $0.03 < x_F < 0.2$. This maximum is less pronounced for π^- than for π^+.

Corresponding x_F distributions at fixed values of p_T are presented in Fig. 30. Again in order to clarify the overall shape development, the curves for the three lowest p_T values 0.050, 0.100 and 0.150 GeV/c are multiplied by different factors specified in the figure caption.

The low p_T region is magnified in the plots of Fig. 31 where the measured cross sections are displayed without multiplication. A complicated cross-over pattern with several inflexion points is evident for p_T values below 0.3 GeV/c which is again less developed for π^- than for π^+.

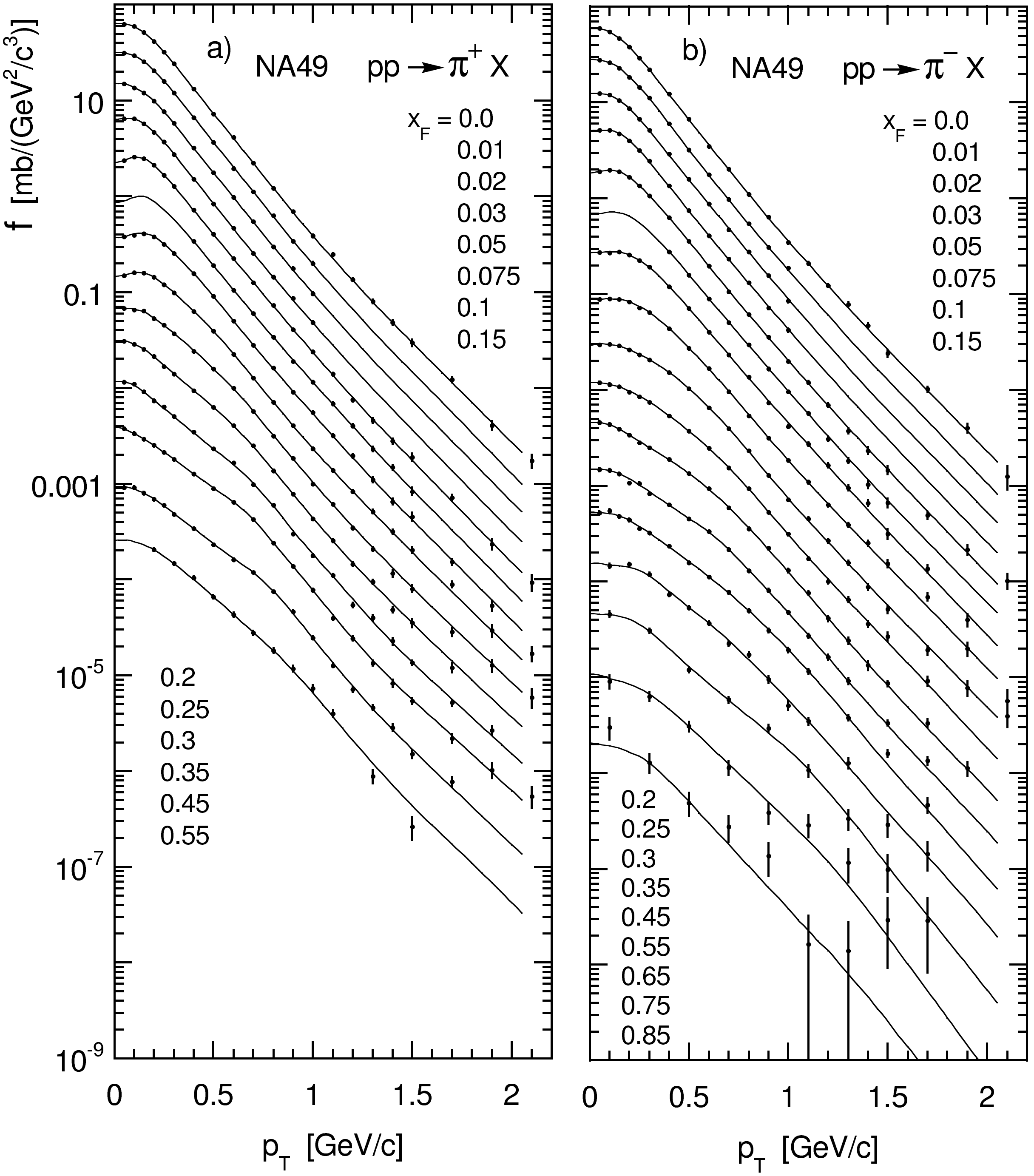

Figure 28: Invariant cross section as a function of p_T at fixed x_F for a) π^+ and b) π^- produced in p+p collisions at 158 GeV/c. Data and lines are multiplied successively by 0.5 for π^+ and by 0.5 up to $x_F = 0.35$ and 0.75 for $x_F \geq 0.45$ for π^- to allow for a better separation.

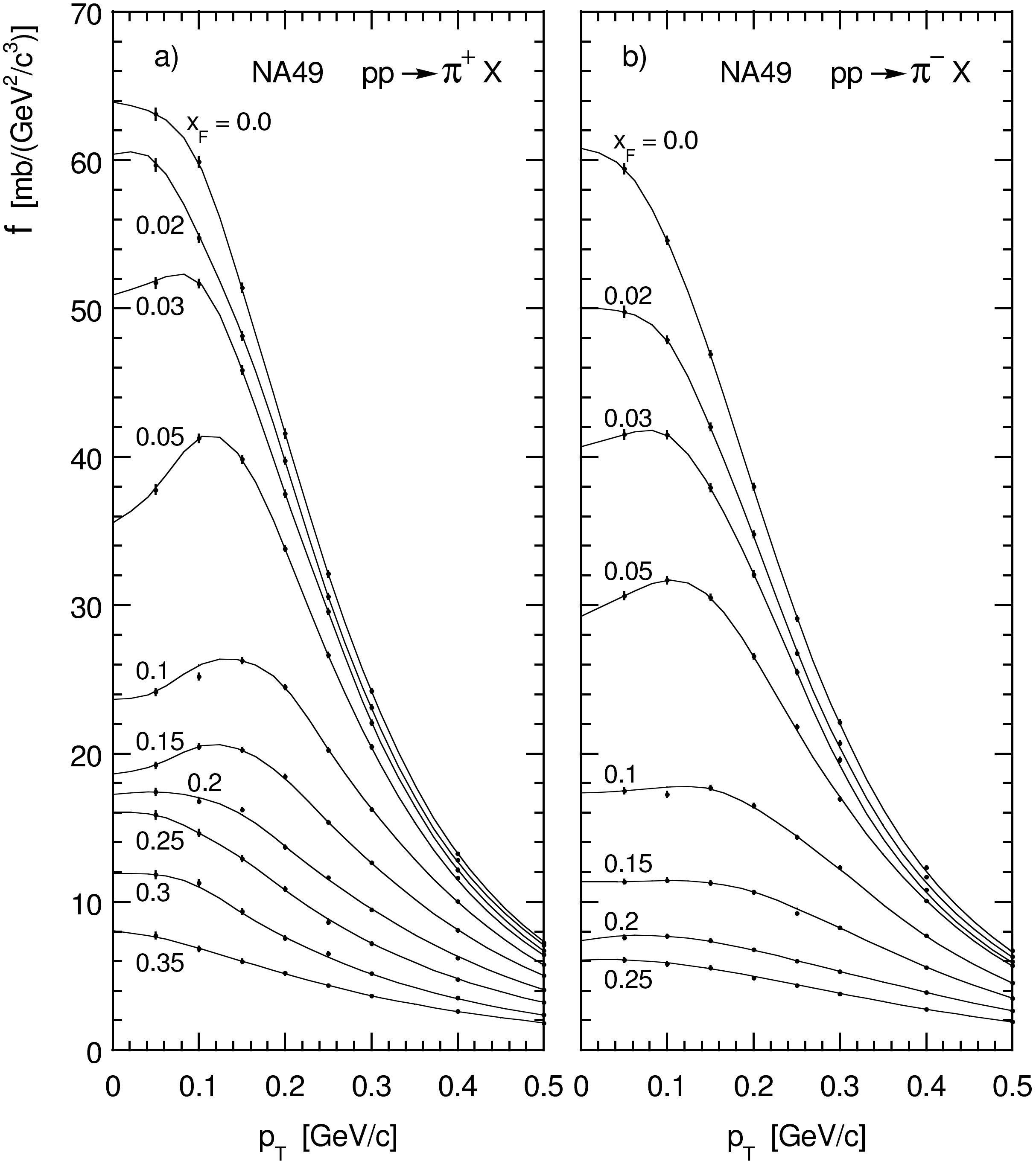

Figure 29: Invariant cross section as a function of p_T at fixed x_F for a) π^+ and b) π^- produced in p+p collisions at 158 GeV/c. The behaviour in the low p_T region is emphasized by using a linear scale.

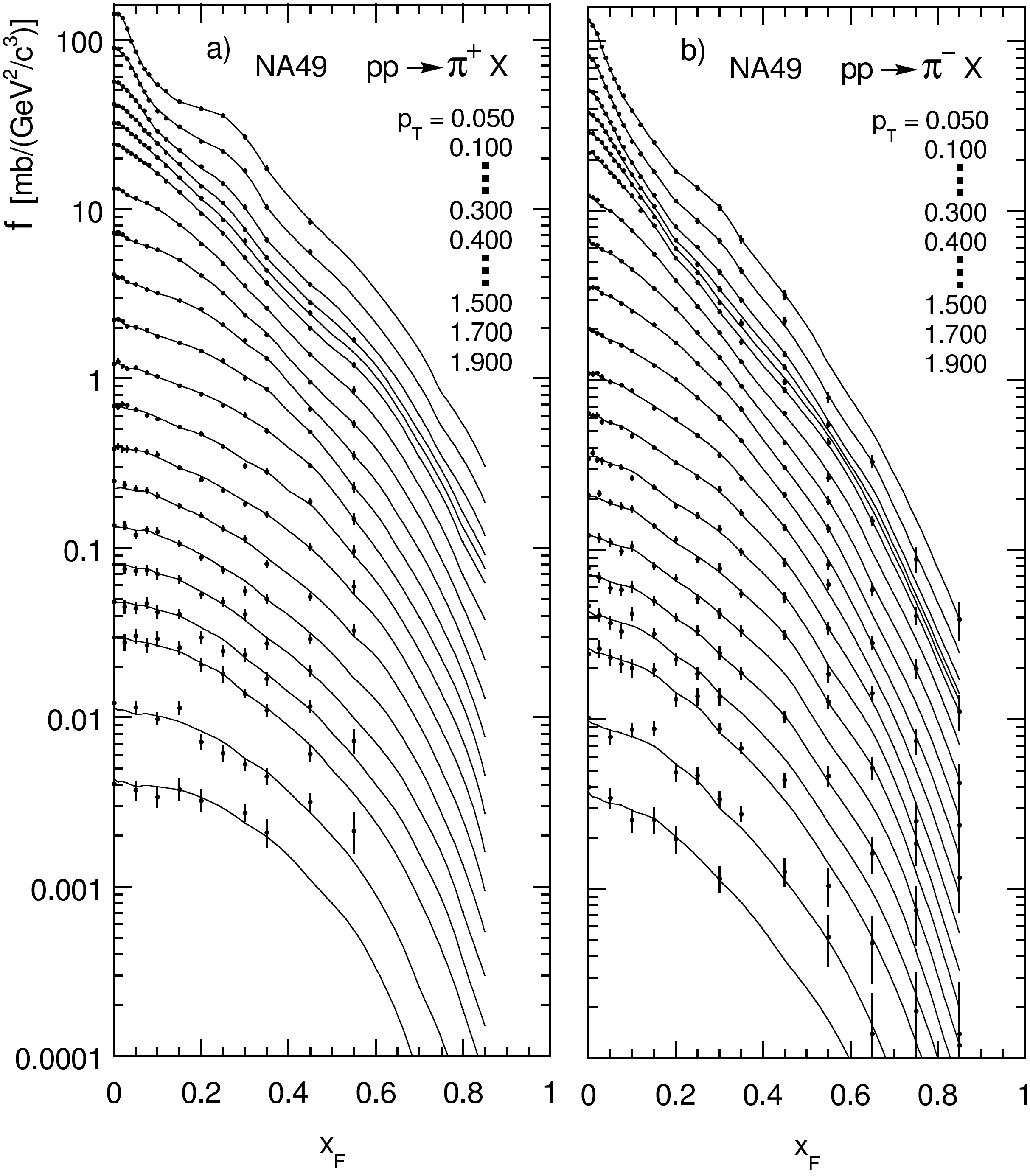

Figure 30: Invariant cross section as a function of x_F at fixed p_T for a) π^+ and b) π^- produced in p+p collisions at 158 GeV/c. The steps in p_T are 50 MeV/c up to $p_T = 0.300$ GeV/c, then 100 MeV/c up to 1.5 GeV/c and finally 200 MeV/c. Data and lines for $p_T = 0.05, 0.1, 0.15$ GeV/c are multiplied by 2.25, 1.5, 1.1, respectively, to allow for a better separation.

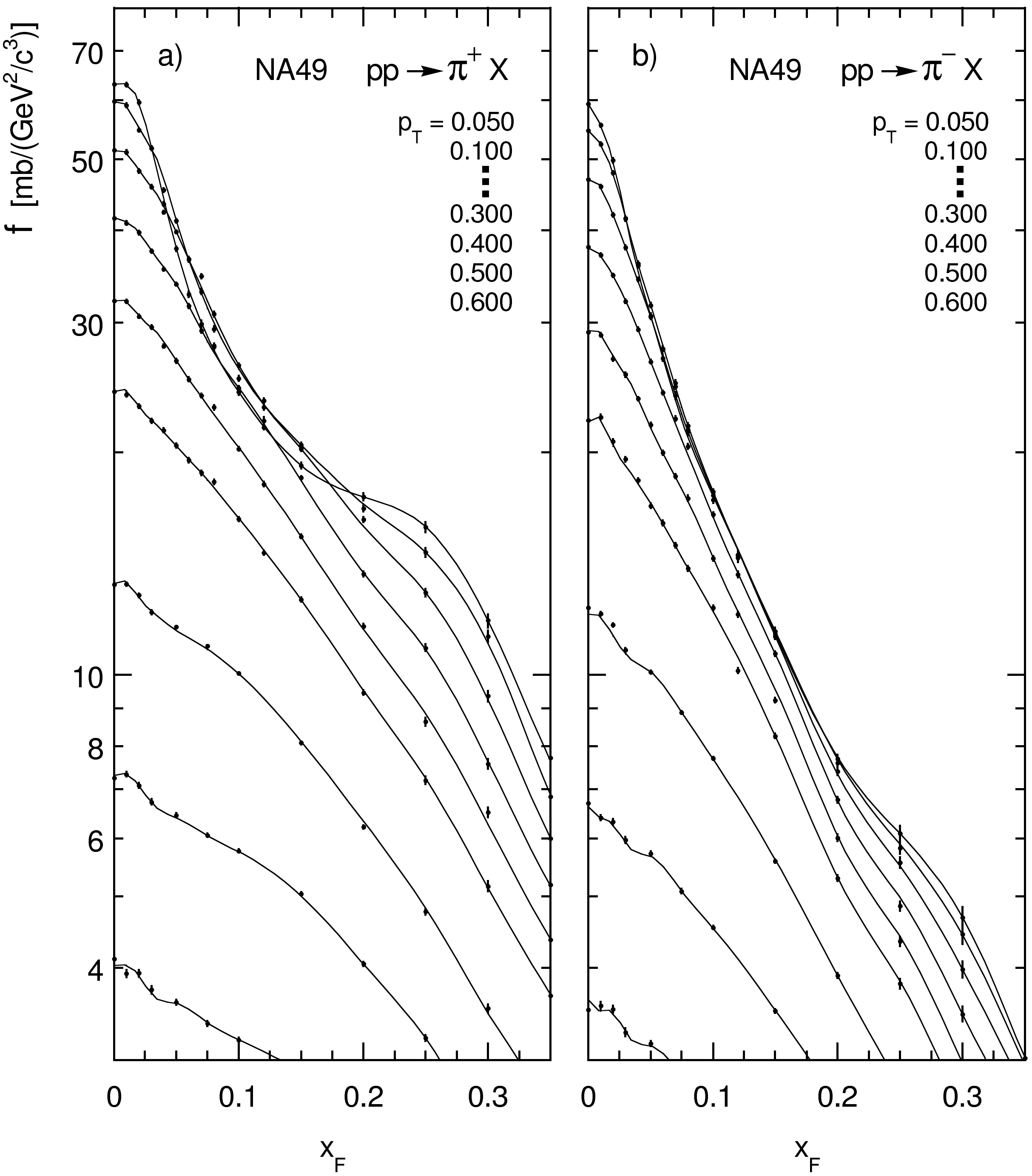

Figure 31: Invariant cross section as a function of x_F at fixed p_T for a) π^+ and b) π^- produced in p+p collisions at 158 GeV/c. The low x_F and low p_T region is magnified in order to demonstrate the complicated behaviour of the invariant cross section in this region. Note that data and lines are not multiplied by factors in contrast to Fig. 30.

7.4 π^+/π^- Ratios

The distinct differences in the distributions of π^+ and π^- over phase space result in a complex pattern of the corresponding π^+/π^- ratios. This is demonstrated in Figs. 32 and 33 where the p_T dependence for fixed x_F and the x_F dependence for fixed p_T are shown in separate panels.

The well-known increase of the ratios with x_F up to values of about 3 at $x_F \simeq 0.5$ is evident (see also Fig. 46); but for the first time with these data, well defined structures at low (< 0.3 GeV/c), intermediate ($0.5 - 0.7$ GeV/c) and high p_T (> 1.5 GeV/c) as well as x_F around 0.25 become visible.

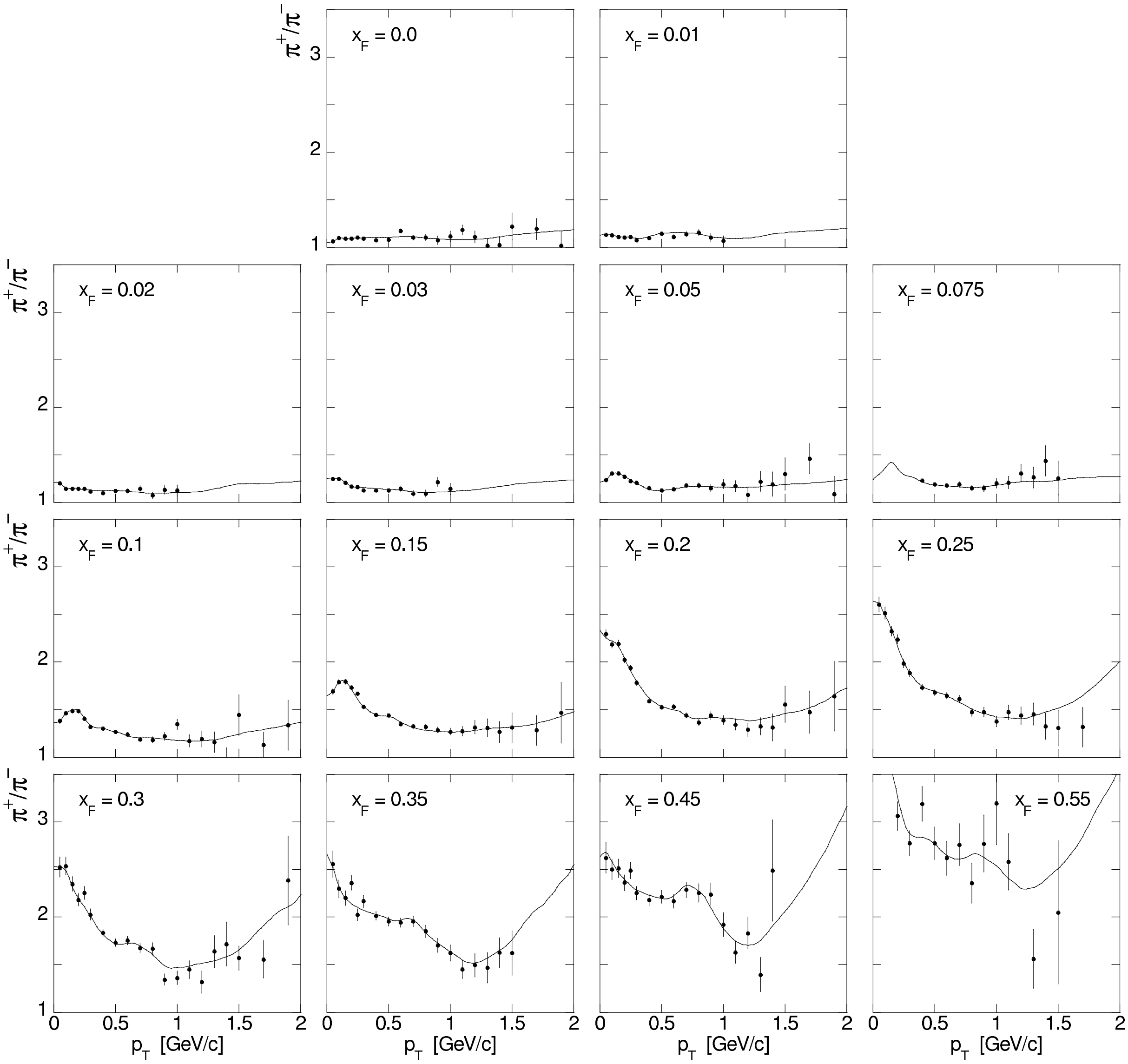

Figure 32: Ratio of invariant cross section for π^+ and π^- as a function of p_T at fixed x_F.

7.5 Rapidity and Transverse Mass Distributions

It is customary to view double differential invariant cross sections also on the phase space subsurface of y and p_T although these two variables are not orthogonal in momentum space.

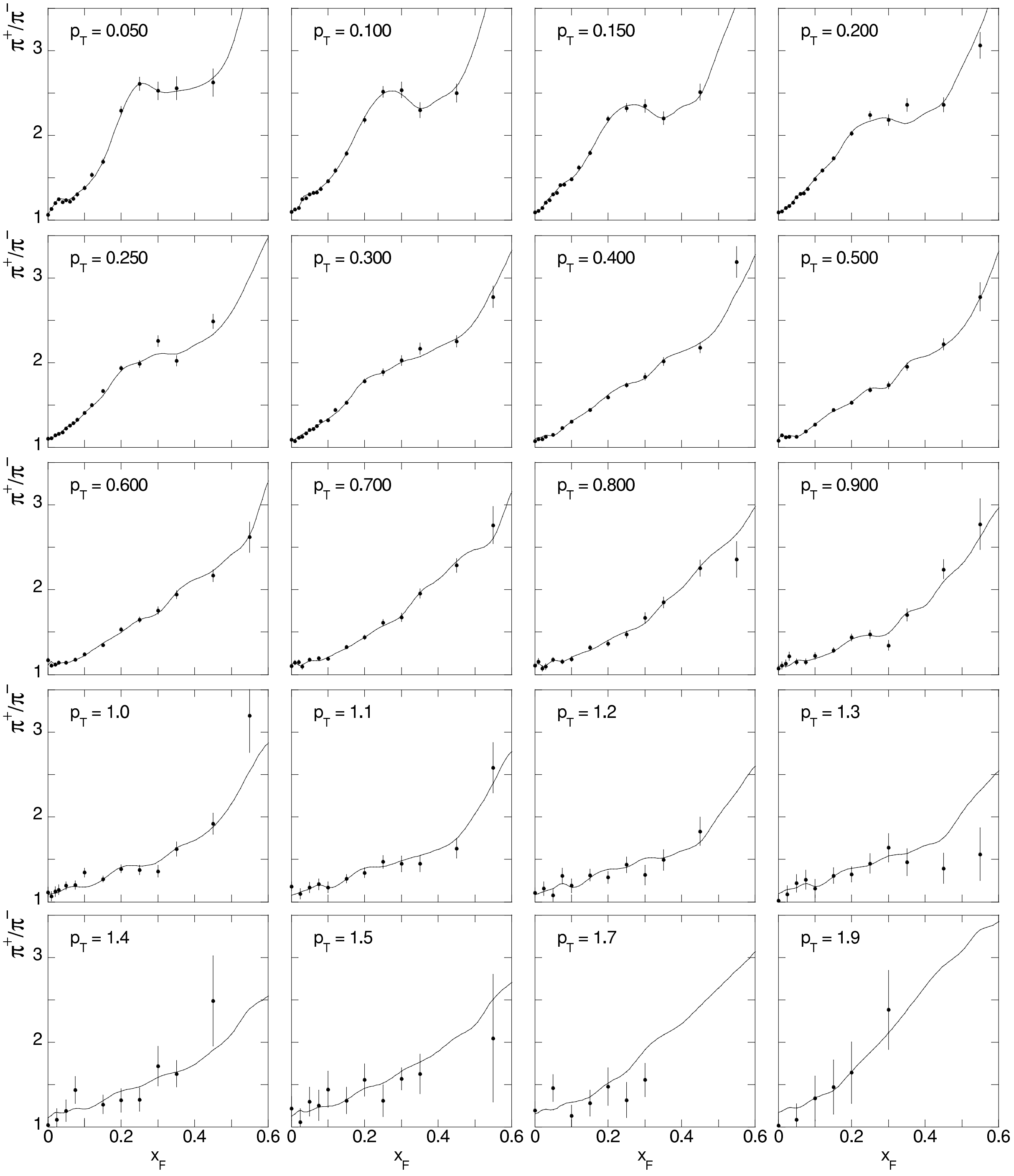

Figure 33: Ratio of invariant cross section for π^+ and π^- as a function of x_F at fixed p_T.

The data of Tables 4 and 5 are readily transformed into y distributions at fixed values of p_T and shown in Fig. 34.

At fixed p_T the y distribution corresponds essentially to a distorted longitudinal momentum distribution. The structures observed as a function of x_F will therefore also appear at the corresponding y values which is indeed the case. This is visible in more detail in the magnified y distributions for $p_T < 0.5$ GeV/c shown in Fig. 35. With increasing p_T these structures happen to be less pronounced as compared to the x_F distributions (Fig. 31) due to the different projection of phase space.

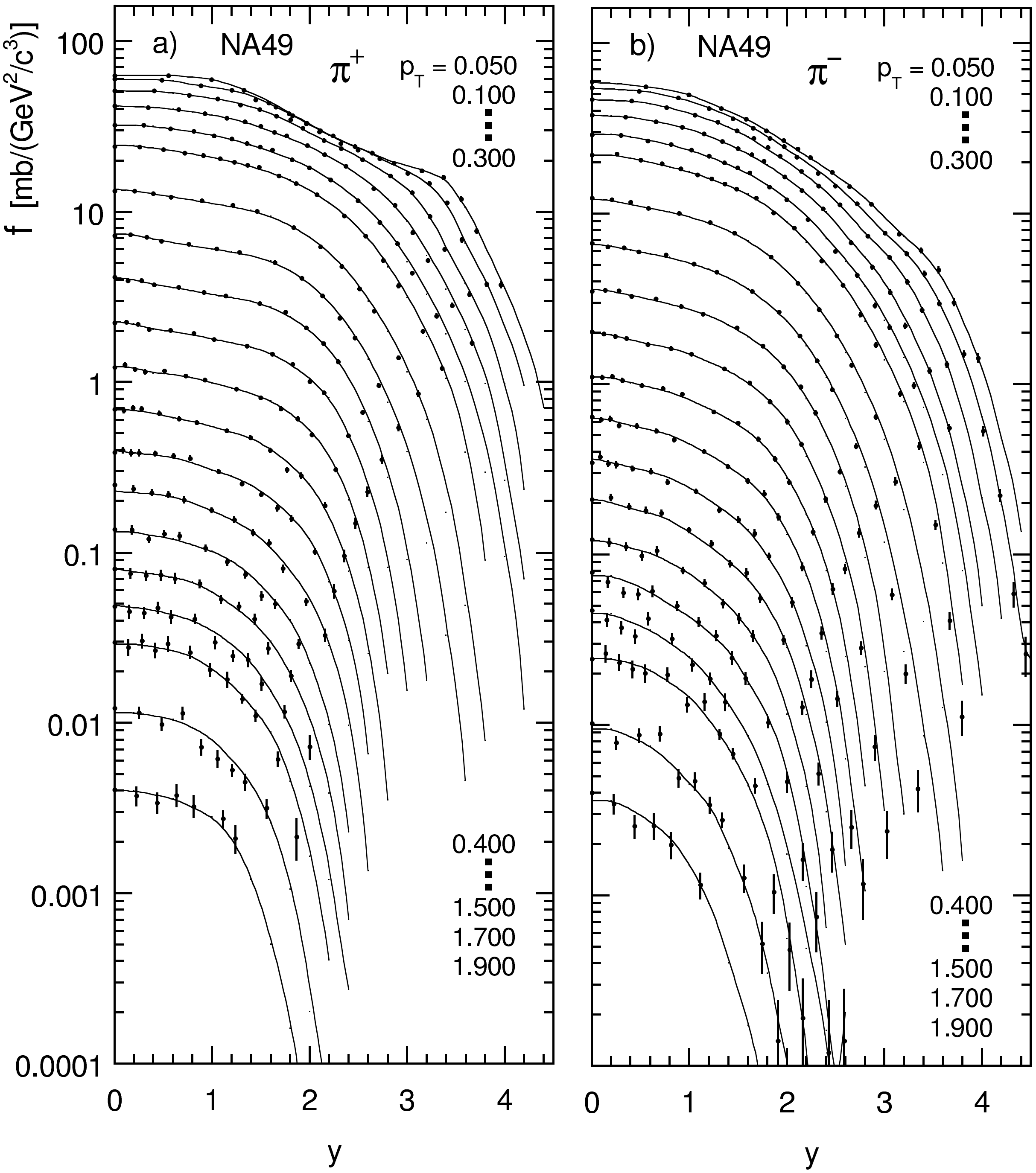

Figure 34: Invariant cross section as a function of y at fixed p_T for a) π^+ and b) π^- produced in p+p collisions at 158 GeV/c. The steps in p_T are 50 MeV/c up to $p_T = 0.300$ GeV/c, then 100 MeV/c up to 1.5 GeV/c and finally 200 MeV/c.

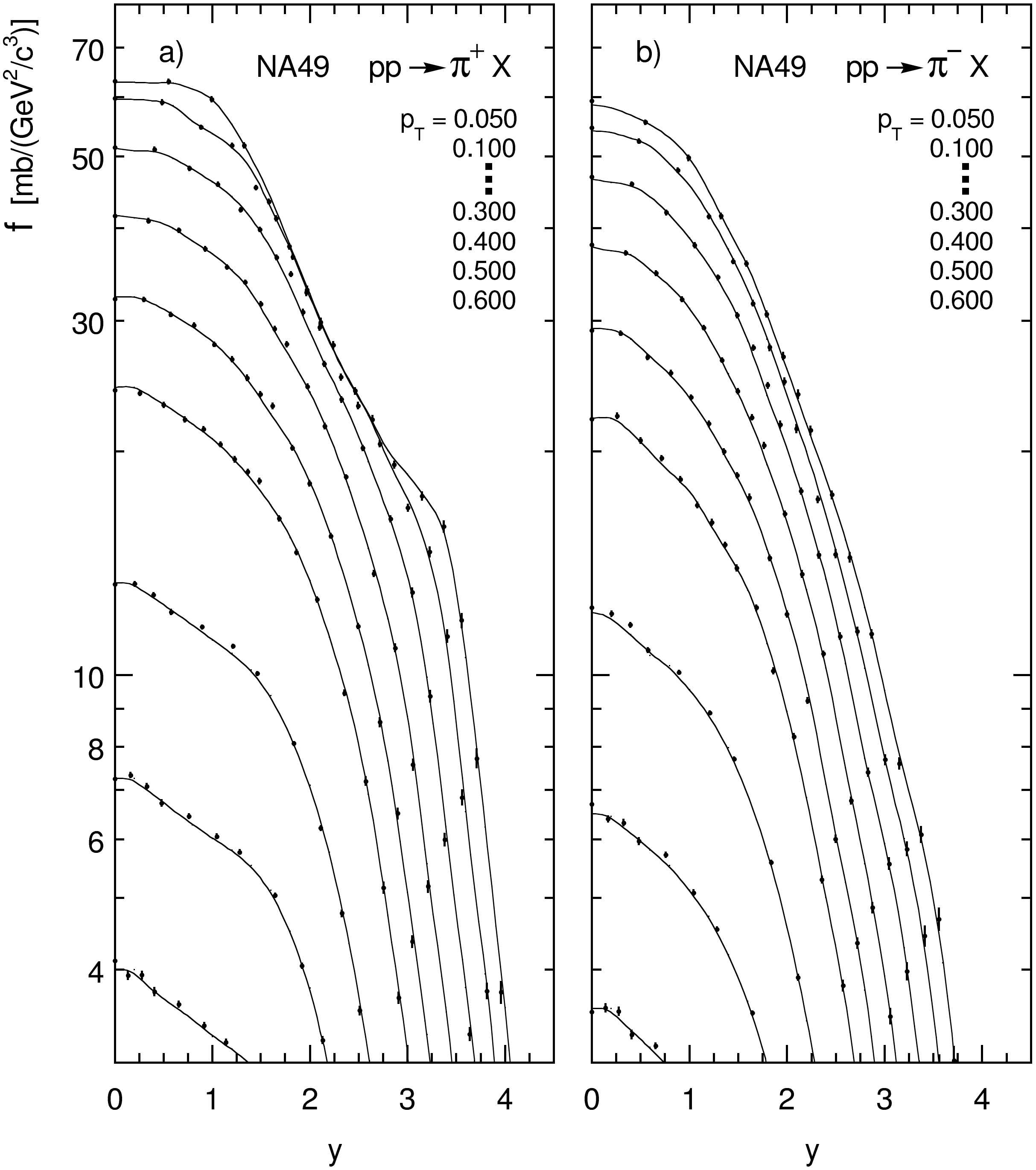

Figure 35: Invariant cross section as a function of y at fixed p_T for a) π^+ and b) π^- produced in p+p collisions at 158 GeV/c. The low p_T region is magnified in order to demonstrate that the complicated behaviour of the invariant cross section in x_F is also apparent in y.

Another frequently used variable is the transverse mass $m_T = \sqrt{m_\pi^2 + p_T^2}$. In fact, the shape of the m_T distributions is often claimed to be close to exponential with an inverse slope parameter T as predicted for particle emission from a thermal source. In Fig. 36 the invariant cross section is presented as a function of $m_T - m_\pi$ for π^+ and π^- produced at $y = 0.0$.

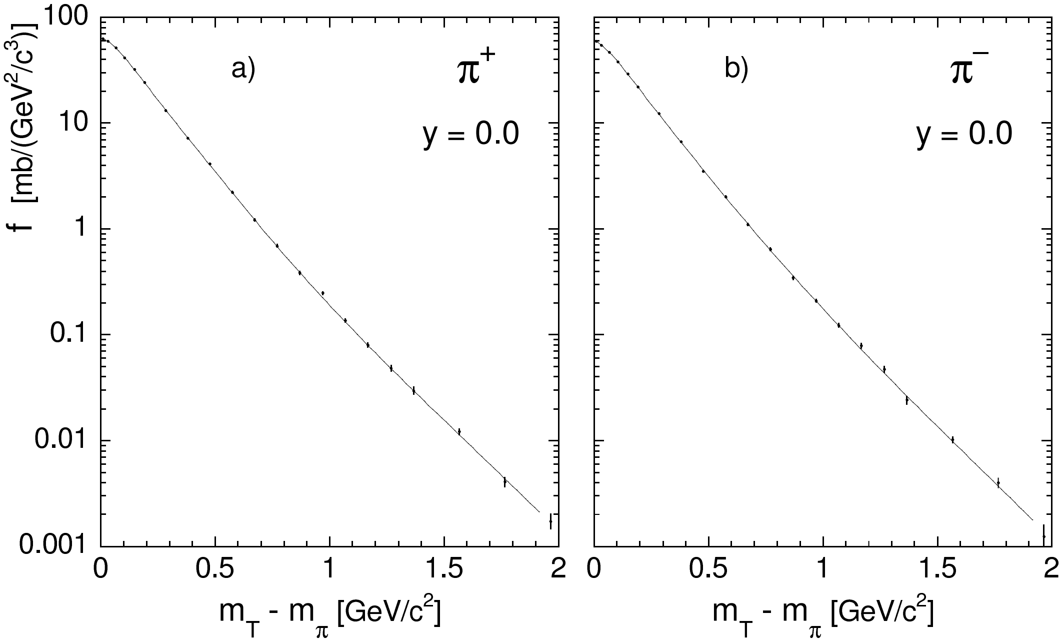

Figure 36: Invariant cross section as a function of $m_T - m_\pi$ for a) π^+ and b) π^- produced at $y = 0.0$

The quality of the data allows to demonstrate that the shape of the m_T distributions cannot be described by a single exponential and makes the determination of the local inverse slope $T(m_T - m_\pi)$ as a function of transverse mass possible. As shown in Fig. 37 there is, both for

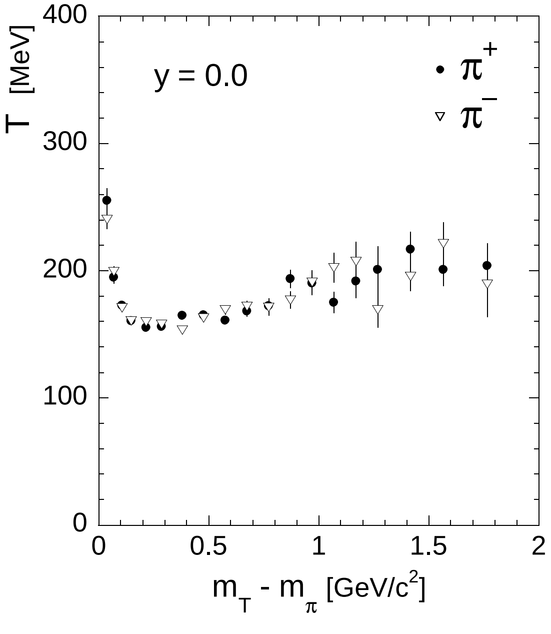

Figure 37: Local slope of the m_T distribution as a function of $m_T - m_\pi$ for π^+ and π^-.

π^+ and for π^-, a smooth and continuous variation of T with $m_T - m_\pi$ around a minimum of $T = 0.155$ GeV at $m_T - m_\pi \simeq 0.250$ GeV/c^2 extending to values in excess of $T = 0.200$ GeV both at low and and high $m_T - m_\pi$.

8 Comparison to other Data

8.1 Comparison at SPS/Fermilab Energies

As shown in Section 2 above, there are only two preceding experiments which measured double differential cross sections for identified pions in overlapping ranges of $\sqrt{s}$ allowing for direct comparison. The data of Brenner et al. [8] from the Fermilab SAS spectrometer offer 107 data points at beam momenta of 100 and 175 GeV/c, the data of Johnson et al. [6] comprise 241 data points at the three beam momenta 100, 200 and 400 GeV/c. The corresponding comparisons are presented in Figs. 38, 39 and 40 where the interpolated NA49 data are used as reference and are shown as full lines at those values of x_F and p_T where direct comparison is feasible. As the Johnson data have not been obtained at fixed x_F but with respect to the radial scaling variable $x_R = E^{cms}/E^{cms}_{max}$, their positions have to be retransformed into x_F values depending both on p_T and $\sqrt{s}$. Therefore in this case only x_F distributions at fixed p_T are given.

Inspection of Figs. 38 and 39 reveals that the SAS data show a good overall agreement with NA49, whereas very sizeable systematic deviations with a complicated p_T and x_F dependence appear in the Johnson data (Fig. 40). This situation is quantified in the statistical analysis presented in Fig. 41.

In Fig. 41a and d the distribution of the point-by-point statistical error of the cross section difference is given. These errors have most probable values around 6 and 4%, respectively, which are governed by the statistics of the spectrometer experiments. The long upwards tails

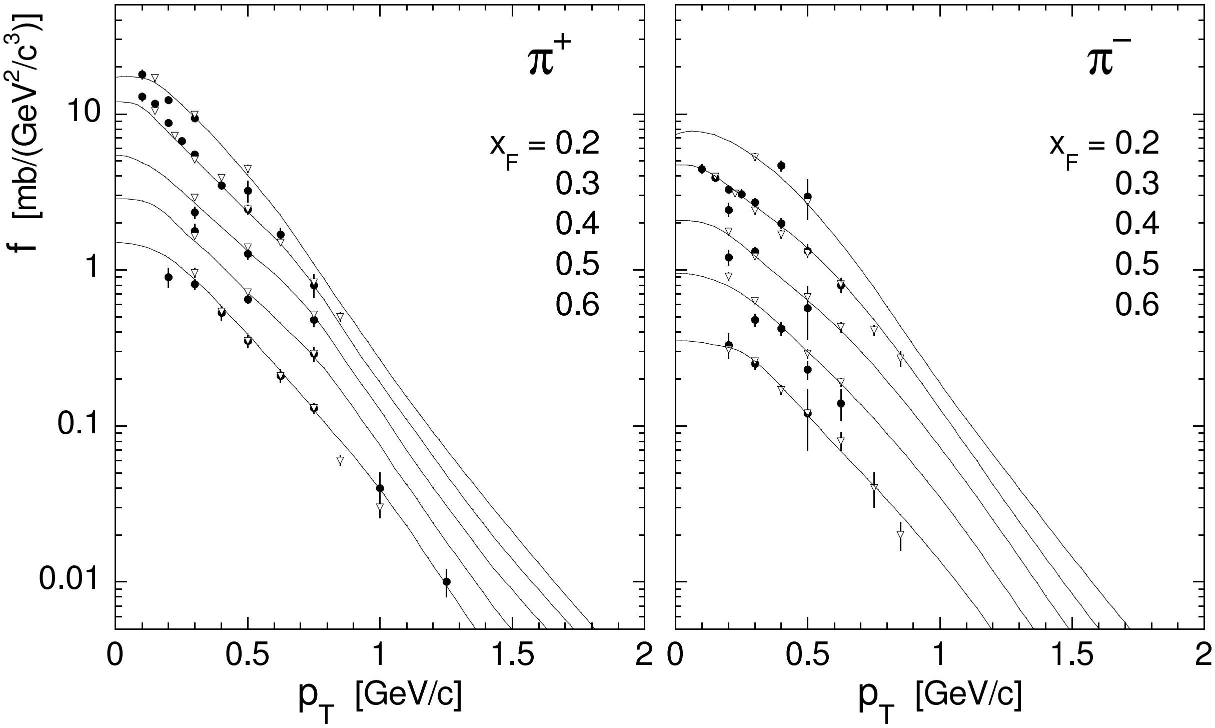

Figure 38: Comparison of invariant cross section as a function of p_T at fixed x_F from NA49 (lines) with measurements from [8] at 100 (full circles) and 175 GeV/c (open triangles).

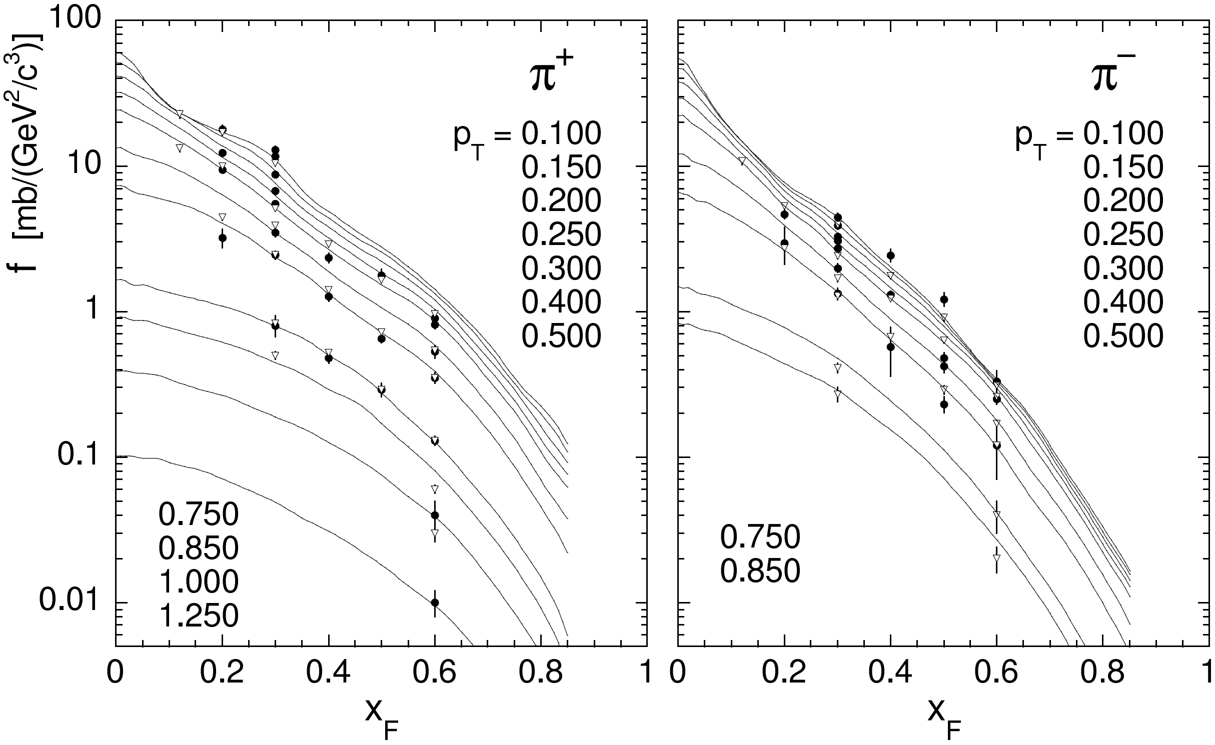

Figure 39: Comparison of invariant cross section as a function of x_F at fixed p_T from NA49 (lines) with measurements from [8] at 100 (full circles) and 175 GeV/c (open triangles).

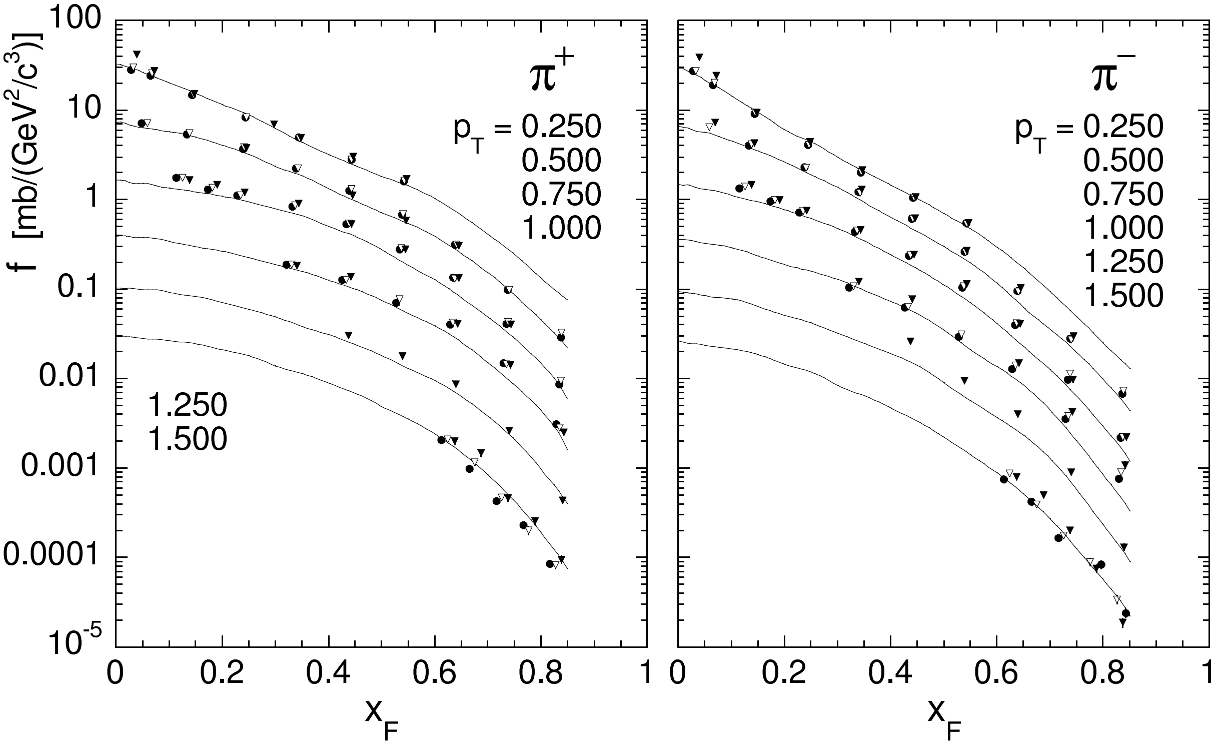

Figure 40: Comparison of invariant cross section as a function of x_F at fixed p_T measured by NA49 (lines) with measurements from [6] at 100 (full circles), 200 (open triangles), and 400 GeV/c (full triangles).

are reflecting the decrease of cross section at high x_F and/or p_T. Here the NA49 errors become comparable or exceed the ones of the comparison data. Fig. 41b and e shows the point-by-point cross section difference in percent with respect to the NA49 data. If this difference is completely defined by statistical fluctuations, its ratio to the statistical error, shown in Fig. 41c and f, should obey a Gaussian distribution with variance unity. This is indeed true for the SAS data as demonstrated by the Gaussian fits superimposed to the histogrammes. In fact the mean difference over the 107 points is less than 1% with an error of about 1%. In view of the overall systematic errors of 2% and 7% given for NA49 and SAS respectively, this agreement has to be regarded as fortuitous. More importantly however, the agreement of the data within purely statistical fluctuations helps to exclude systematic effects between the two measurements as well as s-dependences beyond the level of about 5%.

The experimental situation is less favourable with respect to the data of Johnson et al. Although their statistical errors are smaller than the ones of SAS (see Fig. 41d) already the cross section differences, Fig. 41e, show a very broad and off-centered distribution. The normalized differences, Fig. 41f, are off by nearly 3 standard deviations whilst the variance is around 4 units. Even taking account of a mean shift of the data by 16%, which might be in agreement with the normalization uncertainties mentioned in their publication, this indicates major systematic effects which are also clearly visible in the direct data comparison of Fig. 40.

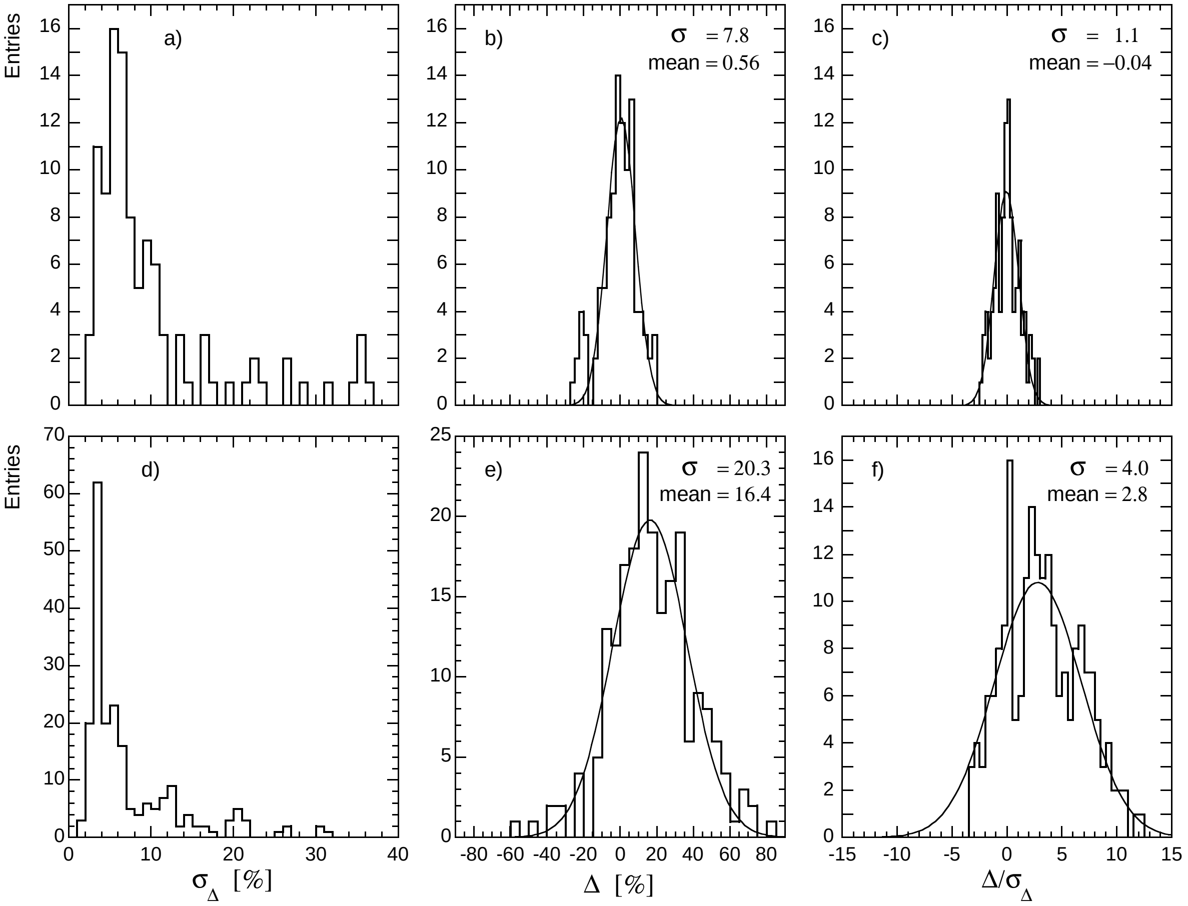

Figure 41: Statistical analysis of the difference of the measurements of [8] (upper three pannels) and [6] (lower three pannels) with respect to NA49: a) and d) error of the difference of the measurements; b) and e) difference of the measurements; c) and f) difference divided by the error.

8.2 Comparison with Forward Production at ISR Energies and Extension of Data Interpolation for π^+

As the identification of π^+ suffers from the preponderant proton component for $x_F > 0.6$, it is of interest to try to make use of the large set of ISR data in the forward region in order to extend the NA49 results on π^+ to the same phase space coverage as the π^- data. The CHLM Collaboration, Albrow et al. [15, 16, 19, 23] has published sizeable sets of cross sections in the region $0.3 < x_F < 0.85$ and $0.3 < p_T < 1.2$ GeV/c. These data are more abundant for π^+ production where samples at $\sqrt{s} = 31$, 45 and 53 GeV [19] as well as independent measurements at $\sqrt{s} = 45$ GeV [23] are available. For π^- only measurements at $\sqrt{s} = 45$ GeV [23] and a set of data at one fixed angle [16] have been published.

The ISR data can be compared directly to the NA49 results in the region of overlapping measurements. For π^- this is presented in Fig. 42 showing various x_F distributions at fixed p_T. A detailed statistical analysis making use of a total of 111 data points is presented in Fig. 43. There is good agreement over the complete range of measurements with the exception of a series of points obtained at $\sqrt{s} = 23$ GeV [16] which are clearly above the NA49 data by about 25% (open triangles in Fig. 42).

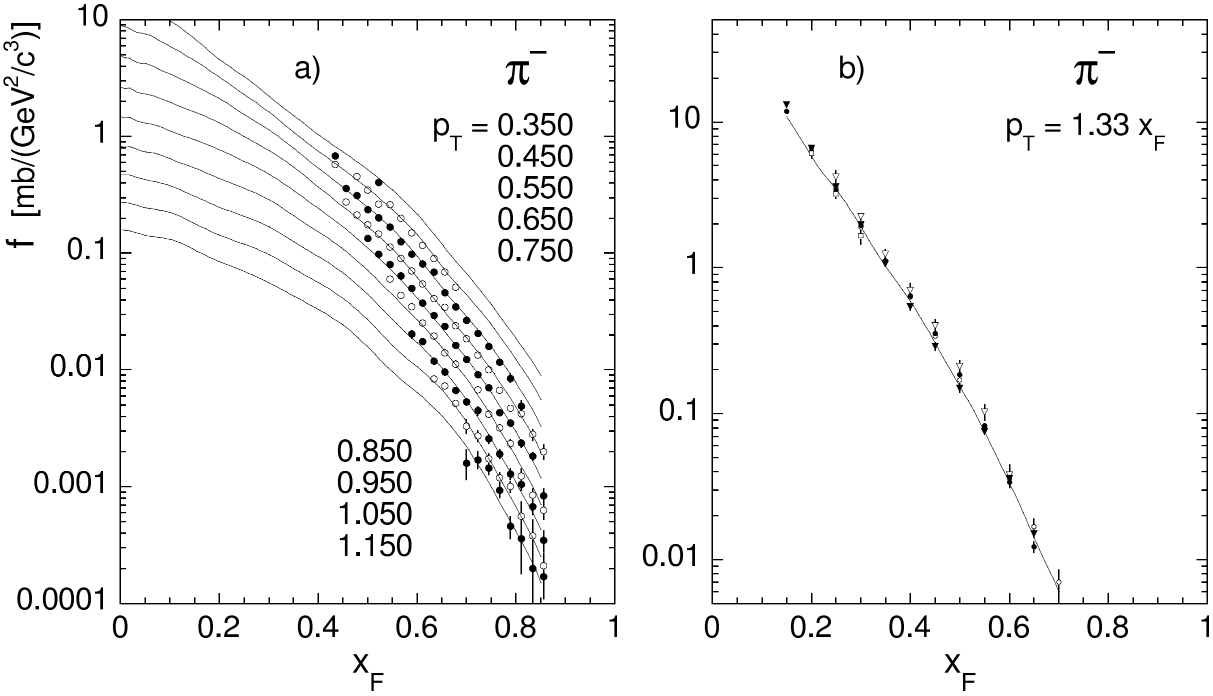

Figure 42: Comparison of invariant cross section as a function of x_F at fixed p_T measured by NA49 (lines) with measurements at a) $\sqrt{s} = 45$ GeV [23] and b) $\sqrt{s} = 23, 31, 45, 53, 63$ GeV [16].

For π^+ the situation is more complicated and summarized in Fig. 44. The ISR data of [19] obtained at $\sqrt{s} = 31$, 45 and 53 GeV show good agreement (Fig. 44a) whereas the data of [23] from the same collaboration show sizeable upward shifts of about 20% in the x_F region where they overlap with the NA49 measurements (Fig. 44b). On the other hand this internal discrepancy vanishes for higher values of x_F, also seen in Fig. 44b. It has therefore been decided to use the combined data of [19] and [23] in the appropriate x_F ranges in order to extend the data parametrization of NA49 for π^+. The statistical analysis of the [19] data is presented in Fig. 45.

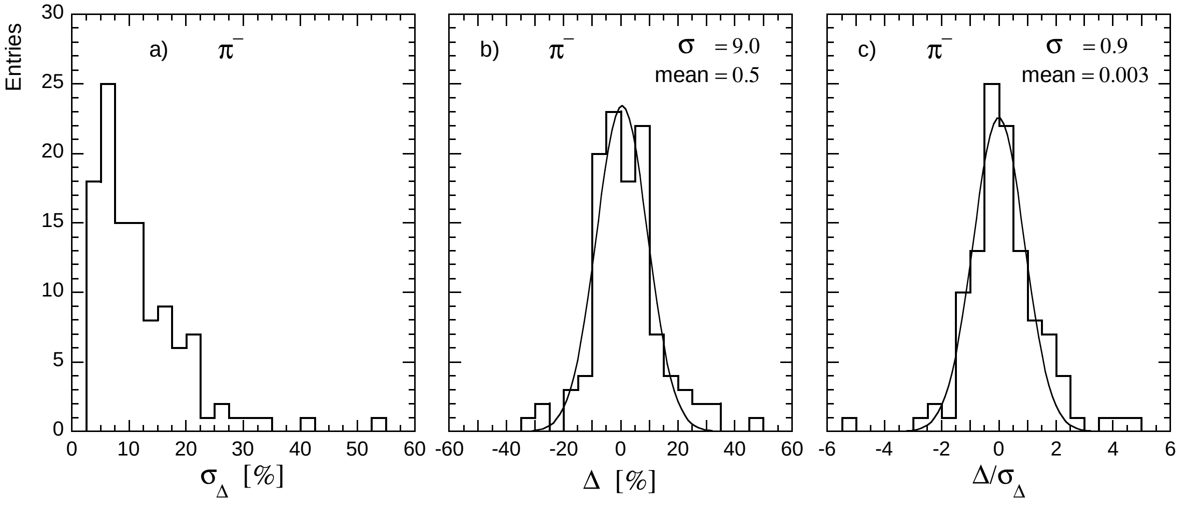

Figure 43: Statistical analysis of the difference of the measurements of [23] with respect to NA49: a) error of the difference of the measurements; b) difference of the measurements; c) difference divided by the error.

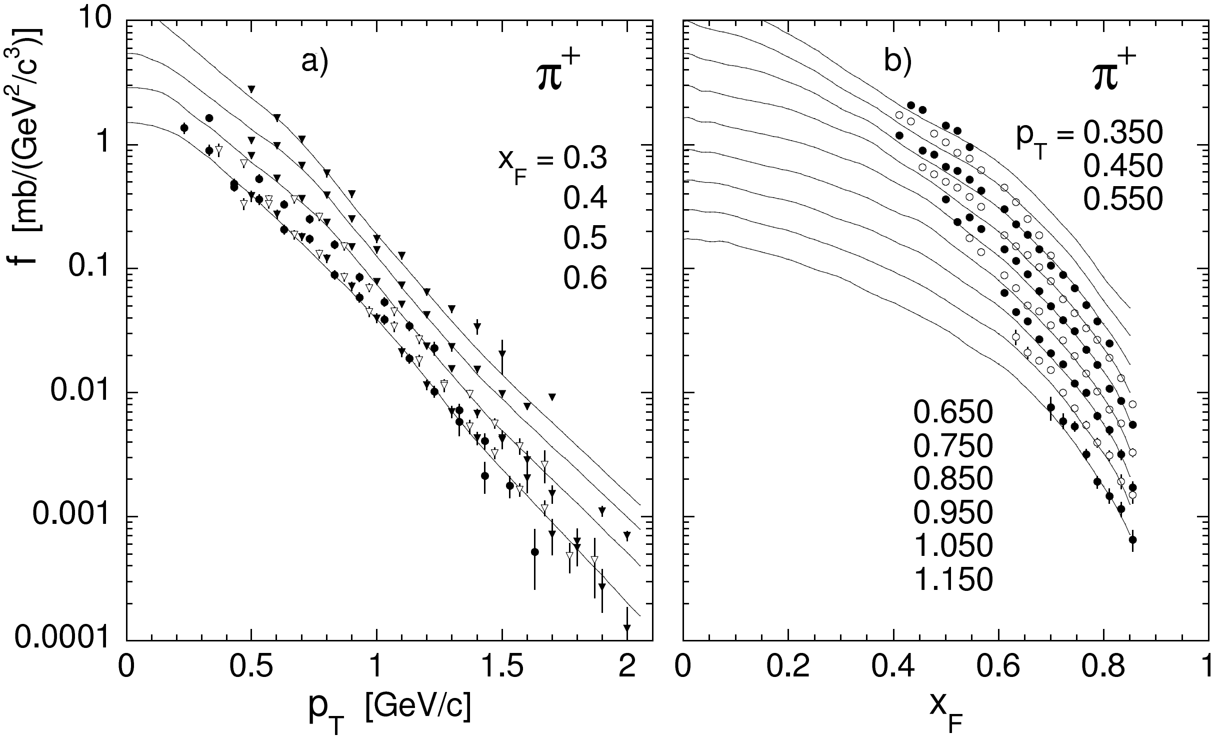

Figure 44: Comparison of invariant cross section as a function of a) p_T at fixed x_F published by [19] at $\sqrt{s} = 31, 45, 53$ GeV and b) x_F at fixed p_T published by [23] at $\sqrt{s} = 45$ GeV to NA49 measurements represented as lines.

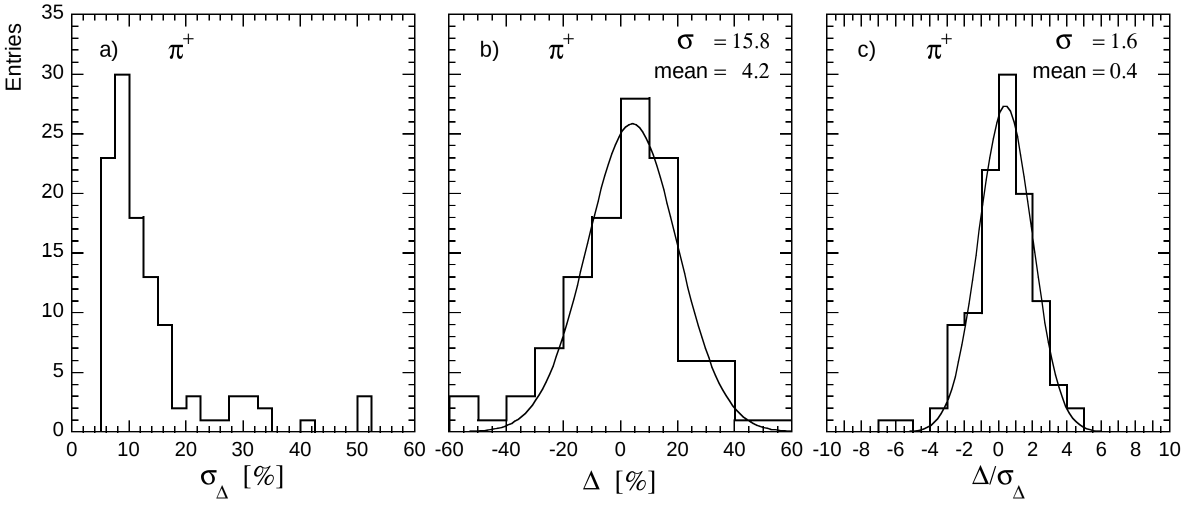

Figure 45: Statistical analysis of the difference of the measurements of [19] with respect to NA49: a) error of the difference of the measurements; b) difference of the measurements; c) difference divided by the error.

All in all, the data comparison over a range of $\sqrt{s}$ from 17 to 63 GeV demonstrates Feynman scaling to the level of a few percent both for π^+ and π^- in the range of $x_F > 0.4$. A more complete study of s-dependence also in comparison to lower energies and for more central ranges of x_F is outside the scope of this paper and will be addressed in a subsequent publication.

8.3 Comparison of π^+/π^- Ratios

A comparison of the π^+/π^- ratios as a function of x_F both in the Fermilab and ISR energy ranges is given in Fig. 46 for various p_T values. As expected from the comparison of the single particle cross sections of [8, 23], the general agreement is satisfactory with the exception of the ISR data at $\sqrt{s} = 45$ GeV in the lower range of x_F.

It is however interesting to note that also the data of Johnson et al. [6] show reasonable agreement as far as the ratios are concerned, which is clearly confirmed by the statistical analysis presented in Fig. 47. This indicates that the large systematic deviations found in the cross sections cancel out in the ratios thus allowing a further precise cross check of the NA49 data.

9 Integrated Data

In addition to the double differential invariant cross sections discussed above, integrated quantities such as invariant and non-invariant yields and particle ratios as a function of x_F or y, first and second moments of the p_T distributions and finally the total pion multiplicity are of interest. Such quantities are evaluated below and compared to other available data. Integrations are generally performed numerically applying Simpsons parabolic approximation to the interpolated data.

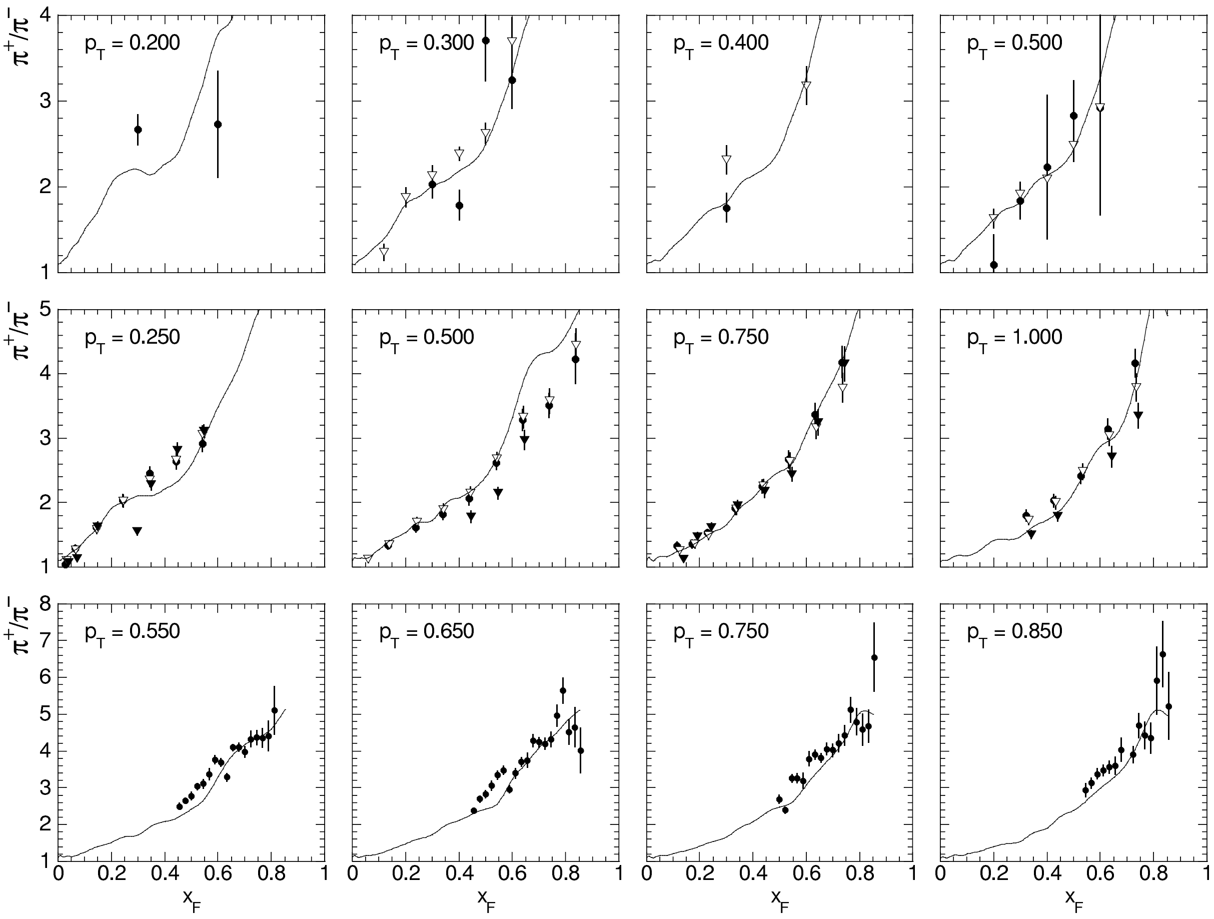

Figure 46: Comparison of π^+/π^- ratios as a function of x_F for various p_T values measured by [8] (upper four pannels), [6] (middle four pannels), and [23] (lower four pannels) to the NA49 results represented as lines.

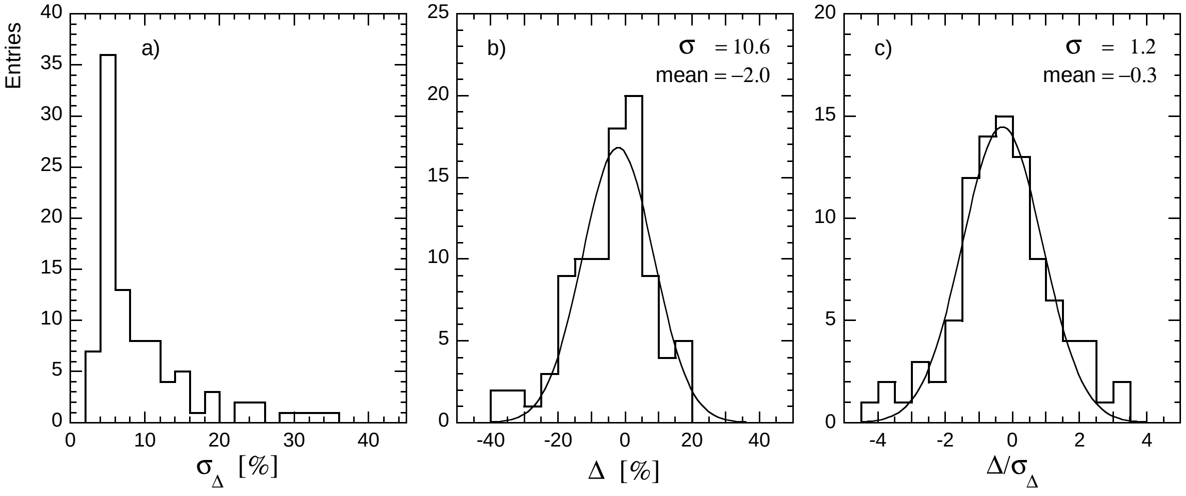

Figure 47: Statistical analysis of the difference of the π^+/π^- ratio of [6] with respect to NA49: a) error of the difference of the ratio measurements; b) difference of the ratio measurements; c) difference divided by the error.

9.1 p_T Integrated Distributions

The distributions of the non-invariant and invariant yields are defined as

$$dn/dx_F = \pi/\sigma_{inel} \cdot \sqrt{s}/2 \cdot \int f/E \cdot dp_T^2 \tag{9}$$

$$F = \int f \cdot dp_T^2$$

$$dn/dy = \pi/\sigma_{inel} \cdot \int f \cdot dp_T^2$$

with $f = E \cdot d^3\sigma/dp^3$, the invariant cross section. These quantities are summarized in Table 6 and shown as a function of x_F and y in Fig. 48.

The statistical errors are in general below the percent level with the exception of the π^- data at $x_F > 0.55$. The overall experimental uncertainties are therefore completely governed by the quoted systematic errors. This is in particular true for the extrapolated data for π^+ in the phase space region above $x_F = 0.55$.

Further integrated quantities such as π^+/π^- ratios, mean transverse momentum $\langle p_T \rangle$ and mean transverse momentum squared $\langle p_T^2 \rangle$ are presented in Fig. 49 again as a function of x_F. The distinct structures and in particular the differences between π^+ and π^- in the first and second moments of the p_T distributions are noteworthy and will be discussed in Section 10.

	π^+								π^-									π^+	π^-
x_F	F	Δ	dn/dx_F	Δ	$\langle p_T \rangle$	Δ	$\langle p_T^2 \rangle$	Δ	F	Δ	dn/dx_F	Δ	$\langle p_T \rangle$	Δ	$\langle p_T^2 \rangle$	Δ	y	dn/dy	dn/dy
0.0	7.505	0.13	20.959	0.14	0.2590	0.06	0.1015	0.13	6.832	0.13	19.136	0.13	0.2579	0.06	0.1009	0.13	0.0	0.7418	0.6713
0.01	7.500	0.12	19.640	0.13	0.2664	0.06	0.1062	0.13	6.704	0.12	17.586	0.13	0.2659	0.06	0.1055	0.13	0.2	0.7327	0.6567
0.02	7.171	0.12	16.348	0.12	0.2811	0.06	0.1165	0.12	6.323	0.12	14.334	0.13	0.2838	0.06	0.1183	0.13	0.4	0.7113	0.6281
0.03	6.819	0.12	13.344	0.12	0.2962	0.06	0.1274	0.12	5.865	0.12	11.377	0.13	0.3018	0.06	0.1312	0.13	0.6	0.6894	0.6022
0.05	6.216	0.12	9.134	0.12	0.3276	0.06	0.1520	0.12	5.180	0.12	7.550	0.13	0.3357	0.06	0.1579	0.13	0.8	0.6618	0.5760
0.075	5.519	0.12	6.084	0.12	0.3571	0.06	0.1776	0.14	4.391	0.13	4.807	0.14	0.3683	0.06	0.1868	0.15	1.0	0.6334	0.5425
0.1	4.963	0.12	4.353	0.12	0.3763	0.07	0.1955	0.14	3.734	0.14	3.254	0.14	0.3912	0.07	0.2093	0.18	1.2	0.6015	0.4973
0.15	4.050	0.11	2.502	0.12	0.4010	0.07	0.2214	0.15	2.707	0.14	1.663	0.14	0.4240	0.07	0.2435	0.14	1.4	0.5614	0.4426
0.2	3.263	0.14	1.549	0.14	0.4170	0.08	0.2408	0.15	1.925	0.17	0.9091	0.17	0.4509	0.09	0.2728	0.17	1.6	0.5102	0.3841
0.25	2.619	0.20	1.007	0.20	0.4246	0.09	0.2520	0.19	1.437	0.24	0.5505	0.24	0.4625	0.12	0.2890	0.23	1.8	0.4509	0.3191
0.3	1.959	0.26	0.6325	0.26	0.4395	0.13	0.2697	0.24	1.042	0.35	0.3355	0.35	0.4750	0.17	0.3046	0.31	2.0	0.3863	0.2534
0.35	1.462	0.27	0.4061	0.27	0.4634	0.13	0.2932	0.23	0.7280	0.37	0.2020	0.37	0.4857	0.18	0.3184	0.31	2.2	0.3186	0.1964
0.45	0.8027	0.29	0.1745	0.29	0.4768	0.14	0.3112	0.24	0.3552	0.45	0.0772	0.45	0.4940	0.19	0.3312	0.33	2.4	0.2525	0.1462
0.55	0.4439	0.65	0.0792	0.65	0.4631	0.25	0.2964	0.50	0.1544	0.78	0.0275	0.78	0.4896	0.40	0.3232	0.74	2.6	0.1924	0.1034
0.65	0.2046	1.00	0.0309	1.05	0.4587	0.60	0.2915	1.15	0.0542	1.46	0.00820	1.46	0.4865	0.82	0.3269	1.58	2.8	0.1420	0.0703
0.75	0.0727	2.05	0.00955	2.10	0.4501	1.00	0.2804	1.75	0.0157	2.96	0.00205	2.96	0.4741	1.64	0.3068	3.05	3.0	0.1018	0.0463
0.85	0.0200	3.25	0.00232	3.35	0.4040	2.60	0.2314	3.50	0.00355	5.93	0.00041	5.93	0.4345	3.44	0.2602	6.25	3.2	0.0698	0.0298
																	3.4	0.0449	0.0179
																	3.6	0.0255	0.00966
																	3.8	0.0133	0.00446
																	4.0	0.00621	0.00179
																	4.2	0.00247	0.000566
																	4.4	0.000755	0.000141
																	4.6	0.000208	0.0000351
																	4.8	0.0000396	0.0000065

Table 6: p_T integrated invariant cross section F [mb·c], density distribution dn/dx_F, mean transverse momentum $\langle p_T \rangle$ [GeV/c], mean transverse momentum squared $\langle p_T^2 \rangle$ [(GeV/c)^2] as a function of x_F, as well as density distribution dn/dy as a function of y for π^+ and π^-. The statistical uncertainty Δ for each quantity is given in %.

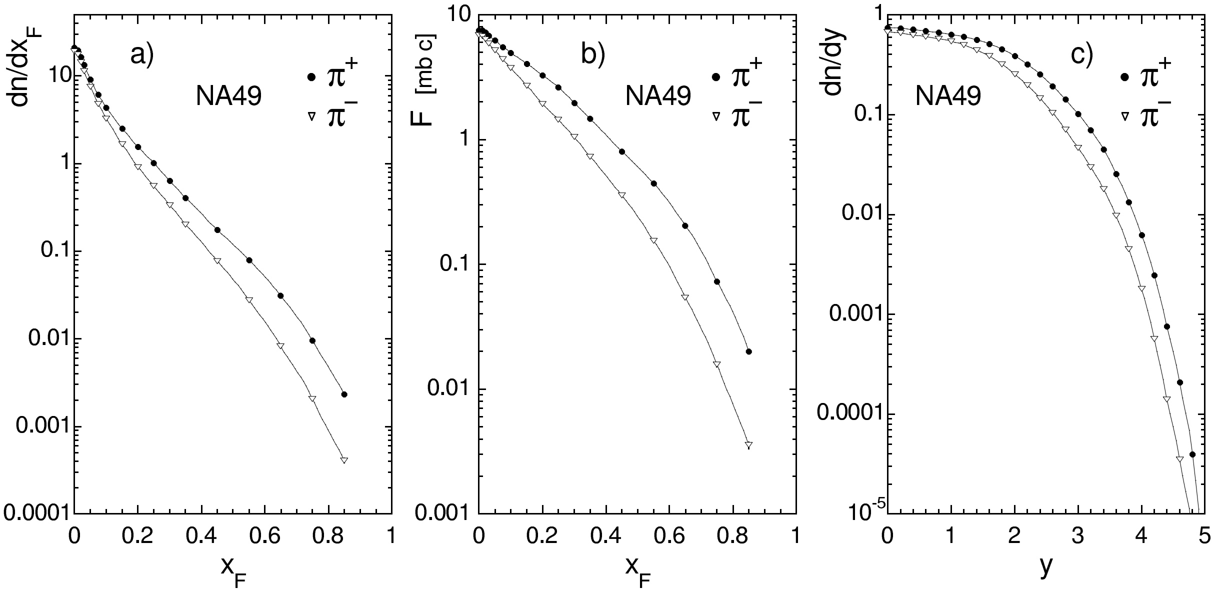

Figure 48: Integrated distributions of π^+ and π^- produced in p+p interactions at 158 GeV/c: a) density distribution dn/dx_F as a function of x_F; b) Integrated invariant cross section F as a function of x_F; c) density distribution dn/dy as a function of y.

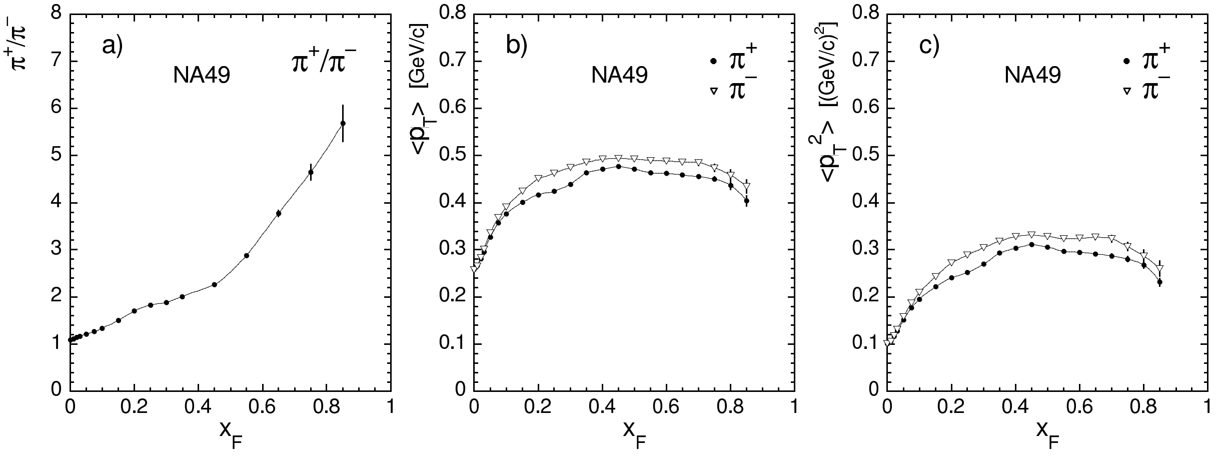

Figure 49: a) π^+/π^- ratio, b) mean p_T, and c) mean p_T^2 as a function of x_F for π^+ and π^- produced in p+p interactions at 158 GeV/c.

9.2 Data Comparison

Given the scarcity and generally incomplete phase space coverage of other experiments the extraction of integrated quantities is liable to suffer from sizeable systematic uncertainties. This becomes evident by comparing the p_T integrated pion yields from [8] to the NA49 data as shown in Fig. 50. Although the differential data are in good agreement with each other as shown in Section 8.1, the use of simple exponential or Gaussian parametrizations of the p_T distributions for extrapolation into the unmeasured regions of p_T [8] result in systematic deviations of the integrated values which reach many standard deviations with respect to the given errors.

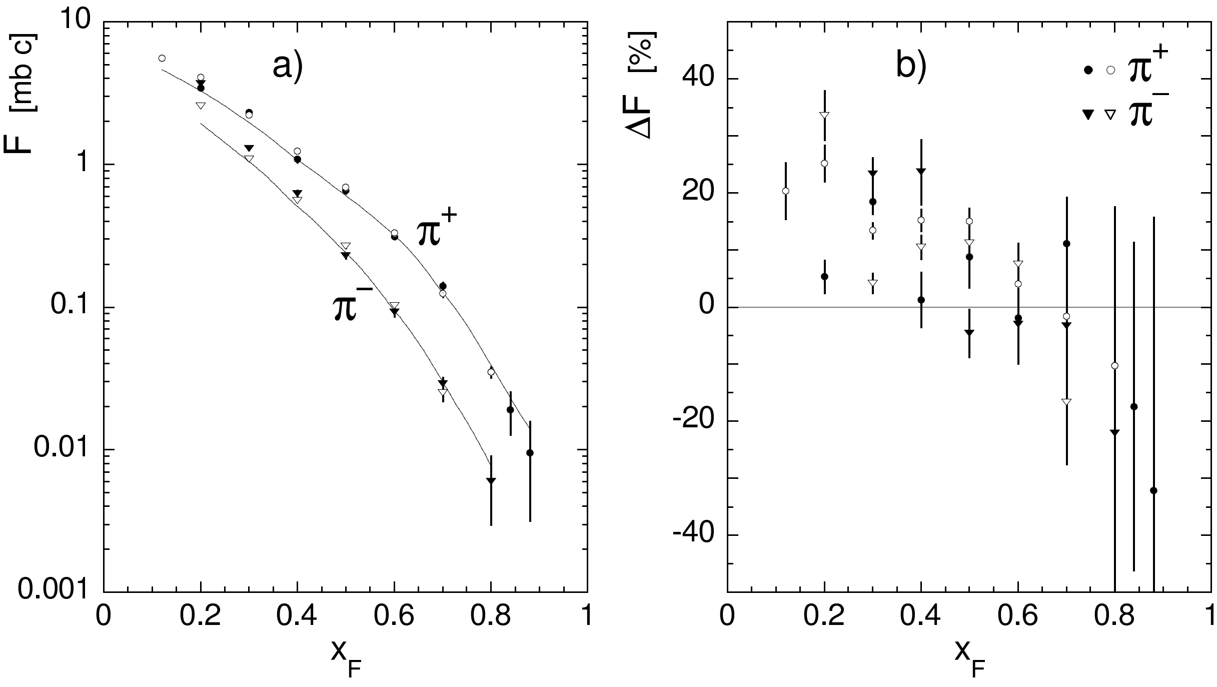

Figure 50: a) Comparison of p_T integrated invariant cross section F as a function of x_F for π^+ and π^- measured by [8] to NA49 results (represented as lines); b) Deviation of the measurements of [8] from the NA49 results in percent.

The EHS experiment [10–12] which is directly comparable to NA49 in terms of phase space coverage and potential particle identification capability and which has accumulated a sizeable data sample of 470k events at a beam momentum of 400 GeV/c has only published p_T integrated distributions of the invariant and non-invariant cross sections. The results are compared to the NA49 data in Fig. 51. As shown by the percentage deviation of the invariant yields (Fig. 51b), a consistent upward shift of about 12% is evident up to $x_F \simeq 0.35$. This shift is not compatible with the precise fulfillment of x_F scaling exhibited by the ISR data for $x_F > 0.3$ in the same energy range as discussed in Section 8.2. This indicates a normalization problem of the EHS data. Above $x_F = 0.35$, the EHS results show large and evidently unphysical systematic effects especially for the π^+ yields.

It is interesting to also compare the non-invariant density distributions dn/dx_F, as presented in Fig. 52. The increase of the percentage deviations below $x_F \simeq 0.15$ is entirely due to the energy dependence of the functional relation between non-invariant and invariant yields, see equation (9), as shown by the superimposed line in Fig. 52b. This relation predicts for s-independent invariant cross sections a linear increase of particle density with $\sqrt{s}$ at $x_F = 0$. This is evidently borne out by the data. A more detailed discussion of s-dependences will be

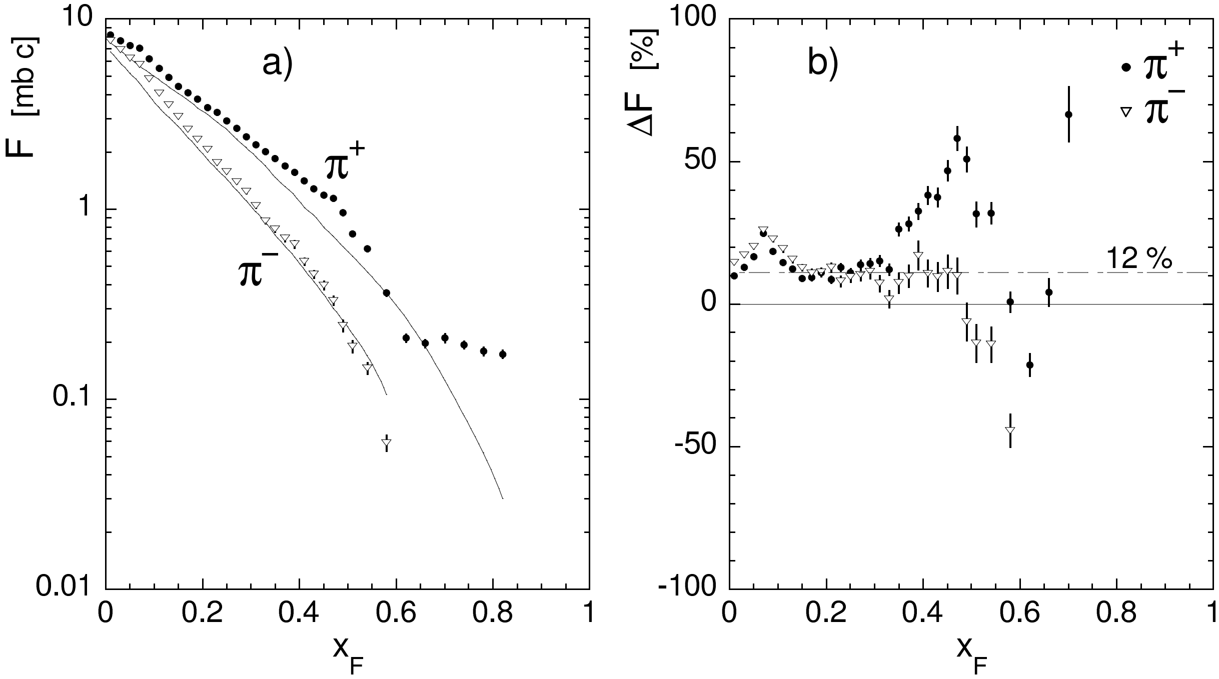

Figure 51: a) Comparison of p_T integrated invariant cross section F as a function of x_F for π^+ and π^- measured by [12] to NA49 results (represented as lines); b) Deviation of the measurements of [12] from the NA49 results in percent.

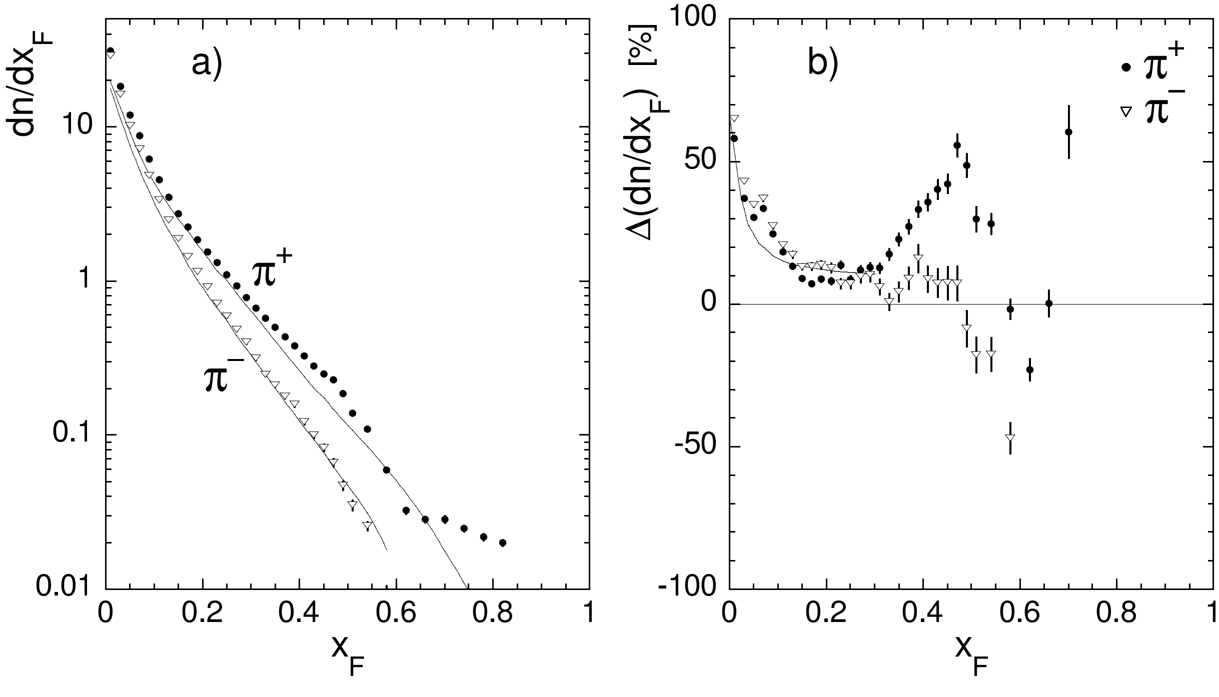

Figure 52: a) Comparison of density distribution dn/dx_F as a function of x_F for π^+ and π^- measured by [12] to NA49 results (represented as lines); b) Deviation of the measurements of [12] from the NA49 results in percent.

carried out in a separate publication.

A comparison of p_T integrated π^+/π^- ratios with NA49 is possible for the data of [8] and [12], whereas mean p_T and mean p_T^2 are only available from [10] and [12]. The summary of these comparisons is presented in Fig. 53.

The π^+/π^- ratios of [8] are in fair agreement with the NA49 results whereas the data of [12] deviate above $x_F \simeq 0.3$. The first and second moments of the p_T distributions show an upward trend also below this x_F value which complies with the expected s-dependence of these quantities.

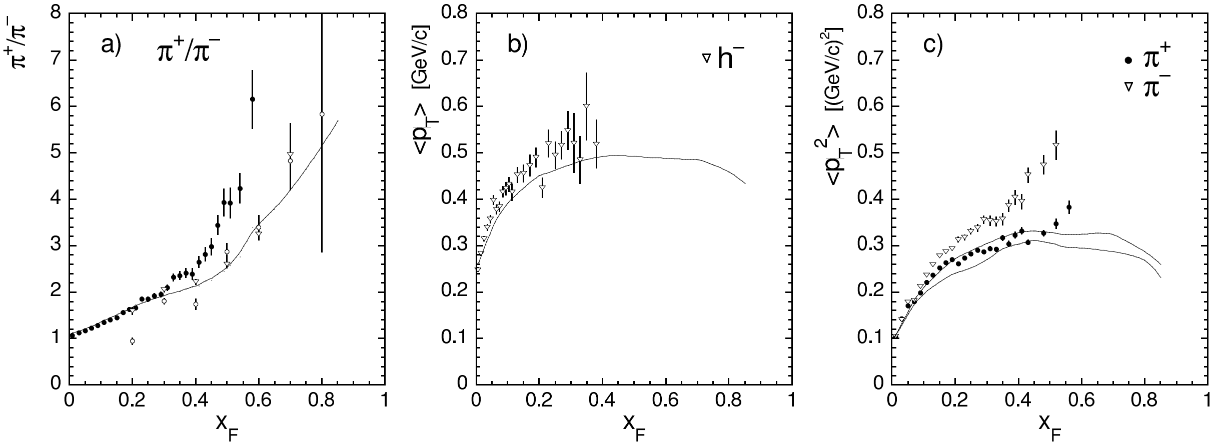

Figure 53: Comparison as a function of x_F of a) π^+/π^- ratio measured by [12] (full circles) and [8] (open symbols), b) mean p_T of h^- measured by [10], and c) mean p_T^2 for π^+ and π^- measured by [12] to NA49 results (represented as lines).

9.3 Total Pion Multiplicity

The integration of the dn/dx_F distribution presented in Table 6 yields the following total pion multiplicities:

$$\begin{aligned} \langle n_{\pi^+} \rangle &= 3.018 \\ \langle n_{\pi^-} \rangle &= 2.360 \\ \langle \pi^+/\pi^- \rangle &= 1.279 \end{aligned}$$

The statistical errors on these quantities are negligible compared to the overall normalization uncertainty of 1.5% given in Table 3.

9.4 Availability of the Presented Data

The NA49 data are available in numerical form on the Web Site [33] as far as the tabulated values are concerned. In addition and in order to give access to the complete data interpolation developed in the context of this publication, two large sets of π^+ and π^- momentum vectors ($5 \cdot 10^7$ each) can also be found on this site. These files are obtained by a Monte Carlo technique with importance sampling without weighting. By normalizing with the respective total pion multiplicities and the total inelastic cross section given above, distributions of cross sections in arbitrary coordinate representations and with arbitrary binning may readily be obtained. This might be found useful for comparison with production models using Monte Carlo methods with finite bin sizes especially in view of the importance of binning effects demonstrated in Section 5.7 above.

10 Discussion

The purpose of this paper is the establishment of a complete and internally consistent set of inclusive pion cross sections at SPS energy. As such, the data may serve as a basis of comparison with other hadronic interactions, in particular with collisions involving nuclei in p+A and A+A reactions. There is however, another important aspect of this work which is more directly related to the status of the theoretical understanding of soft hadronic collisions. This status might be described as deeply unsatisfactory due to the lack of reliability and predictive power of present attempts in the field of non-perturbative QCD. In the presence of sufficiently consistent and precise experimental information, both the multitude of ad-hoc microscopic multiparameter models and the attempts at a statistical approach to hadronic interactions fail to describe the detailed structure of the data even on the most primitive level of single particle inclusive cross sections. It is outside the scope of this publication to proceed with a detailed discussion of these problems which has to be left to subsequent papers. Two aspects are however worth mentioning here. The first concerns the important local structure visible in the data, the second addresses the s-dependence.

10.1 The Importance of Resonance Effects

Distinct local structures are visible in all inclusive distributions shown in this paper, in the x_F or y as well as in the p_T dependences, in the π^+/π^- ratios as well as in the moments of the p_T distributions. These structures are significantly different for π^+ and π^- production. Similar structures have been first observed in a more restricted experiment at the CERN PS in 1974 [34] and discussed in relation to resonance decay. In fact, by using the measured inclusive cross sections for the low-mass mesonic and baryonic resonances ρ and Δ^{++} such structures are readily predicted if the mass distribution of these resonances is properly taken into account. This is illustrated in Fig. 54, where the p_T dependence at fixed x_F, the x_F dependence at fixed p_T, and the mean p_T as a function of x_F for π^+ originating from ρ and Δ^{++} decays are shown. Clearly, the salient features of the data are predicted already from this very restricted set of resonances. In addition, the known charge dependence of mesonic and hadronic resonance production in p+p collisions also implies a distinct difference between π^+ and π^- as observed in the data.

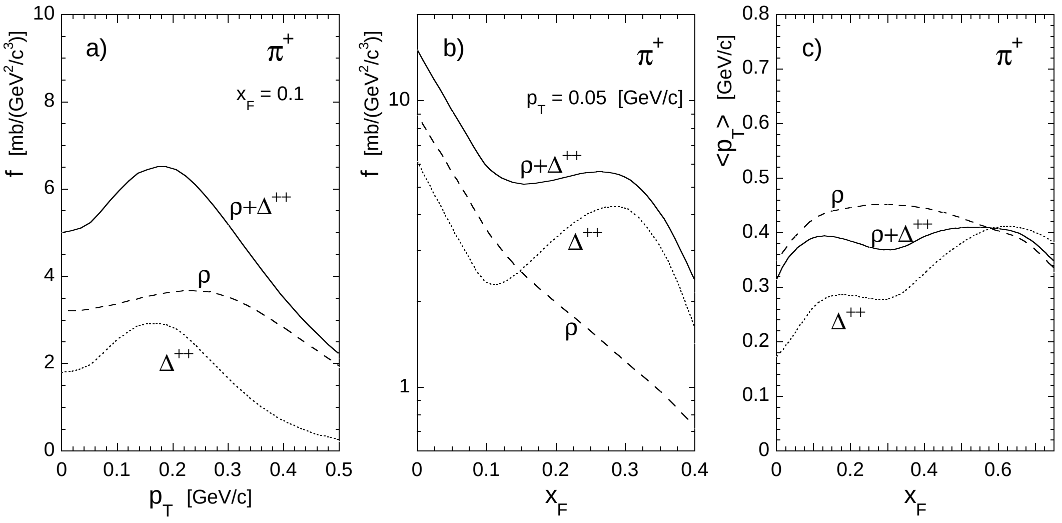

Figure 54: Monte Carlo study of a) p_T distribution at fixed x_F, b) x_F distribution at fixed p_T, c) mean p_T as a function of x_F for π^+ resulting from ρ and Δ^{++} decay.

Evidently a number of questions are raised by this argumentation. It is of course known since a long time [35] that the vast majority of all hadrons come from resonance decay. There has however been a surprising lack of attempts to assess the real consequences of this fact for all aspects of the inclusive distributions. In addition to the local structures discussed above also the full x_F and p_T dependences proper can be reproduced from resonance decay if an appropriate yield of higher mass resonances is allowed for. The past estimates [35] have only taken account of a very limited number of mostly mesonic resonances in the low mass region. There is however good reason to conclude that a much larger fraction of the almost 200 listed baryonic and mesonic resonances is produced in p+p interactions and contributes via cascading decay. A measurement of inclusive resonance cross sections well beyond the lowest-lying states therefore becomes mandatory for any progress in understanding of both the inclusive sector and particle correlations.

10.2 Energy Dependence

The problem of the s-dependence of the invariant cross sections is touched upon in this paper only in the very limited forward region of $x_F > 0.3$ and in the range of $17 < \sqrt{s} < 53$ GeV. This extension in $\sqrt{s}$ is necessary due to the lack of comparison data in the more immediate neighbourhood of interaction energy. It demonstrates the s-independence of the inclusive cross section, to a few percent level, in this area. This finding corresponds to the well-known hypotheses of limiting fragmentation [36] and Feynman scaling [37]. From the physics point of view these hypotheses have the dual aspect of the manifestation of fragmenting excited objects or of a direct trace of the partonic structure of the colliding hadrons. As such, a more detailed scrutiny also at lower and higher energies seems indicated. This study meets, in the lower $\sqrt{s}$ region, with the usual problem of the scarcity of consistent data sets. At $\sqrt{s}$ values above the ISR energy range there is in addition, the basic experimental problem of access to the forward kinematic region. Already at RHIC energies, $\sqrt{s} = 200$ GeV, the present experimental equipment is limited to $x_F < 0.15$ at the mean transverse momentum of the produced particles. This limitation becomes more and more restrictive with increasing energy at p̄p colliders and at the LHC where at best some studies around $x_F = 0$ and in the area of diffraction are feasible.

The zone at $x_F = 0$ has, on the other hand, its proper interest due to the fact that here the bulk of pionic multiplicity is produced and that the invariant cross section shows a steady increase with $\sqrt{s}$, the ”rising rapidity plateau”. These effects are not touched upon in this paper due to the principal problem of feed-down corrections as described in Section 5.6. As the ISR data for example are uncorrected for strangeness feed-down, this correction has to be performed before any reliable conclusions can be drawn. In a more general sense, the subsequent crossing of flavour thresholds and the saturation of corresponding particle yields with increasing $\sqrt{s}$, from SU(2) at the PS/AGS to SU(6) at the LHC, poses considerable problems both on the experimental and on the interpretation level.

11 Conclusion

A new and extensive set of inclusive cross sections for pion production in p+p collisions at the CERN SPS is presented and compared in detail to existing data in the corresponding energy range. The new data cover the available phase space with a consistent set of double-differential cross sections and with systematic and statistical uncertainties well below the 5% level. This precision allows for the first time in the SPS energy range, the observation of a rich substructure in the data. This structure pervades all kinds of inclusive distributions and precludes any attempt at simple analytic parametrizations. It is a direct manifestation of resonance decay.

The importance of this building-up of the inclusive particle distributions, over the full phase space, from the decay of resonances is again stressed, as it has profound consequences for the understanding of particle production in the non-perturbative sector of QCD. The new data may also serve as a basis for comparison with the more complex hadronic collisions involving nuclei in p+A and A+A interactions. Data in these areas will be provided, with similar precision, in upcoming publications.

Acknowledgements

We wish to thank the crews of the CERN accelerator complex and the H2 beam line for the delivery of the high quality proton beam. We are grateful to all groups at CERN and at the collaborating institutions involved in the design, construction, installation, operation, and maintenance of the NA49 detector. Special thanks goes to M. Flammier and the groups of M. Bosteels and C. Ferrari for the continuous support and very fruitful cooperation. We furthermore acknowledge the effective operation of the Vertex Magnets by the CERN cryogenics and power supply groups.

This work was supported by the US Department of Energy Grant DE-FG03-97ER41020/A000, the Bundesministerium für Bildung und Forschung, Germany, the Polish State Committee for Scientific Research (2 P03B 130 23, SPB/CERN/P-03/Dz 446/2002-2004, 2 P03B 04123), the Hungarian Scientific Research Foundation (T032648, T032293, T043514), the Hungarian National Science Foundation, OTKA, (F034707), the Polish-German Foundation, the Korea Research Foundation Grant (KRF-2003-070-C00015), and the Bulgarian National Science Fund (Ph-09/05).

References

[1] Y. Cho et al., Phys. Rev. Lett. **31** (1973) 413
[2] J. Erwin et al., Phys. Rev. Lett. **33** (1974) 1352
[3] C.M. Bromberg et al., Phys. Rev. **D9** (1974) 1864;
Nucl. Phys. **B107** (1976) 82
[4] W.M. Morse et al., Phys. Rev. **D15** (1977) 66
[5] T. Kafka et al., Phys. Rev. **D16** (1977) 1261
[6] J.R. Johnson et al., Phys. Rev. Lett. **39** (1977) 1173;
Phys. Rev. **D17** (1978) 1292
[7] D. Antreasyan et al., Phys. Rev. **D19** (1979) 764
[8] A.E. Brenner et al., Phys. Rev. **D26** (1982) 1497
[9] D. Brick et al., Z. Phys. **C13** (1982) 11
[10] J.L. Bailly et al., Z. Phys. **C35** (1987) 309
[11] M. Adamus et al., Z. Phys. **C39** (1988) 311
[12] M. Aguilar-Benitez et al., Z. Phys. **C50** (1991) 405
[13] A. Bertin et al., Phys. Lett. **38B** (1972) 260;
Phys. Lett. **42B** (1972) 493
[14] M. Banner et al., Phys. Lett. **41B** (1972) 547
[15] M.G. Albrow et al., Phys. Lett. **42B** (1972) 279
[16] M.G. Albrow et al., Nucl. Phys. **B56** (1973) 333
[17] L.G. Ratner et al., Phys. Rev. **D9** (1974) 1135
[18] P. Capiluppi et al., Nucl. Phys. **B70** (1974) 1
[19] M.G. Albrow et al., Nucl. Phys. **B73** (1974) 40
[20] B. Alper et al., Nucl. Phys. **B100** (1975) 237

[21] K. Guettler et al., Phys. Lett. **64B** (1976) 111
[22] M. Banner et al., Nucl. Phys. **B126** (1977) 61
[23] J. Singh et al., Nucl. Phys. **B140** (1978) 189
[24] S. Afanasiev et al., (NA49 Collaboration), Nucl. Instr. and Meth. **A430** (1999) 210
[25] C. Bovet et al., Yellow Report CERN 81-13, 1982
[26] A.S. Carroll et al., Phys. Rev. Lett. **33** (1974) 928;
Phys. Lett. **61B** (1976) 303
[27] I. Lehraus et al., Nucl. Instr. Meth. **200** (1982) 199
[28] H. Fischle et al., Nucl. Instr. Meth. **A301** (1991) 202
[29] V. Blobel et al., Nucl. Phys. **B69** (1974) 454;
E.E. Zabrodin et al., Phys. Rev. **D52** (1995) 1316
[30] G.J. Bobbink et al., Nucl. Phys. **B204** (1982) 173
[31] T. Sjostrand, Comp. Phys. Commun. **135** (2001) 238
[32] V. Blobel et al., Nucl. Phys. **B69** (1974) 454;
D. Brick et al., Nucl. Phys. **B164** (1980) 1;
T. Susa et al., (NA49 Collaboration), Nucl. Phys. **A698** (2002) 491;
S. Erhan et al., Phys. Lett. **85B** (1979) 449
[33] http://cern.ch/spshadrons
[34] U. Amaldi et al., Nucl. Phys. **B86** (1975) 403
[35] H. Grassler et al., Nucl. Phys. **B132** (1978) 1;
G. Jancso et al., Nucl. Phys. **B124** (1977) 1
[36] J. Benecke et al., Phys. Rev. **188** (1969) 2159
[37] R.P. Feynman, Phys. Rev. Lett. **23** (1969) 1415